Master's Thesis

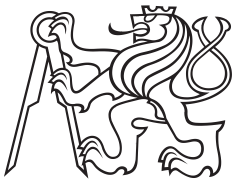

Czech Technical University in Prague

F3

Faculty of Electrical Engineering
Department of Circuit Theory

Simulative Selection of an Adaptive Real-Time Source Separation Algorithm for EIT

Bc. Lukáš Daněk

Supervisor: Diogo Silva, MSc.
Second supervisor: Ing. Jan Havlík, Ph.D.
Field of study: Medical Electronics and Bioinformatics
Subfield of study: Medical Instrumentation
August 2023

MASTER‘S THESIS ASSIGNMENT

I. Personal and study details

Student's name: **Daněk Lukáš** Personal ID number: **474504**

Faculty / Institute: **Faculty of Electrical Engineering**

Department / Institute: **Department of Circuit Theory**

Study program: **Medical Electronics and Bioinformatics**

Specialisation: **Medical Instrumentation**

II. Master’s thesis details

Master’s thesis title in English:

Simulative Selection of an Adaptive Real-Time Source Separation Algorithm for EIT

Master’s thesis title in Czech:

Simulační výběr adaptivního algoritmu separace zdrojů v reálném čase pro EIT

Guidelines:

A long-standing problem in thoracic electrical impedance tomography imaging (EIT) is the real-time separation of cardiac- and ventilation-related components of the signal. Being well spectrally described by a composition of harmonic elements, these components cannot be easily reconstructed from their superposition using traditional means such as bandpass filtering. Moreover, the non-stationarity of these signals requires a time-adaptive approach, and current promising algorithms only achieve this offline.
Fast adaptive and dynamic methods targeting the filtering or approximation of individual harmonics, such as comb filtering or harmonic regression, seem to be particularly suitable for this problem. However, they first require a pitch estimation algorithm to estimate the instantaneous heart- and breath-rate simultaneously and in real time.
Building upon basic implementations of the aforementioned algorithms, the student will extend and combine the different filtering, regression, and pitch detection techniques to investigate which one works best. Moreover, using an existing EIT signal synthesizer with known ground truth, comparison and validation of the ensemble and individual algorithm components will be performed.
The work includes the following topics:
• Simulation of a validation dataset from an existing EIT signal synthesizer
• Implementation of different multi pitch estimation algorithms
• Implementation of different source separation algorithms
• Development of a source separation quality index
• Comparison and validation of the most performant algorithmic ensemble

Bibliography / sources:

[1] S. Leonhardt and B. Lachmann, “Electrical impedance tomography: the holy grail of ventilation and perfusion monitoring?”, Intensive Care Medicine 38, 1917–1929 (2012), doi: 10.1007/s00134-012-2684-z.
[2] C. Putensen, B. Hentze, S. Muenster, and T. Muders, “Electrical Impedance Tomography for Cardio-Pulmonary Monitoring”, Journal of Clinical Medicine 8, no. 8: 1176, 2019, doi: 10.3390/jcm8081176.
[3] C. H. Antink, S. Leonhardt, and M. Walter, “A synthesizer framework for multimodal cardiorespiratory signals”, Biomedical Physics & Engineering Express 3, no. 3: 035028, 2017, doi: 10.1088/2057-1976/aa76ee.
[4] M. G. Christensen, P. Stoica, A. Jakobsson, and S. H. Jensen, “Multi-pitch estimation”, Signal Processing 88.4, 2008, pp. 972 – 983, doi: 10.1016/j.sigpro.2007.10.014.
[5] C. H. Antink, S. Leonhardt, and M. Walter, “Local Interval Estimation Improves Accuracy and Robustness of Heart Rate Variability Derivation from Photoplethysmography”, 2018 40th Annual International Conference of the IEEE Engineering in Medicine and Biology Society (EMBC), 2018, pp. 3558 – 3561, doi: 10.1109/EMBC.2018.8512908.
[6] J. M. Deibele, H. Luepschen, and S. Leonhardt, “Dynamic separation of pulmonary and cardiac changes in electrical impedance tomography”, Physiological Measurement 29, no. 6: S1, 2008, doi: 10.1088/0967-3334/29/6/S01.
[7] A. Battistel, R. Chen, N. Hallemans, R. Pintelon, J. Lataire, and K. Möller, “Harmonic Analysis for the Separation of Perfusion and Respiration in Electrical Impedance Tomography”, IFAC-PapersOnLine 54.15, 2021, pp. 281 – 286, doi: 10.1016/j.ifacol.2021.10.269.
[8] L. Tan and J. Jiang, “Novel adaptive IIR filter for frequency estimation and tracking [DSP Tips&Tricks]”, IEEE Signal Processing Magazine 26, no. 6, 2009, pp. 186–189, doi: 10.1109/MSP.2009.934189.

Name and workplace of master's thesis supervisor:

Diogo Silva, MSc. RWTH Aachen University

Name and workplace of second master's thesis supervisor or consultant:

Ing. Jan Havlík, Ph.D. Department of Circuit Theory, FEE

Date of master's thesis assignment: **13.02.2023** Deadline for master's thesis submission: **31.08.2023**

Assignment valid until: **22.09.2024**

Diogo Silva, MSc. Supervisor's signature	doc. Ing. Radoslav Bortel, Ph.D. Head of department's signature	prof. Mgr. Petr Páta, Ph.D. Dean's signature

III. Assignment receipt

The student acknowledges that the master's thesis is an individual work. The student must produce his thesis without the assistance of others, with the exception of provided consultations. Within the master's thesis, the author must state the names of consultants and include a list of references.

.	
Date of assignment receipt	Student's signature

Acknowledgements

I would like to express my gratitude to my supervisor Diogo Silva, MSc. for his great support and encouragement when supervising my Master's Thesis. With his advice and all the essential insights, I could always focus on the things that mattered most. Moreover, I would like to thank him for providing me with the basic implementations of the presented algorithms that helped me to deliver the Thesis with appropriate quality and on time.

I would also like to thank my second supervisor Ing. Jan Havlík, Ph.D. for supervising my Master's Thesis at CTU in Prague. Even more importantly, I would like to thank him for bringing my attention to medical electronics four years ago and inspiring me to participate in the Double Degree program.

I am also very grateful to my family for their endless support in everything I do. Without them, nothing of this would be possible. Moreover, I would like to thank my girlfriend for all her trust and encouragement.

Last but not least, I would like to express my gratitude to Univ.-Prof. Dr.-Ing. Dr. med. Dr. h.c. Steffen Leonhardt for the opportunity to study the T.I.M.E. Double Master Program and to write my Master's Thesis at the chair of MedIT at RWTH Aachen University.

Author statement

I declare that the presented work was developed independently and that I have listed all sources of information used within it in accordance with the methodical instructions for observing the ethical principles in the preparation of university theses.

place, date	signature

Abstract

Electrical impedance tomography (EIT) is a cheap and non-invasive medical imaging method widely used for continuous mechanical ventilation monitoring at the bedside. However, the measured impedance changes are induced not only by lung volume changes, which are most observable, but also by changes in lung tissue perfusion. Since the respective two EIT signal components are described in the frequency domain by a superposition of overlapping harmonic elements, they cannot be easily reconstructed using traditional filtering methods. Moreover, the current promising algorithms are not suitable for real-time applications. Therefore, this work investigates different adaptive and dynamic methods, such as comb filtering or harmonic regression, to find the most suitable one for real-time source separation in EIT. After analyzing multiple possibilities, comb filtering, as the most effective method to be implemented and combined with other filtering methods, is selected to serve as a proof of concept. However, since it requires accurate instantaneous heart and respiratory rate estimation, multi-pitch estimation methods based on grid search and interval length estimation are implemented and improved to produce the best possible results. The implemented algorithms are validated and compared using a validation signal with known ground truth generated with an existing EIT synthesizer. For performance assessment, pitch estimation and source separation quality measures are developed. In the end, the best-performing algorithm proves that comb filtering can provide good source separation results in real time when combined with the implemented multi-pitch estimation algorithms and other filtering methods. Although the implemented algorithms have certain limitations and no real EIT signal measured in patients was used for their validation, they represent a further step towards real-time source separation in EIT.

Keywords: electrical impedance tomography (EIT), source separation, multi-pitch estimation, comb filtering, EIT signal synthesis

Supervisor: Diogo Silva, MSc.
Chair of Medical Information Technology (MedIT)
at the Helmholtz Institute for Biomedical Engineering
RWTH Aachen University
Pauwelsstr. 20, 52074 Aachen

Abstrakt

Elektrická impedanční tomografie (EIT) je levná a neinvazivní zobrazovací metoda, která se široce používá k průběžnému monitorování umělé plicní ventilace na lůžku. Změny měřené impedance jsou však vyvolány nejen změnami objemu plic, které jsou nejvíce pozorovatelné, ale také změnami prokrvení plicní tkáně. Vzhledem k tomu, že odpovídající složky signálu EIT jsou ve frekvenční oblasti popsány superpozicí překrývajících se harmonických frekvencí, nelze je snadno rekonstruovat pomocí tradičních filtračních metod. Současné perspektivní algoritmy navíc nejsou vhodné pro použití v reálném čase. Proto tato práce zkoumá různé adaptivní a dynamické metody, jako je hřebenová filtrace nebo harmonická regrese, s cílem najít tu nejvhodnější pro separaci zdrojů EIT signálu v reálném čase. Po analýze více možností je jako nejefektivnější metoda na implementaci a kombinaci s dalšími filtračními metodami vybrána hřebenová filtrace, aby posloužila pro základní ověření jako tzv. proof of concept. Protože však vyžaduje přesný odhad okamžité srdeční a dechové frekvence, jsou implementovány a optimalizovány metody odhadu základní frekvence založené na vyhledávání v mřížce a odhadu délky intervalu, aby bylo dosaženo co nejlepších výsledků. Implementované algoritmy jsou ověřeny a porovnány pomocí validačního signálu se známými složkami, tzv. ground truth, vygenerovaného pomocí existujícího EIT syntezátoru. Pro hodnocení výkonu jsou vyvinuta měřítka kvality odhadu základní frekvence a separace zdrojů. Algoritmus s nejlepšími výsledky nakonec dokazuje, že hřebenová filtrace může v kombinaci s implementovanými algoritmy odhadu základní frekvence a dalšími filtračními metodami poskytnout dobré výsledky separace zdrojů v reálném čase. Přestože mají implementované algoritmy určitá omezení a při jejich validaci nebyl použit žádný skutečný signál EIT změřený na pacientovi, představují další krok směrem k separaci zdrojů v EIT v reálném čase.

Klíčová slova: elektrická impedanční tomografie (EIT), separace zdrojů, odhad základní frekvence, hřebenová filtrace, syntéza EIT signálu

Překlad názvu: Simulační výběr adaptivního algoritmu separace zdrojů v reálném čase pro EIT

Contents

Acknowledgements v

Abstract ix

Contents xiii

List of abbreviations xv

1 Introduction 1

2 Theoretical background 3
2.1 EIT fundamentals . . . 3
2.1.1 Impedance measurement . . . 4
2.1.2 Adjacent stimulation . . . 5
2.1.3 Image reconstruction . . . 6
2.1.4 EIT signal origins . . . 9
2.1.5 Applications . . . 10
2.2 Source separation in EIT . . . 11
2.2.1 Principal component analysis (PCA) . . . 12
2.2.2 Empirical mode decomposition (EMD) . . . 13
2.2.3 Harmonic regression . . . 15
2.2.4 Comb filtering . . . 17
2.3 Multi-pitch estimation in EIT . . . 19
2.3.1 Grid search . . . 20
2.3.2 Continuous local interval estimator (CLIE) . . . 22
2.4 EIT signal synthesis . . . 25
2.4.1 Anatomical models . . . 25
2.4.2 Mathematical models . . . 26

3 Methods and implementation details 29
3.1 Comparison of available methods . . . 29
3.2 Implementation of the selected methods . . . 30
3.2.1 Pixel detection algorithm . . . 31
3.2.2 Multi-pitch estimation using grid search . . . 32
3.2.3 Multi-pitch estimation using CLIE . . . 36
3.2.4 Source separation using comb filtering . . . 38
3.3 Validation signal synthesis . . . 40
3.3.1 EIT signal synthesizer . . . 40
3.3.2 Input values for the synthesizer . . . 43
3.3.3 Synthesized EIT signals . . . 45
3.4 Performance assessment metrics . . . 48
3.4.1 RMSE and bias . . . 48

3.4.2 Bland–Altman plot 49
3.4.3 Computation time 49
3.4.4 MEQI 50
3.4.5 SSQI 50

4 Results and discussion **51**
4.1 Multi-pitch estimation algorithms 51
4.1.1 Grid search algorithm 51
4.1.2 Iterative CLIE algorithm 56
4.2 Parameter optimization 59
4.2.1 Grid search algorithm 60
4.2.2 Iterative CLIE algorithm 62
4.3 Source separation algorithms 64

5 Conclusion **69**

Bibliography **71**

A Parameter optimization figures **77**
A.1 Grid search algorithm 77
A.2 Iterative CLIE algorithm 79

List of abbreviations

BCG	ballistocardiography
BP	blood pressure
bpm	breaths/beats per minute
CLIE	continuous local interval estimator
CRS	cardiac-related signal
CT	computed tomography
ECG	electrocardiography
EIT	electrical impedance tomography
EMD	empirical mode decomposition
FEM	finite element method
FFT	Fast Fourier Transform
FIR	finite impulse response
fps	frames per second
GREIT	Graz consensus reconstruction algorithm for EIT
HHT	Hilbert-Huang transform
HP	high-pass
HR	heart rate
ICU	intensive care unit
IIR	infinite impulse response
IMF	intrinsic mode functions
LASTA	lag-adaptive short-time autocorrelation
LLS	linear least squares
LMS	least mean squares
LoA	limits of agreement
LP	low-pass
MA	movement artifacts
MedIT	Medical Information Technology
MEEMD	multi-dimensional ensemble empirical mode decomposition
MEQI	multi-pitch estimation quality index
PAP	peak arterial pressure
PCA	principal component analysis
PPG	photoplethysmography
PRQ	pulse-respiration quotient
PWV	pulse wave velocity
RMSE	root mean square error
ROI	region of interest
RR	respiratory rate
SSQI	source separation quality index
VRS	ventilation-related signal

1 Introduction

Electrical impedance tomography (EIT) was first published in 1978 by Ross P. Henderson and John G. Webster [1] as a new medical imaging method, and since then, it has become widely used. It has been employed primarily at the bedside for continuous ventilation monitoring thanks to being minimally invasive, radiation-free, relatively cheap, and real-time.

The principle of EIT is measuring the impedance inside the patient's body using surface electrodes. Specifically, when acquiring thorax images, the changes in impedance due to breathing are usually reconstructed. However, these changes are induced not only by varying lung volume but also by blood volume changes in the heart and vessels.

Since gas exchange efficiency in the lungs depends on both ventilation and perfusion, separating these two sources of the EIT signal continuously and in real-time would make the ventilation monitoring more accurate and enable a possible use of EIT for simultaneous cardiac activity monitoring.

However, separating cardiac-related signal (CRS) and ventilation-related signal (VRS) is not an easy task because, according to [2] and [3], the perfusion-related changes in thoracic impedance are about one order of magnitude smaller than the changes induced by ventilation. Furthermore, as shown in, for example [3], the harmonics of these two signals usually overlap in the frequency domain, and, therefore, the signals cannot be separated accurately enough using only simple filtering methods, such as low-pass (LP) or high-pass (HP) filtering. Last but not least, the signals are non-stationary, which requires a time-adaptive approach.

Therefore, source separation in EIT is a long-standing problem, and there are some promising attempts at solving it, e.g., [4], [5], [6]. However, currently available algorithms cannot perform the separation continuously and in real time.

To address this, different dynamic source separation approaches are investigated and compared in this work. After analyzing various possibilities, one of the methods is implemented and combined with accurate respiratory rate (RR) and heart rate (HR) estimation algorithms to prove the general concept. Moreover, a validation signal is simulated using an existing EIT signal synthesizer to validate and compare all the implemented algorithm combinations using various performance metrics.

2 Theoretical background

This chapter provides a theoretical background to the topics most important for the thesis. The first section explains the basic principles of EIT, including impedance measurement with the surface electrodes, the so-called adjacent stimulation pattern, and image reconstruction using time differential imaging. Moreover, the origins of the EIT signal are described in more detail, and the most common current applications of EIT are presented.

The second section describes the previously published approaches to source separation in EIT investigated in this work. This includes the algorithms based on principal component analysis (PCA) and empirical mode decomposition (EMD) and those relying on frequency domain analysis, namely harmonic regression and comb filtering.

Consequently, the two approaches to estimating RR and HR that are considered for adaptation and combination with the selected source separation method are summarized in the following section. This includes the grid search algorithm and the continuous local interval estimator (CLIE).

Finally, the last section briefly introduces the synthesis of the EIT signal. Two general approaches, anatomical and mathematical modeling, are described in detail.

2.1 EIT fundamentals

EIT is a two-dimensional imaging method that measures the body's electrical properties, namely the impedance, using a set of electrodes attached to the body surface, typically around the thorax. Such a measurement is minimally invasive, radiation-free, and, therefore, suitable for continuous long-time monitoring. Therefore, it has been employed mainly at the bedside for monitoring regional lung ventilation in mechanically ventilated patients [7].

Moreover, EIT is computationally inexpensive, cheap, and real-time, with the ability to produce a video with the frame rate reaching up to 50 frames per second (fps). Unfortunately, because of the measurement principle, EIT has a very low spatial resolution limited to the distance between electrodes (approximately 20 - 30 mm) at best [3].

EIT for cardiorespiratory monitoring utilizes the fact that the lung tissue has a different impedance when inflated or deflated, and the blood has a different impedance than the tissue. However, measuring absolute impedance values is challenging for many reasons. Instead, the current state-of-the-art is time-differential (relative) EIT imaging [2]. Figure 2.1 shows the schematic representation of the EIT measurement workflow presented in [7]. The following sections describe the involved steps one by one in more detail.

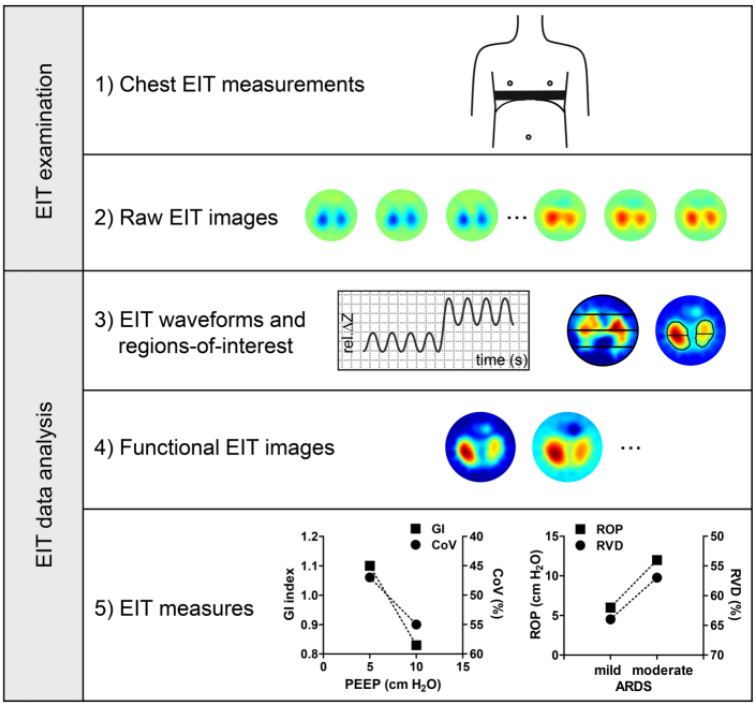

Figure 2.1: Schematic representation of the EIT measurement workflow [7].

2.1.1 Impedance measurement

In general terms, impedance is the opposition of a matter to alternating current introduced by the electrodes in a closed electrical circuit. Mathematically expressed, impedance is a complex quantity Z described by equation

$$Z = R + jX, \tag{2.1}$$

where R is the resistance, j is the imaginary unit, and X is the reactance. The resistance expresses the given matter's opposition to the DC component of the introduced current, and the reactance represents the effects of the constantly-changing AC component of the introduced current.

However, as comes from Ohm's law, impedance Z is also given as

$$Z = \frac{V}{I}, \tag{2.2}$$

where V is voltage and I is electric current. Therefore, the impedance of the human tissue (the so-called bioimpedance) can be determined by injecting a small alternating current, e.g., 5 mA at a frequency of 50 kHz, and measuring the generated voltage [2].

2.1.2 Adjacent stimulation

The most common impedance measurement method in EIT is the adjacent stimulation (adjacent drive configuration). Usually, a belt containing 16 electrodes is placed on the body surface around the thorax. For lung imaging, the 4th–6th intercostal space is typically used [7, 2], as shown in the following figure.

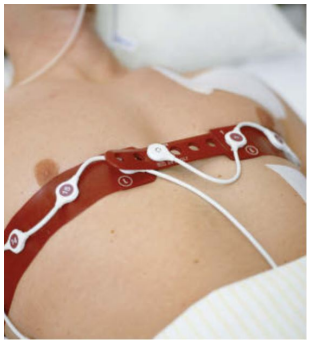

Figure 2.2: Typical electrode belt placement on the patient's body [8].

The adjacent stimulation works by injecting a small alternating current using one electrode pair and measuring the generated surface voltages using the remaining electrode pairs. When the voltages are measured, the current injection is switched to the neighboring electrode pair, and the whole pattern is rotated [2, 7, 9], as shown in the figure below.

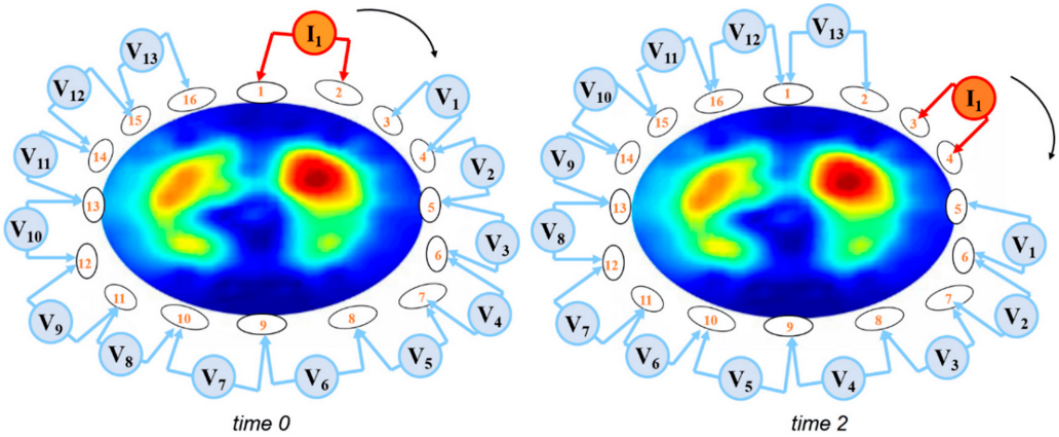

Figure 2.3: EIT measurement using the adjacent stimulation pattern [9].

The entire image is reconstructed once the current injection rotates around the thorax completely [2]. The EIT video is then created by placing the time-consecutive images in a sequence.

2.1.3 Image reconstruction

Image reconstruction in EIT aims to reconstruct the impedance distribution in the measurement plane using the measured surface voltages. At first sight, it might seem reasonable to use the same backprojection algorithm as computed tomography (CT) does. And indeed, this is how the first EIT reconstruction methods worked [3].

As explained in [10], during the CT examination, the X-rays come out from the X-ray tube and travel through the patient to be measured on the detector. When assuming they are always straight and parallel, the image can be reconstructed based on the detector measurement and the known geometry of the CT scanner.

However, in EIT, the pathways of the injected current through the body are not straight nor parallel. Therefore, when the CT backprojection algorithm is applied, only a low-quality reconstruction with many inaccuracies and errors can be achieved [3]. Therefore, more sophisticated EIT reconstruction algorithms have been developed over time.

Forward and inverse problem

In principle, two problems can be addressed in EIT image reconstruction. First, the forward problem can be described as a simulation of the measured voltages using prior knowledge of the impedance distribution in the body. The forward problem can be expressed by equation

$$\mathbf{v} = \mathbf{f}(\mathbf{z}), \tag{2.3}$$

where $\mathbf{v}$ is the surface voltage, and $\mathbf{z}$ is the impedance distribution. This can be easily solved using, for example, the finite element method (FEM) [3].

However, the EIT reconstruction has to find the impedance distribution using the measured surface voltage, which requires solving the inverse problem described as

$$\mathbf{z} = \mathbf{f}^{-1}(\mathbf{v}). \tag{2.4}$$

Unfortunately, the inverse problem is ill-posed and analytically unsolvable. Therefore, its solution is the critical part of the EIT reconstruction. However, obtaining absolute impedance values would be very difficult because it would require a perfect knowledge of the absolute electrode positioning and the geometry of the patient's thorax [2]. Thus, the so-called relative EIT imaging, introduced in [11] and [12], is typically used instead.

Time differential imaging

Time differential imaging is one of the relative EIT imaging methods. Instead of reconstructing the absolute impedance values, the impedance changes $\mathbf{x} = \Delta\mathbf{z}$ are reconstructed using normalized voltage differences

$$\mathbf{y} = \frac{\mathbf{v} - \mathbf{v}_{ref}}{\mathbf{v}_{ref}}, \tag{2.5}$$

where $\mathbf{v}_{ref}$ is the voltage measurement at a specific time point [12]. Consequently, physiological processes such as breathing and heartbeats are displayed in an EIT image sequence. However, the absolute impedance values are lost.

GREIT

Although more methods are available, the current state-of-the-art EIT reconstruction is the Graz consensus reconstruction algorithm for EIT (GREIT), presented by Andy Adler et al. in [13]. As explained by the authors, GREIT is based on a linear reconstruction, mathematically described as

$$\hat{\mathbf{x}} = \mathbf{R}\mathbf{y}, \tag{2.6}$$

where $\hat{\mathbf{x}}$ is the reconstructed impedance change, and R is the reconstruction matrix. The essential task is to find the reconstruction matrix R as accurately as possible [13].

As further explained by the authors, a finite element model such as the one shown in Figure 2.4 is first generated. Next, known target electrical conductivity values are defined to create a set of training data. Subsequently, the forward problem is solved to obtain a simulated voltage measurement $\tilde{\mathbf{y}}$ while accounting for the measurement noise and electrode movement artifacts. Since the target conductivity distribution is known, the perfect reconstruction would reproduce it precisely using $\tilde{\mathbf{y}}$ [13].

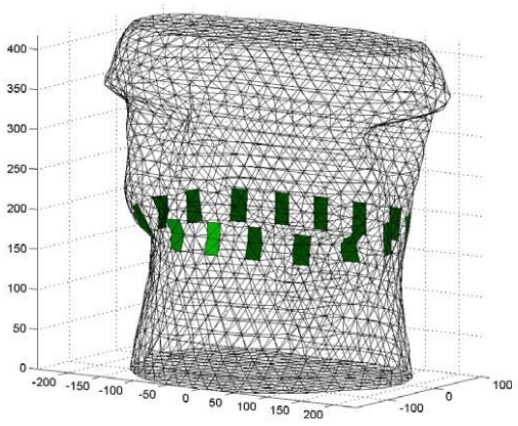

Figure 2.4: Finite element model of an adult thorax with rectangular electrodes [13].

The authors of GREIT defined a set of training EIT images and designed several figures of merit to assess the reconstruction quality. The figures of merit were described in detail by the authors and took various image properties into account: signal amplitude, position error, resolution, shape deformation, and ringing artifacts in the inverted image [13].

The reconstruction matrix R is calculated using an iterative approach with step k. The optimal R^* minimizes the reconstruction error

$$\epsilon^2 = \sum_k \|\tilde{\mathbf{x}}^{(k)} - \mathbf{R}\tilde{\mathbf{y}}_t^{(k)}\|^2_{\mathbf{w}^{(k)}}, \tag{2.7}$$

where $\tilde{\mathbf{x}}$ is the training image of impedance changes, and $\mathbf{w}$ is a diagonal matrix of pixel weights. [13, 3].

It is to be pointed out that the reconstruction matrix R is calculated without using any real data. Then, it is used to quickly solve the inverse problem of EIT when the real voltage measurements are available. Given that the EIT reconstruction can be linearized, as long as the actual geometry of the body and the simulated finite element model are close to each other, good reconstruction results can be achieved [13, 3].

Reconstructed image and EIT signal

A reconstructed EIT image shows the cross-section of the thorax. The left and right sides of the image represent the right and left sides of the thorax, respectively. The upper and lower sides of the image represent the ventral and dorsal sides of the body, respectively [3]. Therefore, the heart can be found mostly between the top and center of the image, while the lungs are usually located on the sides and on the bottom.

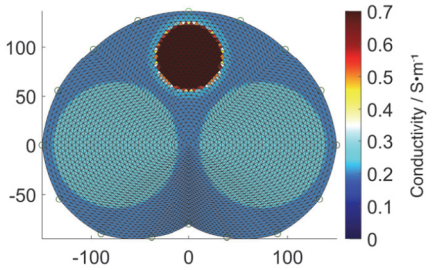

Figure 2.5: Typical heart (dark red) and lung (light blue) locations in EIT image [14].

The colors in the EIT image, better pronounced in Figure 2.3, usually represent the amplitude of the impedance change in the given pixel [2]. Typical resolutions of the EIT images are 32x32 or 64x64 pixels.

Considering time differential imaging, the EIT signal in one image pixel is the impedance change in the given pixel over time. The term global impedance change or global EIT signal refers to one signal representing a sum of all impedance changes over the whole EIT image divided by the number of image pixels. Similarly, the EIT signal of a specific image area can be obtained by summing over a defined region of interest (ROI) and dividing by the number of pixels in the given region [3, 7].

2.1.4 EIT signal origins

This section briefly summarizes the processes inside the thorax that cause impedance changes, thus affecting the EIT signal. The most significant changes in impedance are caused by respiration; less important yet observable are the changes caused by cardiac activity [3, 2].

Due to periodic changes in air volume inside the alveoli during the breathing cycle, the surrounding tissue is stretched and shrunken repeatedly. Consequently, the average current pathways are prolonged and shortened during inspiration and expiration. Thus, the electrical impedance of the lung tissue increases during inspiration and decreases during expiration [9].

Since the blood has a significantly lower impedance than the tissue, increasing blood volume in a given region lowers the impedance in that region. It is to be noted that the influence of perfusion on EIT signal can be observed in both the heart and lung regions [9]. As shown in Figure 2.6, the impedance changes caused by the heart activity are responsible for small ripples superimposed on the slower oscillations caused by respiration.

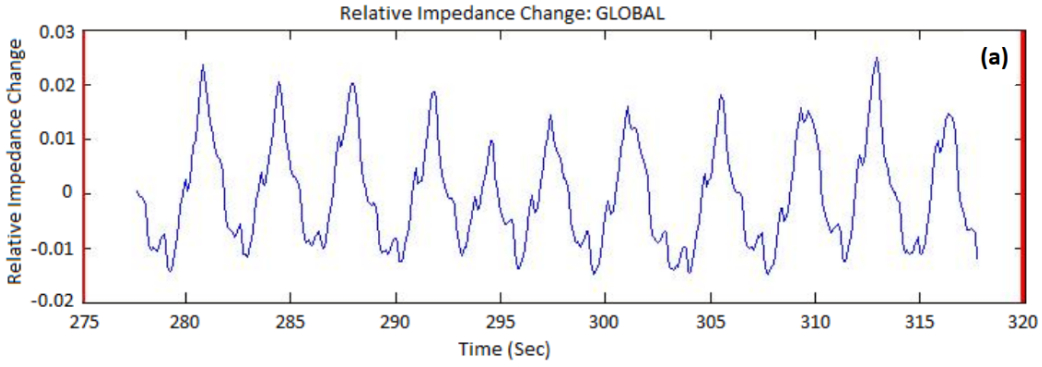

Figure 2.6: Example of a global EIT signal [15]

Minor impedance changes inside the human thorax can also be caused by other physiological processes, e.g., changes in ion concentrations. However, these changes are usually slow, and their influence is not comparable to respiration and perfusion [3].

2.1.5 Applications

EIT is commonly used for mechanical ventilation monitoring in patients at the intensive care unit (ICU). However, since the efficiency of gas exchange in lungs depends on both ventilation and perfusion, simultaneous monitoring of the cardiac activity is also very important.

It is to be noted that there are also some other possible applications of EIT, such as functional brain imaging, especially in some clinical situations where standard methods are not suitable. For example, EIT could help improve the limited understanding of how information is processed in neuroanatomical pathways [3]. However, such applications are not important for this work.

Ventilation monitoring

When a patient at the ICU suffers from acute respiratory failure, mechanical ventilation is monitored continuously with EIT to detect changes in the patient's condition and for individual treatment adaptation. With regional ventilation distribution monitoring, some acute injuries can be quickly identified [3].

Therefore, EIT has become well-established, and over the years, many different measures for ventilation distribution monitoring have been developed. For example, intuitive information is provided to clinicians at the bedside by the percentage of ventilation in the given image quadrant or with the Center of Ventilation (CoV) [2].

Moreover, the global inhomogeneity index (GI index) and the coefficient of variation (CV) were developed to quantify the ventilation distribution's homogeneity. Other measures, such as tidal variation (TV) and its distribution, are also commonly used [3].

Perfusion monitoring

As explained in [3], EIT has a very high potential when used in perfusion monitoring thanks to being non-invasive, real-time, and achieving high temporal resolution. There are three classes of hemodynamic parameters worth considering for EIT application - pressure, flow, and functional volume status [3].

However, since the impedance changes related to cardiac activity and lung perfusion are about one order of magnitude smaller than the changes caused by mechanical ventilation, obtaining accurate information on the hemodynamic parameters, such as cardiac output or stroke volume, and lung perfusion using EIT is very challenging [2, 3].

Therefore, several measurement and analysis techniques have been developed over the years to separate the VRS and CRS in the EIT signal, sometimes referred to as the mixed (EIT) signal. These include, for example, electrocardiogram-gated averaging, apnea measurements, or frequency domain filtering [2].

2.2 Source separation in EIT

Source separation in EIT aims to separate VRS and CRS in the mixed EIT signal. However, as already mentioned in the previous chapter, this is not an easy task because **(a)** the CRS is about one order of magnitude smaller than the VRS [2], [3], **(b)** traditional frequency filtering, i.e., low-pass or high-pass, is not suitable because of the overlapping harmonic frequencies as shown in Figure 2.7, and **(c)** a real-time, computationally inexpensive solution is required to keep EIT applicable for ventilation and perfusion monitoring at the bedside.

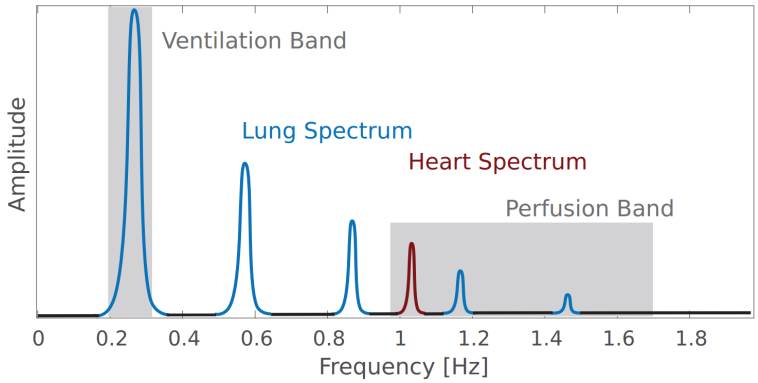

Figure 2.7: A simplified spectrum of an EIT signal [3].

To address the problem of the small CRS amplitude, several measurement methods have been developed so far. One of them is called electrocardiography (ECG) gating. As explained in [2], this technique amplifies the CRS by summing over N heart cycles starting at each QRS complex. At the same time, the ECG signal is measured synchronously with the EIT signal. That way, the signal strength of CRS is amplified by a factor of $\sqrt{N}$. However, considering, for example, 200 heart cycles, the visualization of CRS on the diagnostic screen is delayed by 100 heartbeats, which excludes real-time analysis [2].

Another measurement technique is based on briefly interrupting the ventilation to exclude the VRS from the measured signal completely. It has been proved in [16] and [17] that the apnea methods can provide valuable information on stroke volume and, potentially, on local V/Q distribution. However, as mentioned in [2], the ventilatory situation is changed during the apnea, which can lead to further changes in cardiac activity and perfusion.

Moreover, introducing even a short apnea period in mechanically ventilated patients at the bedside might be undesirable when, for example, a patient suffers an acute respiratory failure and his life depends on mechanical ventilation.

Another option to enhance CRS is using a hypertonic saline solution as an electrical impedance contrast agent. This has been demonstrated in [18]. However, this method is invasive and non-repeatable since a relatively high-concentration saline is intravenously injected. Moreover, as mentioned in [2], even though it seems to have some potential for quantification and future clinical application, this analysis is not beat-to-beat and is delayed by the time-of-flight necessary for the passage of the contrast agent (about 10 seconds) [2]. This prevents such a method from a potential application for real-time monitoring at the bedside.

Since all the measurement methods presented above have certain limitations, developing an accurate real-time source separation algorithm based on the standard EIT signal analysis is very important. In the following sections, some possible approaches considered in this work are described in detail.

2.2.1 Principal component analysis (PCA)

In [4], J. M. Deibele et al. proposed a method of fitting the so-called template functions for the pulmonary and cardiac components into the input signals. These template functions are estimated using PCA and frequency domain filtering [4].

As presented by the authors of [4], the assumption that each input signal matrix X is composed of unknown ventilation (V), cardiac (C) and noise (or remainder, R) components, yields the possibility to write

$$\mathbf{X} = \mathbf{X}_V + \mathbf{X}_C + \mathbf{X}_R. \tag{2.8}$$

Thus, after finding the first principal component

$$\mathbf{B}_V = \mathrm{PCA}(\mathbf{X}, 1), \tag{2.9}$$

the ventilation component can be estimated using the least mean squares (LMS) as

$$\overline{\mathbf{X}}'_V = \mathrm{LMS}(\mathbf{X}, \mathbf{B}_V). \tag{2.10}$$

However, as the authors of [4] explain, the first approximation of the cardiac component would contain a lot of noise when obtained as

$$\overline{\mathbf{X}}'_C = \mathbf{X} - \overline{\mathbf{X}}'_V \tag{2.11}$$

because the $\mathbf{X}_R$ component is still unknown. Therefore, the first two approximations of $\mathbf{X}_V$ and $\mathbf{X}_C$ are further processed to yield better results [4].

The subsequent processing is performed using the template functions and various filtering methods followed by another PCA and LMS to finally obtain accurate ventilation and cardiac component estimation $\overline{\mathbf{X}}_V$ and $\overline{\mathbf{X}}_C$ [4].

Figure 2.8 shows the results of the proposed algorithm as presented by [4]. The upper figure on the left shows the input signal X, and the lower figure shows the isolated cardiac component $\overline{X}_C$ (solid) and ECG signal (dashed) for comparison. The lines in the right figure are depicted with an offset for better discrimination [4].

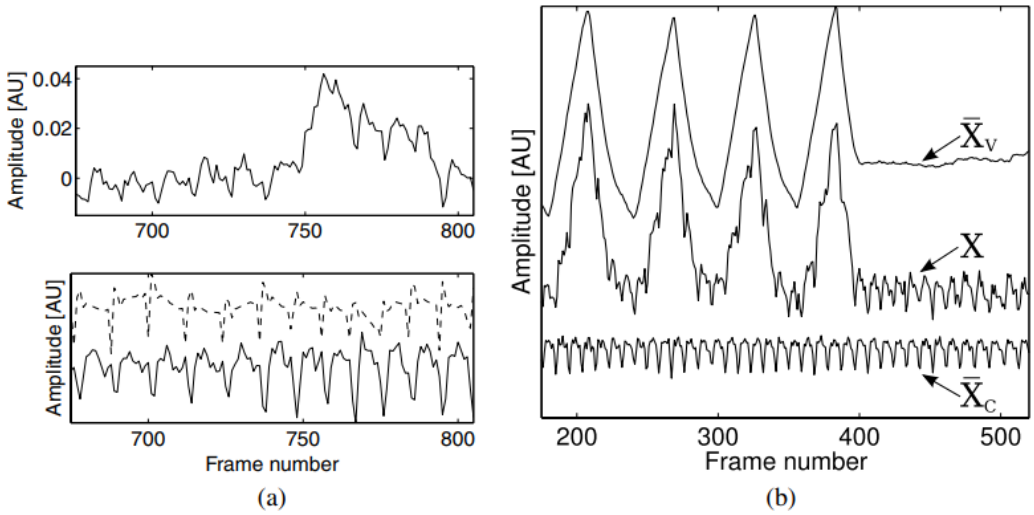

Figure 2.8: Input signal and the results of the PCA source separation [4].

As stated by the authors of [4], their method enables an observer to examine the variation of the cardiac signal beat-by-beat after a one-time setup period of 20 s, and the results are superior to frequency domain filtering. Furthermore, no time delay (lag) is induced by the proposed algorithm between the true signal and the estimated components [4].

However, they admit that the complexity of the calculations restricts the PCA to be performed every two minutes only. Therefore, the proposed algorithm cannot work continuously in real-time, and, more importantly, it yields good results only when cardiac and ventilation activity change slowly over time [4].

2.2.2 Empirical mode decomposition (EMD)

A different approach was proposed by X. Sun et al. in [5]. They introduced a method based on multi-dimensional ensemble empirical mode decomposition (MEEMD) to explore the so-called intrinsic mode functions (IMF) of the VRS and CRS in the mixed EIT

signal. Such an approach is inspired by the nonlinear and time-variant mechanics of the cardiorespiratory system [5].

In mathematical terms, EMD is a part of the so-called Hilbert-Huang transform (HHT), initially proposed by Norden E. Huang et al. in [19]. HHT is an algorithm for obtaining instantaneous frequency information. Unlike Fourier transform, HHT was developed especially for analyzing data from nonlinear and nonstationary processes. EMD is a necessary step of HHT to reduce any given data into a collection of IMF to which the so-called Hilbert spectral analysis can be applied [19].

As explained in [19], IMF represent simple oscillatory modes as counterparts to simple harmonic functions. By definition, IMF are any functions with the same number of extrema and zero crossings. The envelopes of these functions, defined by all the local maxima and minima, are symmetric with respect to zero [19].

To utilize EMD for source separation in EIT, the authors of [5] first select three EIT image pixels, each from a different region: the ventilation-dominated region, the cardiac-dominated region, and the overlapping region. After that, they employed 1D-EMD on each pixel's EIT signal and conducted a multi-scale analysis of the decomposed components, thus changing EMD to MEEMD [5].

To extract the VRS and CRS, the authors projected physiological components into IMF based on a specific two-stage combination strategy. As proposed in [5], a decomposition of a signal into N IMF and a residue r_N is described by equation

$$s(t) = \sum_{j-1}^{N} c_j + r_N, \tag{2.12}$$

with the analytic signal

$$z_j(t) = c_j(t) + y_j(t) \cdot i = a_j(t) \cdot e^{i \cdot \theta(t)}, \tag{2.13}$$

where $y_j(t)$ is the HHT. As further explained in [5], the local properties of the j_{th} IMF can be emphasized by HHT, defined as

$$y_j(t) = \frac{1}{\pi} \int_{-\infty}^{\infty} \frac{c_j(\tau)}{t - \tau} d\tau. \tag{2.14}$$

With $a_j(t) = \sqrt{c_j^2(t) + y_j^2(t)}$ being the instantaneous amplitude and $\theta_j(t) = \arctan \frac{y_j(t)}{c_j(t)}$ the instantaneous phase, the instantaneous frequency, indicating the rate of phase change, is given as

$$\omega_j(t) = \frac{d\theta_j(t)}{dt}. \tag{2.15}$$

Finally, as stated by the authors of [5], using the instantaneous amplitude and phase, the original signal can be expressed by equation

$$s(t) = \Re\left[\sum_{j=1}^{N} a_j(t) \cdot e^{i\int \omega_j(t)dt}\right]. \tag{2.16}$$

Figure 2.9 shows the results of the proposed method as presented in [5]. The input EIT signal involves an apnea period after inhalation, clearly observable in the original signal waveform (a) and the VRS waveform (e).

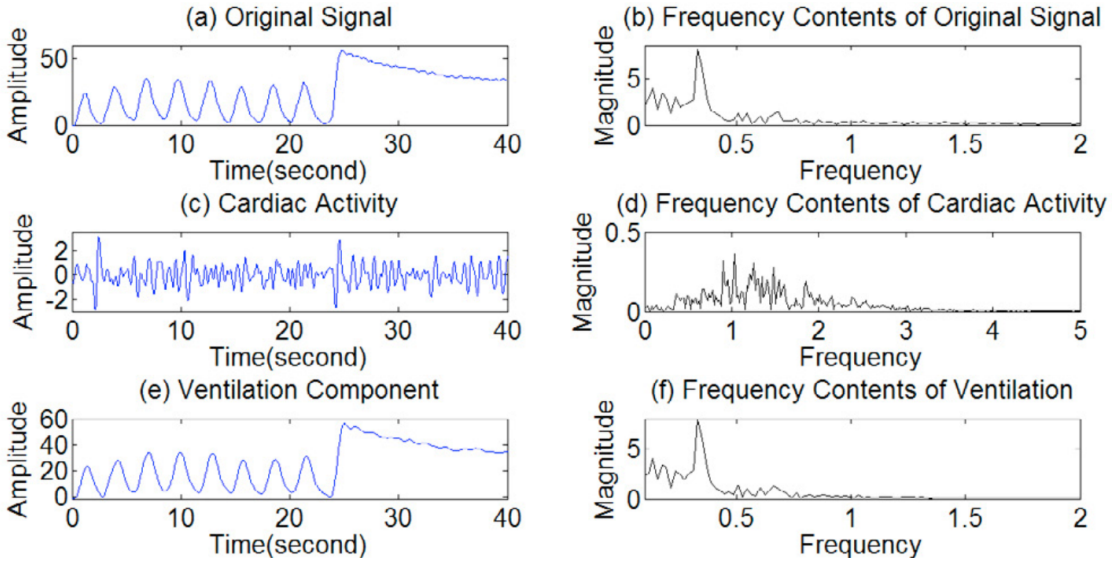

Figure 2.9: Results of the EMD separation in the ventilation-dominated region [5].

Similar to the PCA source separation described in the previous section, the results of the EMD source separation look very promising. However, the algorithm proposed in [5] cannot work in real-time, although the authors claim that a real-time implementation seems feasible in the near future.

2.2.3 Harmonic regression

In [6], A. Battistel et al. showed a possible way how to exploit the differences in fundamental frequencies of VRS and CRS using linear regression in the frequency domain. According to the authors, when making certain assumptions, an EIT signal can be expressed as

$$y(t,\theta) = \sum_{p=0}^{N_p} \sum_{f\in H} \left(\theta^g_{f,p}\, cos(2\pi ft) - \theta^h_{f,p}\, sin(2\pi ft)\right)\, \tilde{b}_p(t), \tag{2.17}$$

where θ is a parameter vector containing coefficients $\theta^g_{f,p}$ and $\theta^h_{f,p}$, and $\tilde{b}_p(t)$ are the so-called basis functions [6].

With some further modifications and after showing the benefits of using the so-called Hermite polynomials and Hermite functions, the authors describe how the estimation of the coefficients $\theta^g_{f,p}$ and $\theta^h_{f,p}$ in the frequency domain is performed.

As explained in [6], the frequency domain data can be written in matrix form

$$\mathbf{Y}_w = K\theta + V, \tag{2.18}$$

where Y_w is the frequency-domain data $y(t)$, K is a regression matrix consisting of the basis functions $\tilde{B}_p$, and V is a noise vector. This way, the optimal parameters $\hat{\theta}$ can be obtained by least squares method as

$$\hat{\theta} = arg\min_{\theta} ||\mathbf{Y}_w - K\theta||^2 = (K^T K)^{-1} K^T \mathbf{Y}_w. \tag{2.19}$$

Finally, the coefficients corresponding to the respiration and perfusion frequencies and their harmonics are obtained from the estimated parameter vector $\hat{\theta}$ and the separated VRS and CRS are reconstructed using equation 2.17 [6].

The following figures show the results presented in [6]. In Figure 2.10, the red diamonds represent the harmonics of the respiration, the violet circles that of the cardiac signal, and the green squares that of the intermodulations.

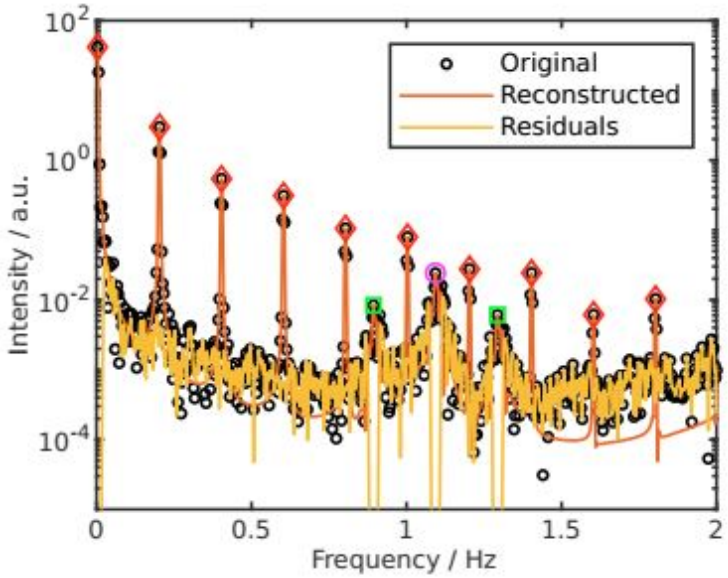

Figure 2.10: Global impedance signal in the frequency domain [6].

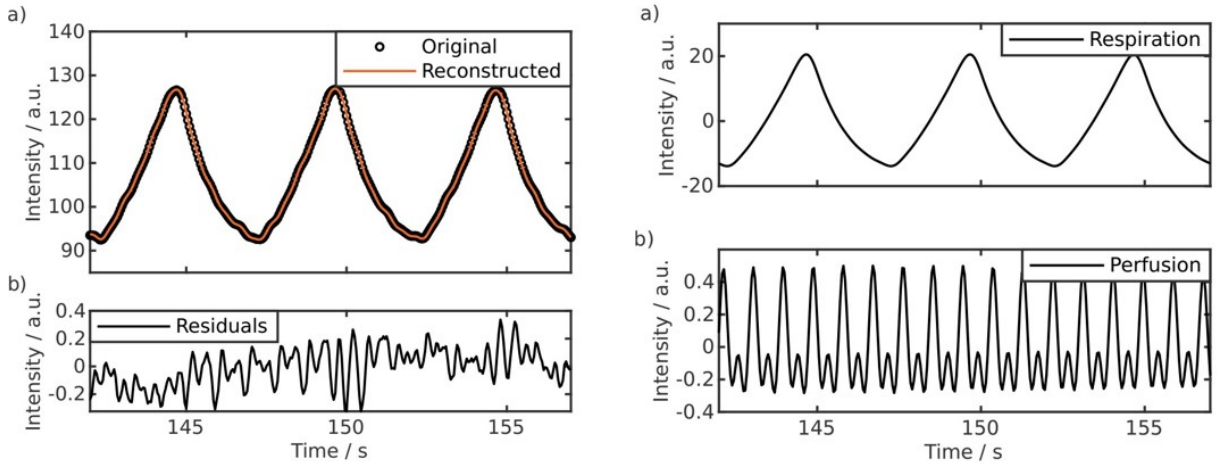

Figure 2.11: Left figure: Global impedance signal with its reconstruction (a) and residuals (b), right figure: Reconstructed VRS (a) and CRS (b) [6].

Although the results look promising, a possible real-time implementation should be discussed. One option might be to implement the so-called Dynamic harmonic regression as presented, for example, by Peter C. Young et al. in [20]. The authors described their method as a flexible approach to non-stationary time series analysis that, from the computational standpoint, benefits mainly from using an extremely fast alternative to the maximum likelihood estimation [20].

A much easier way would be to perform the proposed harmonic regression on a measured signal window of a specific size. However, the algorithm must be fast enough to perform the separation until the new window is available. Moreover, the window length would probably be treated as a parameter for optimization or even implemented as adaptive to changing fundamental frequencies in the input signal.

2.2.4 Comb filtering

Comb filtering is a well-established audio processing method with several advantageous properties that can benefit the source separation algorithm. Although no renowned publications on comb filters used for source separation in EIT were found, there are several publications on notch filters used for movement artifacts (MA) removal in photoplethysmography (PPG) signal, e.g., [21], [22], [23] and ECG noise removal, e.g., [24], [25], [26].

In simple terms, a notch filter is a very narrow band-stop filter, whereas creating a comb filter usually means applying more notch filters in a cascade. The purpose of a notch filter is to suppress the exact given frequency in the input signal. Figure 2.12 shows the

frequency response of an exemplary comb filter with the notch frequency of 1 kHz and its second and third harmonics.

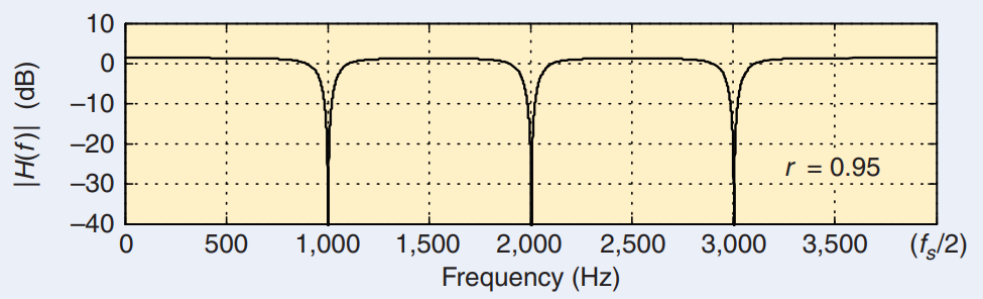

Figure 2.12: Frequency response of a comb filter [27]

Since the so-called finite impulse response (FIR) filters require high orders to achieve a narrow bandwidth (high selectivity), infinite impulse response (IIR) filters are usually used as notch filters instead. In [28] or [27], the implemented second-order notch filters are designed with a typical transfer function

$$H(z) = \frac{1 - 2\cos(\omega_n)z^{-1} + z^{-2}}{1 - 2r\cos(\omega_n)z^{-1} + r^2 z^{-2}}, \tag{2.20}$$

where $\omega_n = \frac{2\pi f_n}{f_s}$ with f_n being the notch frequency and f_s the sampling frequency. The r parameter controls the filter's bandwidth and should be set close to, but less than, one to achieve narrowband notches and avoid filter stability problems [27].

All the publications mentioned in the first paragraph of this section provide good algorithms for PPG signal enhancement or ECG noise removal. However, to keep this section concise, only one of the publications is described below as a general example of a notch filtering application.

In [21], Q. Zhang et al. presented a new method for motion artifact removal in PPG. As explained by the authors, the proposed method utilizes accurate HR estimation to first suppress the HR and its second harmonic in the raw PPG signal. The clean PPG signal is then recovered by subtracting the notch-filtered result from the raw signal.

The authors of [21] introduced a novel HR correction stage to improve the accuracy of HR estimation. They combined the estimation algorithm with a band-pass filter and an LMS-Newton adaptive filter based on adaptive noise canceling. Figure 2.13 describes the complete processing pipeline of the proposed algorithm, and in Figure 2.14, the results presented in [21] are shown.

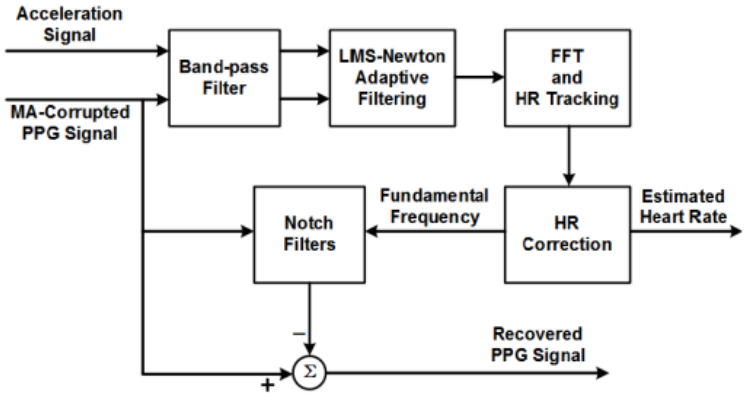

Figure 2.13: Complete signal processing pipeline presented in [21].

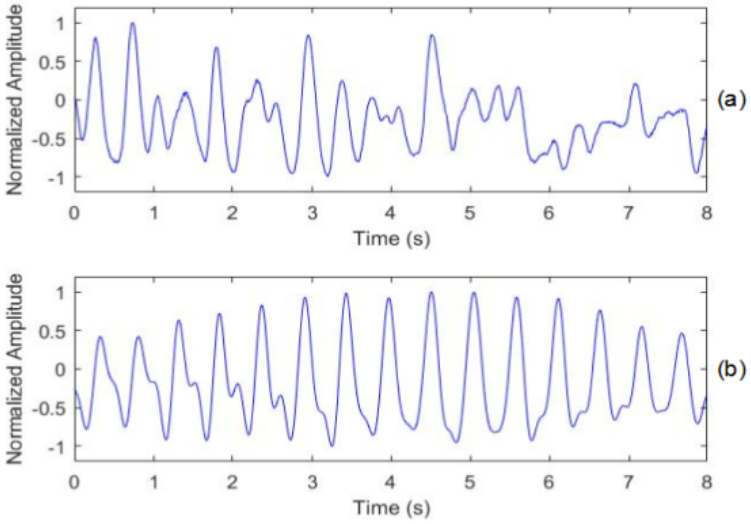

Figure 2.14: MA-corrupted raw PPG signal (a) and clean PPG signal (b) [21].

The results presented in [21] look highly promising. Moreover, the proposed algorithm is adaptive thanks to the combination of notch filtering with accurate HR estimation performed on the windowed input signal. Therefore, a real-time implementation should be possible using the windowing technique.

2.3 Multi-pitch estimation in EIT

The performance of all source separation methods based on the frequency domain analysis, such as the harmonic regression or comb filtering, highly depends on the accuracy of fundamental frequency estimation. In general, there are two possible approaches on

how to implement the RR and HR estimation. It can either be incorporated inside the source separation algorithm, making it self-adaptive (closed-loop approach), or performed by a different algorithm designed specifically for the frequency estimation (open-loop approach).

Advantage of the closed-loop approach is that the source separation is self-adaptive and utterly independent of any other algorithm. However, there might be some limitations to optimizing the frequency estimation while maintaining the overall accuracy and computation speed of the complete ensemble.

To address this, a well-established and optimized multi-pitch estimation method is utilized in the open-loop approach. The source separation algorithm then uses the estimated frequencies for the separation. This allows for independent optimization and comparison of the algorithm components, potentially making the results more accurate. However, it can be computationally ineffective since it increases the complexity of the complete ensemble.

In simple terms, the so-called multi-pitch estimation is a general name for various frequency estimation and tracking algorithms, well-know in audio and speech processing [29], [30], [31]. Some concepts can easily be adapted to estimate RR and HR from the mixed EIT signal. Such methods are mainly based on frequency domain analysis, and in the following sections, two of them are described in detail.

2.3.1 Grid search

The basic idea of grid search is very similar to harmonic regression. The EIT signal is assumed to be composed of a sum of sine and cosine functions with different fundamental frequencies. In [32], D. F. Silva and S. Leonhardt published the results of their development of a grid search-based algorithm for RR and HR estimation in EIT.

The proposed algorithm uses a grid of predefined frequencies for the parallelized harmonic regression in the time domain. A score function based on linear least squares (LLS) combined with the so-called Laplacian prior is then used to find RR and HR simultaneously, based on the EIT signal reconstruction [32]. Moreover, the algorithm uses the windowed input signal to simulate a real-time implementation.

The proposed application of grid search in EIT source separation is based on the fact that mixed EIT signal is mainly composed of the VRS, CRS, their intermodulation, and noise. If the noise is neglected, the discretized superposition of the signal components $x(t)$ can be described in the frequency domain by the intertwining harmonics of RR and HR [3] and a set of harmonics corresponding to the intermodulation with a fundamental frequency IR = HR - RR [33].

However, since the proposed algorithm utilizes only a two-dimensional frequency grid (one dimension for RR and the other for HR), the intermodulation component is also neglected. Therefore, as explained in [32], discrete signal model with sampling period Δt can be expressed in the time domain as a sum of sine and cosine functions using the following equation:

$$y(k) = \sum_{i=1}^{2} \sum_{l=1}^{N_i} \lambda_{i,l} \cos(2\pi l f_{0,i} k \Delta t) - \gamma_{i,l} \sin(2\pi l f_{0,i} k \Delta t), \tag{2.21}$$

where $\mathbf{f_0} = [f_{0,RR}, f_{0,HR}]^T$ is the set of fundamental frequencies distinguished by $i = \{1, 2\} \hat{=} \{RR, HR\}$, and N_i is the number of harmonics associated with each fundamental frequency $f_{0,i}$. The scalars $\lambda_{i,l} = A_{i,l} \cos(\phi_{i,l})$ and $\gamma_{i,l} = A_{i,l} sin(\phi_{i,l})$ encode both the amplitude and phase information of the signal. The explained parameters are gathered in a column-vector $\theta_{\mathbf{LLS,i}} = [A_{i,1}, ..., A_{i,N_i}, \phi_{i,1}, ..., \phi_{i,N_i}]^T$ corresponding to the fundamental frequency $f_{0,i}$ [32].

As further described by the authors, the equation 2.21 in matrix notation becomes

$$\mathbf{y} = \mathbf{M}(\mathbf{f_0}) \cdot \theta_{\mathbf{LLS}}, \tag{2.22}$$

where $\mathbf{y}$ is the input signal, $\mathbf{M}(\mathbf{f_0})$ is a regression matrix containing the sums of sine and cosine functions associated with the fundamental frequencies $\mathbf{f_0}$, and $\theta_{\mathbf{LLS}}$ is a matrix comprised of the parameter vectors [32].

Therefore, when knowing $\mathbf{f_0}$ defined with the frequency grid and, consequently, $\mathbf{M}(\mathbf{f_0})$, an estimation of $\theta_{\mathbf{LLS}}$ is obtained for each point in the frequency grid using LLS:

$$\hat{\theta}_{\mathbf{LLS}}(\mathbf{f_0}) = (\mathbf{M}^T(\mathbf{f_0})\mathbf{M}(\mathbf{f_0}))^{-1} \mathbf{M}^T(\mathbf{f_0})\, \mathbf{y}. \tag{2.23}$$

After the linear regression is performed with the known $\hat{\theta}_{\mathbf{LLS}}$ and the signal estimation $\hat{\mathbf{y}}$ is available, the best estimation of the RR and HR $\hat{\mathbf{f}}_\mathbf{0} = [\hat{f}_{0,RR}, \hat{f}_{0,HR}]^T$ is found by minimizing the estimation error:

$$\hat{\mathbf{f}}_0 = \min_{\mathbf{f0}} \mathrm{E}(\mathbf{f}_0) = \min_{\mathbf{f0}} ||\mathbf{y} - \mathbf{M}(\mathbf{f_0}) \cdot \hat{\theta}_{\mathbf{LLS}}(\mathbf{f_0})||^2. \tag{2.24}$$

The authors of [32] perform a simple validation using a signal created with the EIT synthesizer presented in [34] and briefly described in section 2.4. The validation signal is defined as a weighted sum of the generated cardiac and respiratory signals with weights $\omega_{card} \in \{0.1, 0.2, ..., 0.9\}$, $\omega_{resp} \in \{0.1, 0.2, ..., 0.9\}$, and $\omega_{card} + \omega_{resp} = 1$. Common accuracy metrics, namely the root mean square error (RMSE), bias (offset), and Bland-Altman plot (see 3.4.2) are used.

Figure 2.15 shows the RMSE values for all ω_{card} and ω_{resp} combinations. It is found that the implemented algorithm works best when $0.3 \leq \omega_{card} \leq 0.7$, and no reasonable accuracy can be achieved when the amount of VRS and CRS in the input signal is significantly

different [32]. This is expected since the linear regression described above assumes the input signal as a superposition of the VRS and CRS, both represented equally.

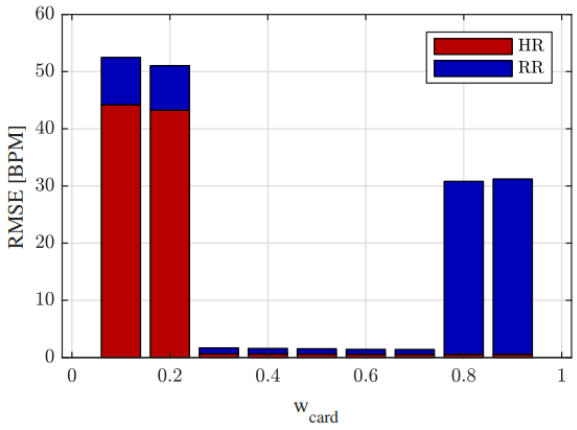

Figure 2.15: Total estimation RMSE for all ω_{card} values [32].

Figure 2.16 shows the estimates compared to the true values of RR and HR. The results look highly promising when considering only the values of ω_{card} associated with reasonable accuracy. Also, the Bland-Altman plot proves that the estimation does not show any significant trend, and the bias and limits of agreement (LoA) are small.

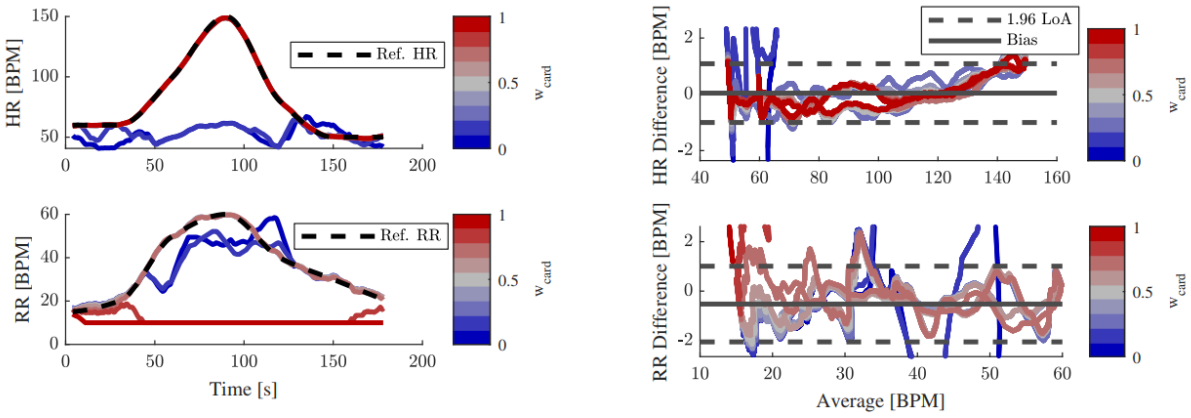

Figure 2.16: RR and HR estimates (left) and Bland-Altman plots (right) [32].

2.3.2 Continuous local interval estimator (CLIE)

The CLIE algorithm was initially presented by Christoph Brüser et al. in [35] for the derivation of beat-to-beat intervals from ballistocardiography (BCG). Five years later, in [36], Christoph Hoog Antink et al. published promising results of their investigation on possible CLIE application for HR variability derivation from photoplethysmography.

According to the authors of [35], the local interval length T_k and the local frequency f_k at the time point t_k where the heartbeat occurs can be defined as

$$T_k = t_k - t_{k-1}, \tag{2.25}$$

$$f_k = \frac{1}{T_k}, \tag{2.26}$$

where $k = \{2, ..., N\}$ with N being the number of detected heartbeats. As the authors explain, CLIE aims to estimate T_k from the signal's fundamental frequencies directly. Such an approach is inspired by the pitch tracking method, well-known in speech processing and widely used for continuous and real-time fundamental frequency estimation [35].

As described in [35], CLIE uses three fundamental frequency estimators to increase the robustness of estimation on a moving processing window. However, instead of being designed to contain multiple oscillations of the fundamental frequency, the processing window size is set so that the window includes only two heartbeats. The three interval estimators are modified auto-correlation S_{Corr}, modified average magnitude difference function S_{AMDF}, and maximum amplitude pairs S_{MAP} [35].

However, in [36], C. H. Antink et al. presented some changes regarding their application of CLIE. The first estimator, the so-called lag-adaptive short-time autocorrelation (LASTA) score function, is described as

$$S_{LASTA}(\eta) = \frac{1}{\eta} \cdot \sum_{\nu=0}^{\eta} \omega[\nu] \cdot \omega[\nu - \eta], \tag{2.27}$$

where $\omega[\nu]$ is the analysis window and η is a respective lag. The modified second and third estimators are

$$S_{AMDF}[\eta] = \left[\frac{1}{\eta} \sum_{\nu=0}^{\eta} |\omega[\nu] - \omega[\nu - \eta]| \right]^{-1}, \tag{2.28}$$

$$S_{MAP}[\eta] = \max_{\nu \in \{0,...\eta\}} \left(\omega[\nu] + \omega[\nu - \eta] \right). \tag{2.29}$$

This ensures that the exact number of samples necessary for each candidate lag ν is considered [36].

Whereas the authors of [35] used a probabilistic estimator fusion to obtain a combined score function, the fusion presented in [36] is different. As claimed by C. H. Antink et al., the estimation accuracy is improved by defining the fused score function

$$S_{fused}(\eta) = S_{LASTA}(\eta) \cdot S_{AMDF}(\eta) \cdot S_{MAP}(\eta). \tag{2.30}$$

To increase the robustness of the estimation, the authors of [36] introduced a lag-adaptive prior. Such prior uses the previously estimated intervals to improve the current estimation. According to the authors, the MIT-BIH Arrhythmia database was analyzed and the Laplace distribution using the median of 10 previous estimates is implemented. Since the

prior is adapted by D. F. Silva and S. Leonhardt in [32], it is described in more detail in section 3.2.2.

Finally, as presented in [36], the optimal interval is equal to the optimal lag η^* found by maximizing the combined score function:

$$\eta^*[i] = \arg\max_{\eta}(S_{fused}[i,\eta] \cdot S_{prior}[i,\eta]). \tag{2.31}$$

Moreover, a post-processing moving median filter is utilized to remove the estimation outliers.

For the performance assessment of the proposed algorithm, the authors of [36] used the same metrics as the authors of [32]. RMSE, bias (offset), and the so-called Bland-Altman plot are utilized to compare the results of CLIE and CLIE with Laplace prior ($CLIE_p$) to some of the well-established HR estimation methods, specifically peak-to-peak (P2P), peak-to-peak of the first derivative (P2P'), troth-to-troth (T2T), CLIE, and . Table 2.1, presented in [36], compares beat-to-beat estimation errors.

	absolute error [ms]		relative error [%]	
method	offset	RMS	offset	RMS
P2P	-0.19	13.96	-0.0057	1.63
P2P'	**-0.09**	17.94	-0.0071	2.06
T2T	-0.12	11.90	**0.0008**	1.27
CLIE	-0.19	**10.68**	-0.0061	**1.16**
$CLIE_p$	-0.35	11.45	-0.0168	1.23

Table 2.1: Beat-to-beat interval estimation errors [36].

Figure 2.17 shows the Bland-Altman plots. When analyzing the displayed results and the results shown in Table 2.1, it is clear that the CLIE and the $CLIE_p$ achieve a comparable accuracy to the other, already well-established, methods.

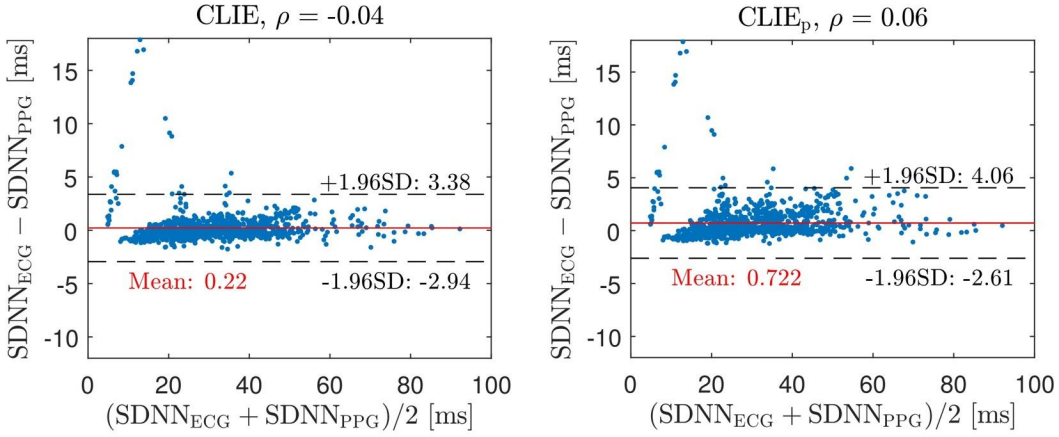

Figure 2.17: Bland–Altman plots presented in [36].

2.4 EIT signal synthesis

When performing an EIT measurement in patients, only a mixed EIT signal can be acquired. As a consequence, it is impossible to compare the separated signals to the ground truth when validating a source separation algorithm. However, when synthesizing a mixed EIT signal from the given VRS and CRS, the ground truth is known.

Use of a synthesized EIT signal in source separation was already presented in [32], described in section 2.3.1. In [37], the so-called source consistency method was used to synthesize boundary voltage data for EIT.

2.4.1 Anatomical models

There are two general approaches to modeling the impedance changes in the thorax. The first one is to model the physiological properties of the cardiorespiratory system as faithfully as possible, which inevitably results in complex anatomical models.

For example, in 2017, Martin Proença published a thesis [38] where he developed a 4D bioimpedance model of the human thorax. The main focus of the included model-based feasibility study is to simulate peak arterial pressure (PAP)-affecting pathologies and enable the estimation of the pulmonary pulse transit time based on the PAP measurement.

The model presented in [38] consists of an anatomically realistic static 3D model of the whole pulmonary arterial tree combined with a dynamic model of pulmonary circulation. The model is transformed into a 4D bioimpedance model by describing how the pressure-induced distension of the pulmonary arteries affects the conductivity at each location in the lungs [38].

Finally, the so-called Maxwell Garnett mixing formula [39] is used to obtain conductivity values. It combines lung tissue as a dielectric medium with conductivity inclusions from blood vessels. Since D. F. Silva and S. Leonhardt adopted this approach in [40], it is described in more detail in section 3.3.1.

Figure 2.18: Visualization of the anatomical model of the pulmonary arterial tree [38].

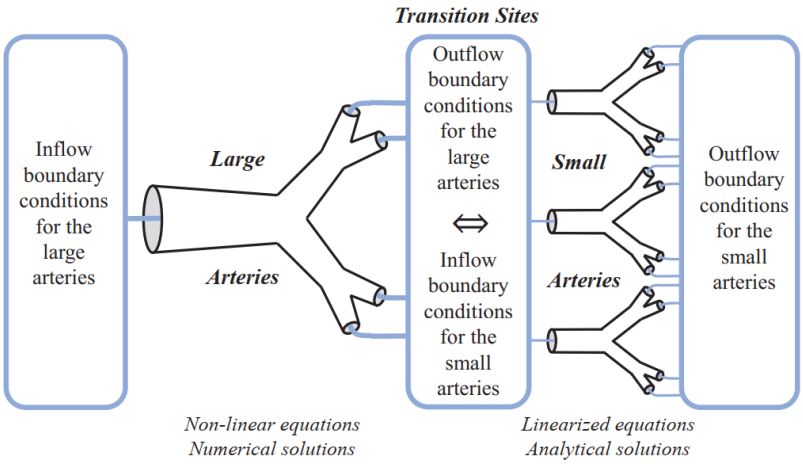

Figure 2.19: Structure of the global model of the pulmonary circulation [38].

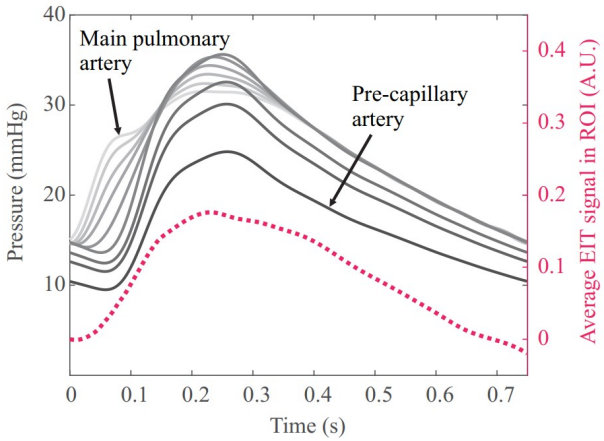

Figure 2.20: Generated pressure waves and average EIT signal in a pulmonary ROI [38].

2.4.2 Mathematical models

The second approach is to model the function of the cardiorespiratory system using mathematical models mimicking the system's behavior. For example, in 2017, C. H. Antink et al. published their framework for multimodal cardiorespiratory signals synthesis [34]. The presented model consists of two general parts: **(a)** six modality-independent coupled oscillators and **(b)** modality-dependent waveform generators, which utilize various template functions.

According to the authors, the coupled oscillators are described with nonlinear ordinary differential equations, including RR and HR parameters and the modulation functions to simulate physiological processes such as Mayer oscillations. It is to be noted that due to

the nonlinear coupling, the solution of the differential equations is too complex. Therefore, a numerical solution is found using the Runge-Kutta method [34]. Figure 2.21 shows the overall structure of the synthesizer.

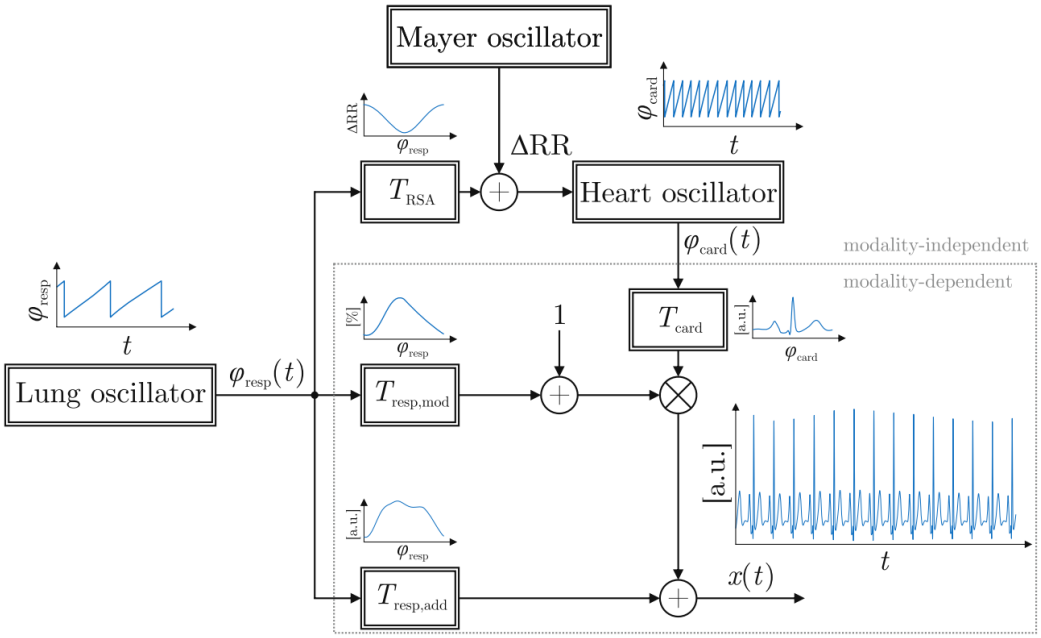

Figure 2.21: Overall structure of the synthesizer [34].

As further presented in [34], measurements from three databases are used for validation. Therefore, different modality signals, namely respiration, ECG, blood pressure (BP), BCG, PPG, and flow signals, are synthesized and compared to the ground truth. Figures 2.22 and 2.23 show some of the presented results.

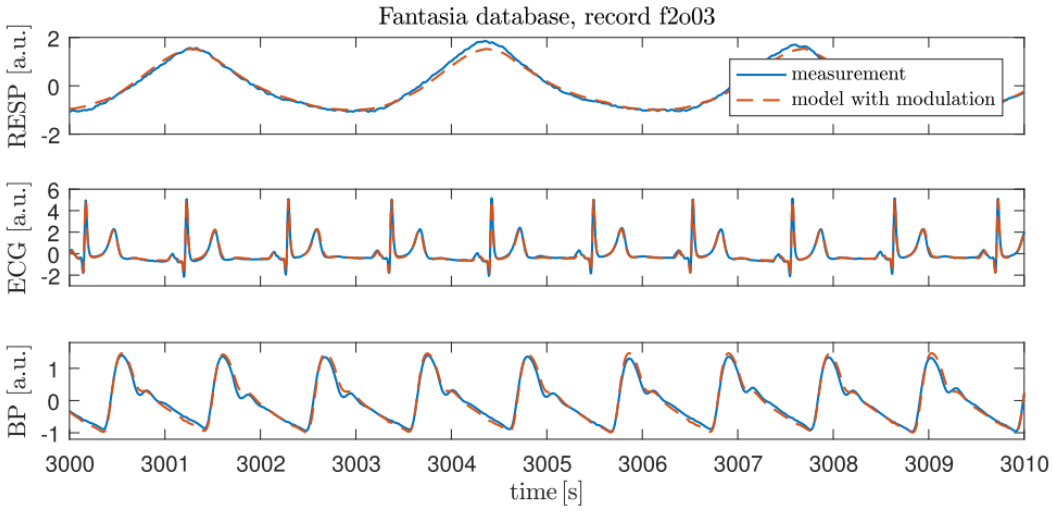

Figure 2.22: Measured and synthesized respiration, ECG, and BP signals [34].

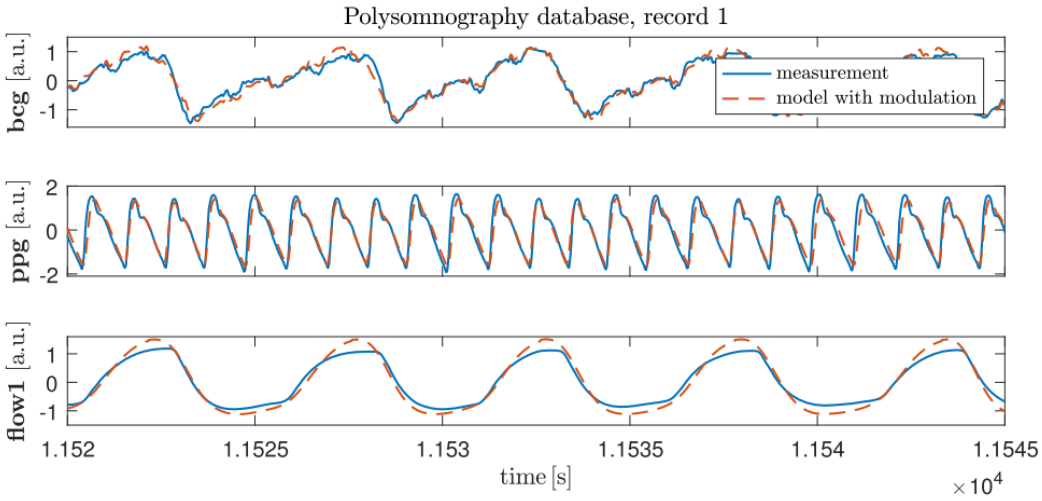

Figure 2.23: Measured and synthesized BCG, PPG, and flow signals [34].

As shown by the authors, the synthesizer presented in [34] generates the signals with correct phase relationships and mimics several aspects of physiological coupling. However, as the authors admit, the model does not allow for a respiratory pattern or amplitude change [34].

3 Methods and implementation details

This chapter describes the implementation of the multi-pitch estimation and source separation algorithms in MATLAB software in detail. As shown in section 2.2, there are several approaches to be considered for real-time source separation in EIT. However, some of them are more suitable than the others. Therefore, this chapter starts with their comparison. The reasons for the chosen methods are given and their implementation is described in detail.

Next, the EIT signal synthesizer utilized to simulate a validation signal is presented. The input parameters for the synthesizer are explained and the signal itself is analyzed in detail in the time and frequency domains.

Finally, the performance assessment metrics used for the validation and comparison of the implemented algorithms are explained.

3.1 Comparison of available methods

It was shown in [4] that the methods based on PCA can achieve good separation of the EIT signal components while keeping the algorithm easy to understand and the results interpretable. However, they cannot model temporal dynamics and, therefore, adapt to non-stationary signals. When the windowing method is applied, the algorithm is expected to provide the separation results for each sample quick enough to follow the EIT frame rate of at least 50 fps.

Although there are some possible real-time or at least dynamic PCA implementations, e.g., [41] or [42], such implementation would cost a lot of additional effort. As already explained in 2.2.1, the algorithm implementation presented in [4] cannot work in real-time. Another concern is that even if a more computationally efficient real-time implementation is developed, it might still require higher computational power than is usually available at the bedside.

In [5], the authors presented very promising results of their separation algorithm based on EMD. Because the EMD was initially developed as a frequency domain analysis method for non-stationary signals, its biggest advantage is that it can model the temporal dynamics and, therefore, adapt to the changes in the input signal. However, since the mathematical background behind EMD is quite complex, the method is harder to understand and the interpretation of the results is less convenient than with PCA. Moreover, for a real-time implementation, the windowing method has to be used.

There are several real-time implementations of EMD, e.g., [43], [44], and [45]. Therefore,

the authors can be trusted when claiming in [5] that a real-time implementation should be possible in the near future, even though their algorithm is actually based on slightly more complex approach, MEEMD. However, there are still similar concerns as with PCA when a real-time implementation at the bedside with a limited computational power of the hardware is considered.

As presented in [6], linear regression can be performed in the frequency domain to separate the VRS and CRS in the mixed EIT signal. Such approach is simple to understand and the results are easily interpretable. The real-time implementation using the input signal windowing seems feasible since linear regression is usually computationally very effective and it should be quite easy to modify the algorithm proposed in [6].

However, there is still one method considered more suitable for a simple proof-of-concept algorithm. In section 2.2.4, various applications of comb filtering on biosignal processing are presented. Comb filtering seems to work well for MA removal in PPG signals and noise removal in ECG signals as long as the HR is estimated accurately.

Moreover, since signal filtering is usually very fast, a real-time implementation able to perform the separation with each new sample, i.e., with the frequency of 50 Hz, should be feasible with no concerns. At the top of that, the filtering is incredibly easy to understand and the results can be interpreted directly.

3.2 Implementation of the selected methods

After thoroughly analyzing the already published approaches, comb filtering is selected to be implemented in this work as a proof-of-concept for real-time source separation in EIT. It is decided to take the open-loop approach and first implement the multi-pitch estimation methods, described in section 2.3, in real-time and enhance their performance to achieve as accurate as possible estimation of HR and RR. Next, the estimated frequencies are used as the inputs of a simple comb filtering algorithm in combination with standard filtering methods, such as LP and HP filtering, and some post-processing.

Figure 3.1 shows a complete signal processing pipeline. For clarity, each pipeline block is explained one by one in the following sections. In each section, a brief theoretical introduction is followed by the implementation details. However, a thorough validation and comparison of all the implemented algorithms are provided in chapter 4.

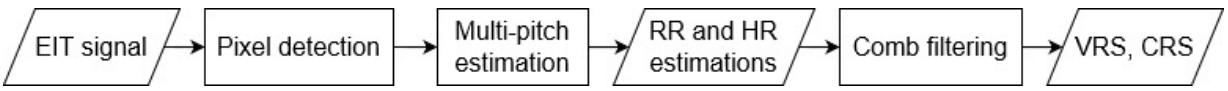

Figure 3.1: A diagram showing the complete signal processing pipeline.

3.2.1 Pixel detection algorithm

The pixel detection algorithm is a simple tool for finding EIT image pixels with a defined ratio of component representation based on frequency domain analysis. Its primary purpose is to find the balanced signal for the grid search algorithm, which performs best when the VRS and CRS are represented equally in the input signal, as already explained in section 2.3.1. Moreover, the CLIE algorithm presented in section 2.3.2 and modified in this work to estimate both RR and HR utilizes the pixel detection algorithm to find the ventilation-dominated and cardiac-dominated signals, as explained in 3.2.3.

Although the pixels can easily be selected by location in the image, such selection cannot assure the given ratio of component representation. Therefore, the whole EIT image sequence (EIT video) is first transformed from the time domain into the frequency domain using Fast Fourier Transform (FFT) implemented in MATLAB. Next, the component representation ratio

$$R = \frac{A_{c,max}}{A_{r,max}} \tag{3.1}$$

is calculated for each pixel using maximum amplitudes in pre-defined frequency bands for cardiac activity ($A_{c,max}$) and for respiration ($A_{r,max}$).

The frequency bands are defined as 0.17 Hz (10 breaths per minute (bpm)) to 0.5 Hz (30 bpm) for respiration and 0.67 Hz (40 beats per minute (bpm)) to 3.33 Hz (200 bpm) for cardiac activity. These values are set with the basic knowledge of typical RR and HR values.

After the component representation ratios R are found, the algorithm chooses the pixels where the dominance ratio is as close as possible to the given value, e.g., 1.0. However, if the cardiac-dominated signal is required, the pixel with maximum R_D is selected. Similarly, when the respiration-dominated signal is needed, the pixel with minimum R_D is selected.

The implemented pixel detection algorithm is tested with satisfying results. Since its outputs are used to validate and compare the implemented multi-pitch estimation and source separation algorithms, see chapter 4 for more details and figures.

However, it is to be noted that for a real-time implementation, only a small portion of the EIT image sequence, e.g., a setup period of 10 seconds with stable RR and HR, should be used. After the setup period, the selected pixels would be fixed, and the source separation would be performed with each new sample without the pixel detection algorithm. For this reason, the computational time needed for pixel detection is further considered unimportant.

3.2.2 Multi-pitch estimation using grid search

The general principle of a grid search approach is well-known. A set of given values is exhaustively searched to find the optimal ones. The grid search implemented in this work is based on the algorithm presented in [32] and described in detail in section 2.3.1.

Reminding the basics, it utilizes a predefined 2D grid of frequencies for the input EIT signal reconstruction with linear regression. Thus, finding the best-matching reconstructed signal best estimates the RR and HR. Moreover, the input signal is processed using a sliding window to simulate a real-time application.

However, after testing the original implementation presented in [32], it is still necessary to significantly reduce the computational time and make the algorithm parameters adaptive to the changing RR and HR input signal. Therefore, significant modifications are introduced in this section. Four different versions of the complete algorithm are implemented and tested. However, a thorough validation and comparison is provided in section 4.1.1 as well as the parameter optimization in section 4.2.1.

Original implementation

Once the grid search algorithm is initiated, the 2D frequency grid of $\mathbf{f_0} = (f_{RR}, f_{HR})$ is initialized, and all the respective regression matrices $\mathbf{M}(\mathbf{f_0})$, described in section 2.3.1, are calculated. When applied to real-time signals, the algorithm needs a period corresponding to the processing window length W to calculate the first estimation assigned to the sample located right at the end of the window. The value of W is found empirically as 180 samples. Considering the EIT frame rate (sampling frequency) f_s of 50 fps (Hz), this corresponds to 3.6 seconds.

The following estimates are calculated immediately one by one since the sliding window shift is set as one sample. This is suitable for the real time application where the samples are processed continuously one by one.

Among other parameters, the accuracy of the grid search algorithm depends on the grid resolution. In [32], the grid step is defined as 2.5 bpm in both RR and HR. During the algorithm development and testing in this work, this value is changed slightly to 2.0 bpm, while further changes are not beneficial for the overall algorithm performance. Table 3.1 shows all the grid parameters.

i	$\Delta f_{0,i}$ (bpm / Hz)	$f_{0,i,min}$ (bpm / Hz)	$f_{0,i,max}$ (bpm / Hz)
RR	2.0 / 0.03	10 / 0.17	60 / 1.00
HR	2.0 / 0.03	40 / 0.67	200 / 3.33

Table 3.1: Parameters of the frequency grid.

After performing the linear regression and finding the EIT signal estimation for each point in the frequency grid, the estimation errors described by equation 2.24 are inverted to represent a linear least squares score function $S_{LLS}(\mathbf{f_0})$.

As explained in [32], a compound Laplacian prior $S_{LAP}(\mathbf{f_0}, \tilde{\mathbf{f}}_\mathbf{0})$, adapted from [36], is defined as

$$S_{LAP,i}(f_{0,i}, \tilde{f}_{0,i}) = \frac{1}{2b_i} \cdot e^{-\frac{|f_{0,i} - \tilde{f}_{0,i} - 1|}{b_i}}, \tag{3.2}$$

where $\tilde{f}_{0,i}$ is the median of previous n estimates, representing a location parameter of the Laplace distribution $\mu = \tilde{f}_{0,i} + 1$. Parameter $b_i > 0$ is a scale parameter, sometimes referred to as diversity.

As shown in Figure 3.2, the Laplacian prior smoothens the score function. The value of n is set accordingly to [36] and [32] as ten samples. However, it is to be further optimized as well as the values of $\mathbf{b} = \{b_{RR}, b_{HR}\}$. Therefore, the optimal values are shown in section 4.2.1.

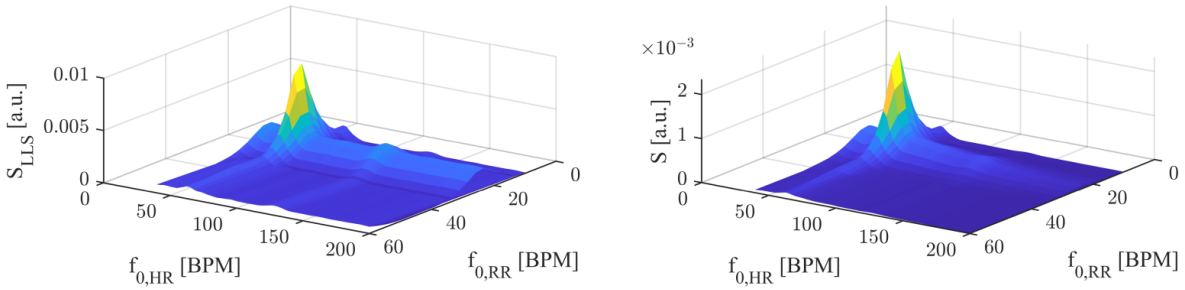

Figure 3.2: Example of S_{LLS} (left picture) and combined score S (right picture) [32].

Next, both S_{LLS} and S_{LAP} are normalized so that the sum of their values equals one. That makes it possible to treat the scores as probabilities and combine them into the overall estimation score

$$S(\mathbf{f_0}, \tilde{\mathbf{f}}_\mathbf{0}) = S_{LLS}(\mathbf{f_0}) \cdot \prod_{i=1}^{2} S_{LAP,i}.(f_{0,i}, \tilde{f}_{0,i}). \tag{3.3}$$

Finally, maximizing the score function gives the best estimation of $\mathbf{f_0}$. Since no post-processing is implemented in the original version or the others, the RR and HR estimation is given as

$$\hat{\mathbf{f}}_\mathbf{0} = \arg\max_{\mathbf{f_0}} S(\mathbf{f_0}, \tilde{\mathbf{f}}_\mathbf{0}). \tag{3.4}$$

Laplace prior thresholding

The second algorithm version introduces the most beneficial upgrade from the computational time standpoint, as shown in section 4.1.1. The idea behind Laplace prior thresholding is that there is no need to perform the linear regression with all the frequencies in the predefined grid for each input signal sample when there is already some information about the most promising estimates available.

Therefore, once the S_{LAP} is known for the given sample, only the frequencies corresponding to $S_{LAP} \geq h$, where h is the given threshold, are calculated. Since the Laplace distribution slightly changes with each new sample, the threshold is implemented as adaptive using

$$h = p \cdot \max(S_{LAP}), \tag{3.5}$$

where $p \in (0, 1)$ is ideally the highest possible value that results in no loss in estimation accuracy. The initial value of p is found empirically as 0.75 while subject to parameter optimization described in section 4.2.1. Eventually, this modification is found very beneficial without having any drawbacks as shown in section 4.1.1 and, therefore, is implemented in the following grid search algorithm versions as well.

Adaptive parameters

In the third implemented version, the algorithm's parameters are modified to be adaptive. First, the adaptive processing window length is introduced. Due to the limitations of the original implementation, the adaptive processing window is incorporated into the existing code as a cropping window of size m that allows only a smaller portion of the processing window for regression calculations.

A proportional relation of m to the previously estimated frequencies is empirically found to make it adaptable to the changes in estimated RR and HR, thus improving the accuracy of the estimation. The relation is given by equation

$$m = 2 \cdot f_s \cdot \left(\frac{\sum_{i=1}^{2} \tilde{f}_{0,i}}{2} \right)^{-1}, \tag{3.6}$$

where $\tilde{f}_{0,i}$ is the median of n previously estimated frequencies as defined already for Laplacian prior. Moreover, it increases the estimation robustness of a potential real-time application of the grid search algorithm.

Consequently, the processing window size W is re-defined as

$$W = \frac{2.5 \cdot f_s}{f_{0,RR,min}} = 750\,\text{samples} \mathrel{\hat{=}} 15\,\text{s} \tag{3.7}$$

to always accommodate at least 2.5 cycles of respiration and omitted from further parameter optimization.

Finally, it makes sense to also modify n accordingly to m with equation

$$n = r \cdot m, \tag{3.8}$$

where $r \in (0, 1)$. The value of r is initially set as 0.15 while being subject to parameter optimization described in section 4.2.1. Therefore, its final optimal value is shown there.

Super-resolution

Finally, the benefits of the so-called super-resolution are investigated in the last implemented version of the grid search algorithm. Super-resolution is a well-known approach in image processing that aims to approximate the image values between the defined pixels, thus seemingly increasing the image resolution. There are many examples of super-resolution algorithms, such as [46] and [47].

In this work, a 2D bilinear interpolation is implemented, utilizing a 2D Taylor series approximation to estimate the values of the combined score function S between the predefined points of the frequency grid.

As explained, for example, in [48], two-dimensional Taylor series of $f(x, y)$ around the point (a, b) is generally given by equation

$$\begin{aligned} f(x,y) = f(a,b) + f_x(a,b)(x-a) + f_y(a,b)(y-b) + \frac{1}{2!}[f_{xx}(a,b)(x-a)^2 \\ + 2f_{xy}(a,b)(x-a)(y-b) + f_{yy}(y-b)^2] + ..., \end{aligned} \tag{3.9}$$

where $f_x = \frac{df(x,y)}{dx}$ and $f_y = \frac{df(x,y)}{dy}$ are the first-order partial derivatives of $f(x, y)$ while $f_{xx} = \frac{df(x,y)}{dx^2}$, $f_{xy} = \frac{df(x,y)}{dxdy}$, and $f_{yy} = \frac{df(x,y)}{dy^2}$ are the second-order partial derivatives of $f(x, y)$.

The best linear approximation of $f(x, y)$ around the point (a, b) is then given as

$$L(x, y) = f(a, b) + f_x(a, b)(x - a) + f_y(a, b)(y - b). \tag{3.10}$$

To implement Taylor series into the grid search algorithm, the first- and second-order derivatives are calculated for the neighboring points of the maximum overall estimation score S. The new peak is considered to be precisely where the first-order derivative of the interpolation function equals zero, and the second-order derivative is negative, which ensures concavity. With the new peak already known, the respective coordinates (x, y), in our case equal to (f_{RR}, f_{HR}), are found. If this peak is higher than the one found before, the final frequency estimates are changed.

Theoretically, the pre-defined frequency grid resolution does not limit the estimation accuracy when applying the super-resolution algorithm. This can be used to achieve better overall accuracy of the estimation with the same frequency grid, or the number of points in the grid can be lowered by setting higher $\Delta f_{0,i}$ while retaining approximately the same estimation accuracy but with lower computational time. However, as shown in section 4.1.1, the super-resolution does not perform as expected.

3.2.3 Multi-pitch estimation using CLIE

As already mentioned in section 2.3.2, the CLIE algorithm was initially presented by Christoph Brüser et al. in [35]. In this work, the original implementation for HR estimation from BCG signals is modified to estimate RR and HR from EIT signals. With the proposed iterative approach, CLIE is used twice to estimate RR and HR individually.

Two methods of the iterative approach are implemented as two different algorithm versions. However, both use the windowing technique to simulate a real-time application while the window shift is set as one sample. Similarly to the grid search algorithm, RR and HR are thus estimated sample by sample after the first signal window is available.

As shown in Figure 3.3, to obtain RR estimation, both versions start with filtering the windowed ventilation-dominated or balanced signal selected by the pixel detection algorithm (see section 3.2.1). Using a second-order Butterworth LP filter with a cutoff frequency $f_{c,LP} = 0.8$ Hz (48 bpm), the amount of high-frequency cardiac-related oscillations in the input signal is significantly reduced. The value of $f_{c,LP}$ is initially set with the author's knowledge of typical RR and HR values but adjusted empirically to improve the results. The LP-filtered signal is then processed with CLIE, and the RR is estimated.

However, the two proposed methods use different tools to obtain HR estimation. The first algorithm version utilizes a second-order Butterworth HP filter with a cutoff frequency $f_{c,HP} = f_{c,LP}$ to filter out low-frequency oscillations from the input cardiac-dominated signal selected by the pixel detection algorithm.

The second version uses a comb filter, described in detail in section 3.2.4, to separate the VRS from the balanced input signal. More specifically, the RR estimates obtained with CLIE are used as notch frequencies and the comb-filtered signal is then filtered with the same above-mentioned HP filter to separate any remaining low-frequency oscillations.

In the end, the HR is estimated by CLIE in both implemented versions. Figure 3.3 shows the two signal processing pipelines introduced by the two implemented versions of the iterative CLIE algorithm.

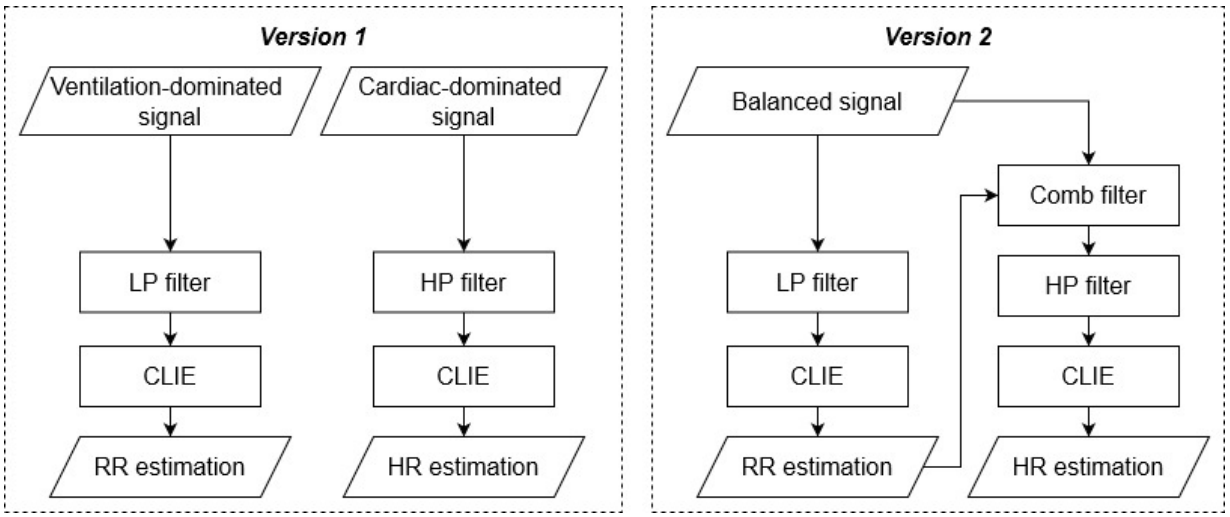

Figure 3.3: Processing pipelines of the two CLIE algorithm versions.

The CLIE implementation's critical parts have already been converted from MATLAB into C before. Thus, when CLIE is implemented in the proposed iterative approach, the estimation is already fast enough for a potential real-time application. However, some modifications, presented in the following section, are still necessary to improve the accuracy and robustness of the estimation. Moreover, a thorough validation and comparison of both implemented versions of the iterative algorithm are presented in section 4.1.2.

Modifications of the original implementation

The modified CLIE algorithm implemented in this work introduces two adaptive processing window sizes, one for RR and one for HR estimation. Therefore, the initial window sizes $W_{RR,1}$, $W_{HR,1}$ are set to include at least one cycle of the ventilation or cardiac activity using

$$W_{RR,1} = \frac{f_s}{f_{0,RR,min}} = 300\,\text{samples} \mathrel{\hat{=}} 6\,\text{s}, \tag{3.11}$$

$$W_{HR,1} = \frac{f_s}{f_{0,HR,min}} = 75\,\text{samples} \mathrel{\hat{=}} 1.5\,\text{s}, \tag{3.12}$$

where $f_{0,RR,min} = 0.17$ Hz (10 bpm) and $f_{0,HR,min} = 0.67$ Hz (40 bpm). Therefore, the initial delay needed to gather all the necessary samples for the first estimation of both RR and HR is 6 seconds.

After that, the estimated frequencies are available sample by sample, and the size of each following processing window is set equal to the previous interval estimation:

$$W_{i,j} = \hat{I}_{i,j-1}, \tag{3.13}$$

where $i = \{\text{RR, HR}\}$ denotes the type of estimation and j the current estimation sample. To add some robustness, the window size is changed every s_i-th sample only, while $\mathbf{s} = [s_{RR}, s_{HR}] = [50, 25]$ is set initially, but later subjected to parameter optimization described in section 4.2.2.

Moreover, a simple outlier detection is implemented to significantly reduce the number of outliers produced during the interval calculations. With the knowledge of the previously estimated interval, it is assured that the current estimation does not differ by more than 50 % from the previous one.

Finally, a post-processing median filter window sizes are initially set as $\mathbf{M} = [M_{RR}, M_{HR}] = [50, 25]$ while subjected to parameter optimization described in section 4.2.2. Because of the implemented outlier detection, the moving median window can be set much shorter than in the original CLIE implementation. This leads to much faster algorithm adaptability while not losing the smoothing ability of the median filter.

However, it is to be noted that in the actual real-time implementation, the median filtering would have to be performed on each processing window individually instead of the complete estimated signal.

3.2.4 Source separation using comb filtering

This section describes the implementation of a comb filter for source separation in EIT. As already mentioned in section 2.2.4, different publications describing various comb-filtering applications have some similarities. For example, many of them use notch filters in cascade to create a comb filter, accompanied by other filters, e.g., band-pass or moving average, to improve the results.

Since all the published results look promising, the implementation presented in this work takes a similar approach. However, the algorithms presented in section 2.2.4 are designed for motion-artifact removal in the PPG signal or noise removal in the ECG signal. Neither of them is explicitly developed for source separation in EIT.

Therefore, the critical task is first to prove that comb filtering is applicable for source separation in EIT and can produce valid results. The implementation presented here thus provides a proof-of-concept and possibly a starting point for more complex implementations.

Implementation details

A simple comb filtering algorithm is designed in the so-called open-loop approach, already explained in section 2.3. The implemented multi-pitch algorithms estimate the RR and HR accurately, ensuring the comb filter is also accurate and, more importantly, adapts its notch frequencies accordingly to the input signal.

The implementation of the filter itself is done in MATLAB using in-built functions *iirnotch* and *filtfilt*. According to MATLAB documentation [49], *iirnotch* returns the numerator and denominator coefficients of a digital second-order IIR notch filter. The user-defined parameters of the designed filter are the normalized frequency ω_0

$$0 < \omega_0 = f_n \cdot \frac{2}{f_s} < 1.0, \tag{3.14}$$

where f_n is the notch frequency in Hz,and the quality factor

$$Q = \frac{\omega_0}{B}, \tag{3.15}$$

where B is the bandwidth [49].

As explained in MATLAB documentation [50], filtering a signal with *filtfilt* means performing zero-phase digital filtering. In other words, the input signal is processed in both the forward and reverse directions using the given numerator and denominator coefficients of the transfer function. As a result, zero phase distortion is achieved, the magnitude of the transfer function is squared, and the filter order is doubled.

Zero phase distortion ensures that the features of the unfiltered signal in the time domain waveform are preserved precisely at the same locations after filtering [50]. Zero-phase filtering was successfully utilized, for example, by C. Park et al. in [22] for PPG signal enhancement.

The implementation of the comb filter algorithm developed in this work is inspired by those presented in papers mentioned in section 2.2.4, e.g., [27], [22], and [21]. The input signal is swept over with the sliding window. For simplicity, the windowing is performed without any overlap, and the window size is set empirically as 200 samples. However, it is to be noted that in a true real-time implementation, when comb filtering is combined with multi-pitch estimation, the window size would have to be the same as that introduced by the respective multi-pitch estimation algorithm.

For every window, three notch filters are designed to filter out the RR or HR harmonics. At this point, the VRS is filtered out in VRS separation, and analogously, the CRS is filtered out when performing CRS separation. The quality factor $Q = 1$ is set empirically for all notch filters. The comb filtering is then performed with the three notch filters in two cascades, one for VRS and the other for CRS separation.

Next, depending on the type of separation, the remaining signal is filtered with a second-order Butterworth HP or LP filter to remove any remaining low- or high-frequency components, respectively. The cut-off frequencies are set as $f_{c,HP} = 0.17$ Hz (10 bpm) and $f_{c,LP} = 3.33$ Hz (200 bpm).

Subsequently, the filtered signal is subtracted from the input signal. That way, the intermodulation component (and potentially some noise) is also filtered out in both the VRS and CRS separations. Since the CRS can be expected to be in the opposite phase with the VRS (see section 2.1.4), the separated CRS is multiplied by -1 to match the true signal.

Finally, to smoothen the transitions between the processing windows, a moving average window of size of 25 samples is utilized. Figure 3.4 shows the complete signal processing pipelines of the VRS and CRS separations.

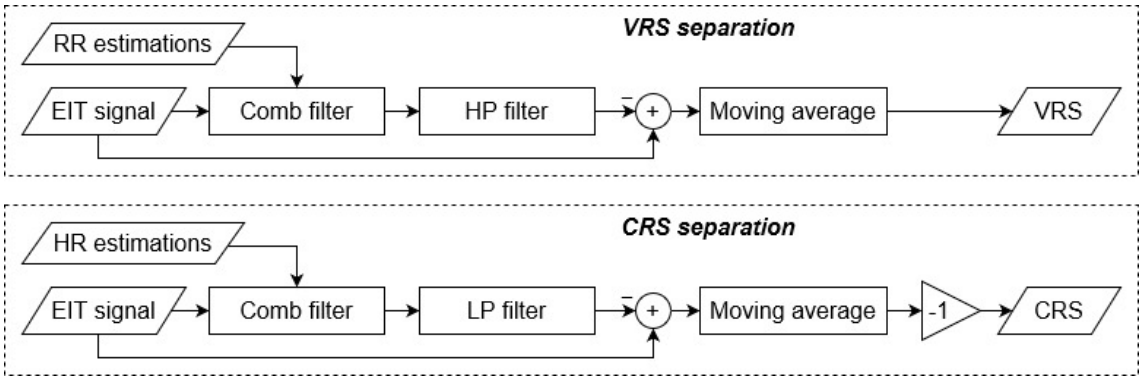

Figure 3.4: Processing pipelines of the implemented comb filtering algorithms.

3.3 Validation signal synthesis

A synthesized EIT signal is used to validate and compare all the implemented algorithms. That way, the outputs of the multi-pitch estimation and source separation algorithms can be compared to the ground truth, as already mentioned in section 2.4. Therefore, the following sections provide a detailed description of the utilized synthesizer and the generated validation signal.

3.3.1 EIT signal synthesizer

To synthesize the validation signal, Fast 4D FEM Model for EIT Source Separation Benchmarking [40] is used. This synthesizer is currently in development by D. F. Silva and S. Leonhardt at the chair of Medical Information Technology (MedIT) at RWTH Aachen

University, while being inspired by the model designed by M. Proença in [38], already introduced in section 2.4.

As explained in [40], D. F. Silva and S. Leonhardt introduced an anatomical model of the heart, lungs, and pulmonary arteries. To simplify the model, a single heart ventricle is represented by two concentric ellipsoids, while each lung is modeled using one hemi-ellipsoid. An ellipsoidal cylinder models the thorax. Around the half-height of the thorax cross-section, 16 equidistantly placed electrodes are simulated [40].

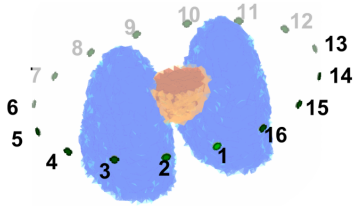

Figure 3.5: Visual representation of the anatomical model [40].

According to the authors, the pulmonary tree is built from small, medium, and large vessels. Therefore, the following equation utilizes a scaled and offseted template function $T_i(\phi)$ for each vessel caliber $i = \{\text{small, medium, large}\}$ to model the volume changes with quasiperiodic volume functions as

$$V_i(t) = V_{max,i} - \left(\frac{\Delta V_i(t)}{2} \cdot T_i(\phi) + \frac{\Delta V_i(t)}{2} \right), \tag{3.16}$$

where V_i is the volume of the respective organ over time t oscillating with ΔV_i below a maximum value $V_{max,i}$, according to a template function $T_i \in [-1, 1]$ with $\phi = \phi(t)$ as its cycle phase [40].

As further explained in [40], the synthesizer is equipped with the cardiorespiratory frequency coupling, initially presented in [34], to simulate the signal's non-stationarity due to the so-called respiratory sinus arrhythmia and Mayer wave oscillations. That way, the heart-lung interactions are simulated through differential equations with two user-defined frequency coupling parameters. These parameters' values are designed for synthesizing physiologically relevant EIT signals comparable to those measured in adults.

According to [40], the conductivities of muscles, fat, bones, and blood in the ventricle are set constant. The conductivities of lung tissue and blood in the lungs are defined as functions of local organ movement and arterial flow.

The vessel distribution in the pulmonary tree is given by the custom radial density functions amorphously distributed throughout the lungs. The amorphous distribution leads to lower computational costs while not significantly lowering the model's overall accuracy because of EIT's spatial resolution limitations [40].

As further explained in [40], the blood volume in an element of the FEM mesh is empirically defined as a weighted sum of the contributions from all vessel calibers. The following equation, initially presented by Klaas R. Visser in [51], models flow-dependent intravascular blood conductivity changes

$$\Delta\sigma_{perf}(\epsilon,t) = -0.45 \cdot HCT \cdot \left(1 - e^{-0.26\left(\frac{v(\epsilon,t)}{r(\epsilon,t)}\right)^{0.39}}\right), \tag{3.17}$$

where $\Delta\sigma_{perf}(\epsilon,t)$ is the change in blood conductivity in element ϵ at time t, considering cylindrical vessels with changing radius $r(\epsilon,t)$, as defined with equation 3.16, and $v(\epsilon,t)$ is the mean velocity of blood with hematocrit value $HCT = 43$ % passing through the vessels [40].

According to [40], the lung tissue conductivity in an element $\sigma_{vent}(\epsilon,t)$ is assumed to oscillate between deflated ($\sigma = 0.270$ S/m) and inflated ($\sigma = 0.110$ S/m) states synchronously to the volume changes $V_{vent}(\epsilon,t)$. The volume changes are considered to be homogeneously distributed over all lung mesh elements. Moreover, time delay t_0 is applied to the conductivity, volume, and flow curves of lung elements at a distance d from the pulmonary valve using $t_0 = \frac{d}{\mathrm{PWV}}$, with pulse wave velocity (PWV) set as 200 cm/s [40].

Finally, the mixed conductivity of element ϵ at time t is obtained from the Maxwell Garnett mixing formula, initially presented in [39] and utilized also in [38], expressed as

$$\sigma(\epsilon,t) = \sigma_{vent}(\epsilon,t) + \frac{\frac{1}{3} \cdot f_v(\epsilon,t) \cdot [\sigma_{perf}(\epsilon,t) - \sigma_{vent}(\epsilon,t)] \cdot a(\epsilon,t)}{1 - \frac{1}{3} \cdot f_v(\epsilon,t) \cdot [\sigma_{perf}(\epsilon,t) - \sigma_{vent}(\epsilon,t)] \cdot b(\epsilon,t)}, \tag{3.18}$$

where $a(\epsilon,t)$, $b(\epsilon,t)$ are substitutions to make the equation simpler to understand, and $f_v(\epsilon,t)$ is a local volume fraction in element ϵ over time t. Furthermore, a dielectric background of lung tissue $\sigma_{vent}(\epsilon,t)$ is assumed to contain cylindrical perfusion inclusions, encoded by $\mathbf{M} = (0.5,\ 0.5,\ 0)$ [40].

$$a(\epsilon,t) = \sum_{i=1}^{3} \frac{\sigma_{vent}(\epsilon,t)}{\sigma_{vent}(\epsilon,t) + M_i \cdot [\sigma_{perf}(\epsilon,t) - \sigma_{vent}(\epsilon,t)]}, \tag{3.19}$$

$$b(\epsilon,t) = \sum_{i=1}^{3} \frac{M_i}{\sigma_{vent}(\epsilon,t) + M_i \cdot [\sigma_{perf}(\epsilon,t) - \sigma_{vent}(\epsilon,t)]}, \tag{3.20}$$

$$f_v(\epsilon,t) = \frac{V_{perf}(\epsilon,t)}{V_{perf}(\epsilon,t) + V_{vent}(\epsilon,t)}. \tag{3.21}$$

As presented in [40], a mixed EIT signal, VRS, and CRS can be generated using the proposed synthesizer. To obtain a VRS or CRS, $\sigma(\epsilon,t)$ is simply set as $\sigma_{vent}(\epsilon,t)$ or $\sigma_{perf}(\epsilon,t)$, respectively. Therefore, the model can produce realistic non-stationary EIT signals while preserving all physiological characteristics relevant to source separation.

Initially, all the necessary model parameters and template functions were set accordingly to various publications, e.g., [38], [52] while subject to further optimization. However, as

utilized in this work, the synthesizer configuration does not include spontaneous ventilation modeling, which is still in development. Therefore, only mechanical ventilation is simulated.

Furthermore, the provided implementation allows for various physiological parameter settings. It also accepts definitions of different vessels' spatial densities and enables the employment of user-defined templates for volume and flow equations. This allows for the simulations of, for example, various ventilation or perfusion injuries [40].

3.3.2 Input values for the synthesizer

To synthesize the validation signal, it is first necessary to set the respective parameters of the EIT synthesizer. It is decided to synthesize three validation signals (mixed, VRS, and CRS) with only one setting of parameter values that would simulate all possible situations at the bedside. This can be achieved with the following parameters: a set of RR values f_{RR} [bpm] and HR values f_{HR} [bpm], the time duration of the synthesized signal t_{sim} [s], and the sampling frequency f_s [Hz] which corresponds to EIT video frame rate in fps.

It is to be noted that the model interpolates the f_{RR} and f_{HR} values to smoothen any sudden transitions. During the interpolation, the given values are considered equally distributed in time. That way, a valid EIT signal is always synthesized based on various input RR and HR. Moreover, the true RR and HR values after the interpolation are known and can be analyzed and compared to, e.g., multi-pitch estimation results.

To simulate as many potential situations as possible, the values of f_{RR} and f_{HR} are designed to contain three plateaus (very low, very high, and a medium one) and some fast and slow changes. Since the f_s is given as 50 Hz, the t_{sim} is set to 120 s to provide a good compromise between computational costs and valid RR and HR changes. The following table shows the exact input values of f_{RR} and f_{HR}.

	set of values [bpm]
f_{RR}	{13, 12, 18, 23, 45, 46, 33, 30, 27, 25, 24}
f_{HR}	{50, 50, 70, 90, 180, 180, 130, 120, 110, 100, 100}

Table 3.2: The input values of f_{RR} and f_{HR} for the EIT synthesizer.

As shown in Table 3.2, a sort of resting state is simulated in the first ca. 13 seconds of the signal with a very low plateau. For this purpose, the RR and HR are set close to 12 bpm and 50 bpm, respectively. By the following slow rise to approx. 20 and 80 bpm, somewhat increased activity is simulated. Next, with a steep increase to the high plateau at approx. 45 and 180 bpm followed by an abrupt decrease to approx. 30 and 130 bpm, a more challenging signal for multi-pitch estimation and source separation is created. Finally,

the last slow decline and a medium plateau simulate a sort of resting activity after, for example, a challenging physical exercise.

The input values of RR and HR are chosen based on the author's knowledge and study of literature on typical RR and HR values in adults, e.g., [53], [54], and [55]. Also, the values are designed so that the ratio of HR to RR, commonly known as pulse-respiration quotient (PRQ), stays close to 4 [56, 57]. Based on these studies, PRQ seems relatively stable regardless of whether there is a resting state or a physical exercise.

Figure 3.6 shows the true RR and HR values after the interpolation. Those are the exact values used for validation signal synthesis. Therefore, they are considered the ground truth frequencies and compared to multi-pitch estimation results in section 4.1.

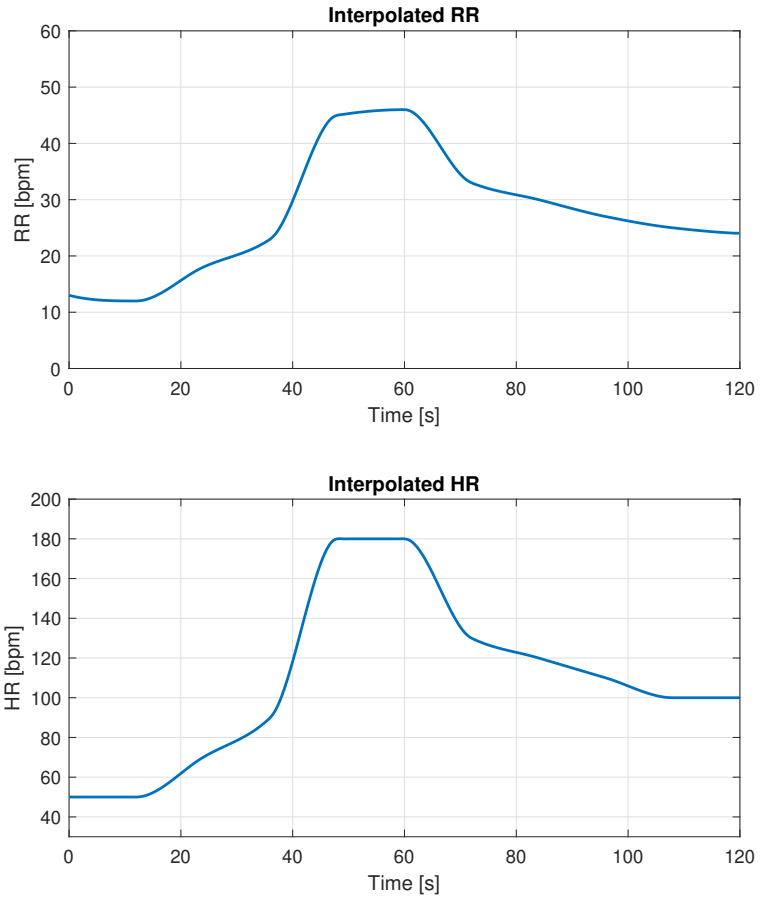

Figure 3.6: The true values of RR and HR after the interpolation.

It is to be pointed out that such fast and significant changes in RR and HR would most likely not be observed in adults at the bedside since there is no challenging physical exercise. However, in neonates, the resting RR and HR are usually much higher (approx. 30-50 and

120 - 150 bpm, respectively), and the changes are faster and more significant than in adults [58, 59].

Moreover, the synthesized validation signal should serve as a set of many possible real-life situations stacked one by one instead of replicating a signal measured continuously in one subject. Moreover, it should be as general as possible since when the proposed algorithms can follow changes with overestimated speed and magnitude, they can easily follow the true ones. Ultimately, such values can provide a perfect understanding of the algorithms' performance in real-life situations.

3.3.3 Synthesized EIT signals

Finally, the validation signals are synthesized. In Figure 3.7, all three types of the generated signals are shown in the time domain. Although the signals are synthesized for all pixels in a 64x64 image, only a signal in a typical lung pixel with coordinates $(x, y) = (49, 30)$ is selected for the visualization. Moreover, only the first 60 seconds of the synthesized signals are shown for clarity.

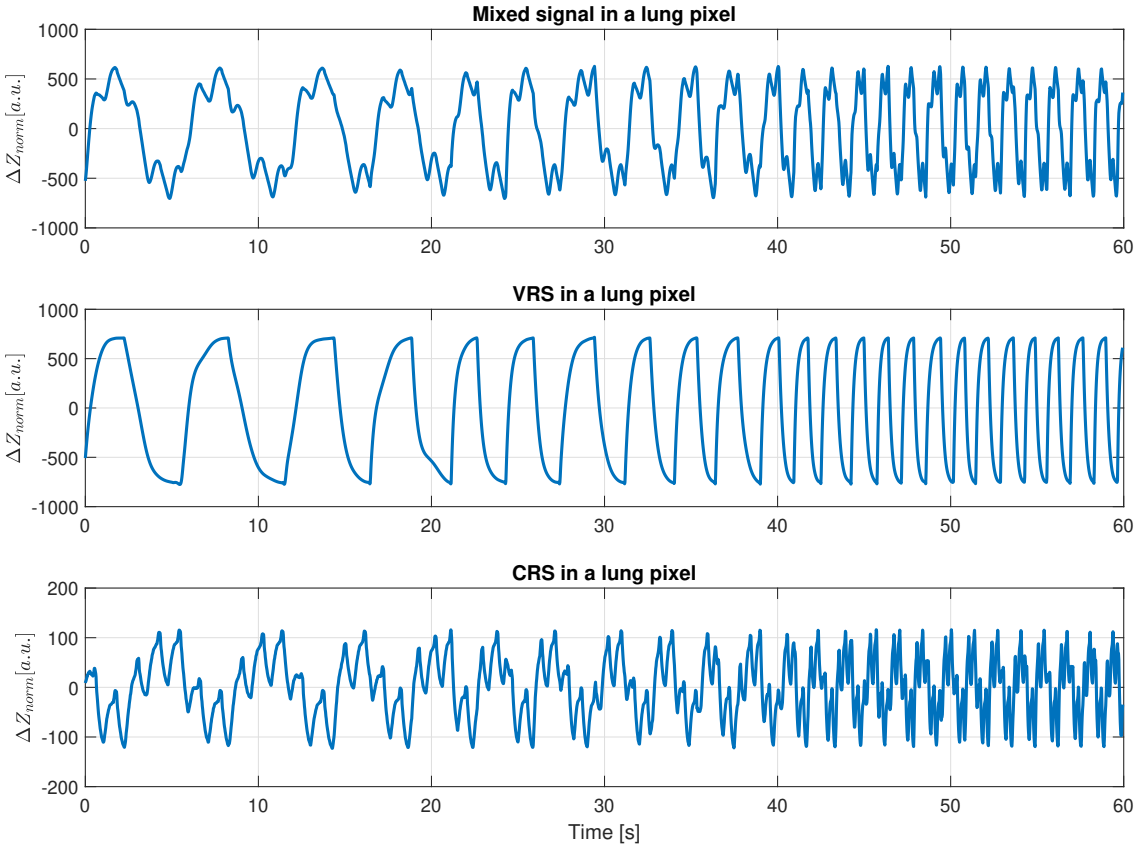

Figure 3.7: First 60 seconds of the synthesized signals in a lung pixel in the time domain.

At first sight, the influence of changing RR and HR can be seen. Also, the mixed EIT signal has the usual EIT signal properties, i.e., fast oscillations caused by cardiac activity are superimposed on the slow ones caused by ventilation. Compared to the example of a global EIT signal shown in Figure 2.6, the synthesized signal looks slightly different, probably because the synthesizer does not model spontaneous ventilation.

The effect of the mechanical ventilation simulation is observable in VRS since the shape of its waveform looks quite similar to the typical volume curves observed in patients during ventilator therapy [60, 61]. Moreover, the VRS amplitude is approximately five times higher than the CRS.

It might be surprising that the CRS waveform contains some low-frequency oscillations. This happens because the CRS in the lungs corresponds to the perfusion of lung tissue and, therefore, is influenced not only by cardiac activity but also by lung movements during ventilation. To prove that the synthesized CRS is valid, Figure 3.8 shows all three signals in a typical cardiac-dominated heart pixel with coordinates $(x, y) = (43, 16)$ found with the pixel detection algorithm.

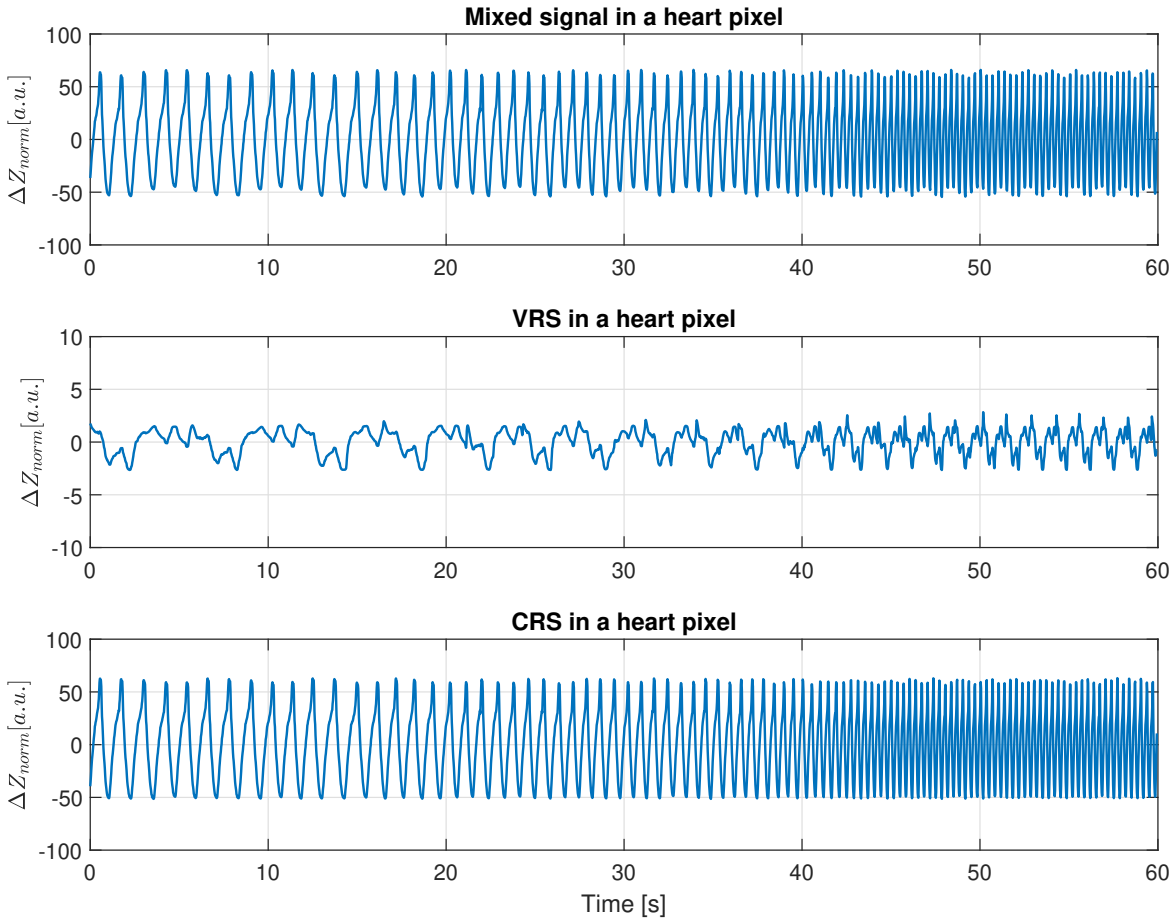

Figure 3.8: First 60 seconds of the synthesized signals in a heart pixel in the time domain.

As shown in Figure 3.8, the mixed signal and VRS in a heart pixel look very different than in a lung pixel, and no slow oscillations can be observed in the CRS. Moreover, the mixed signal is composed almost exclusively of the CRS since the amplitude of the VRS is extremely small. This can be expected since the EIT signal in the heart is influenced almost solely by cardiac activity.

To prove that the synthesized signals also have valid physiological properties in the frequency domain, they are converted from the time domain using FFT and shown in Figure 3.9. The mixed signal and VRS in a lung pixel are displayed, whereas the CRS in a heart pixel is shown. For clarity, only the first 20 seconds of each signal, with low and steady frequencies, are shown.

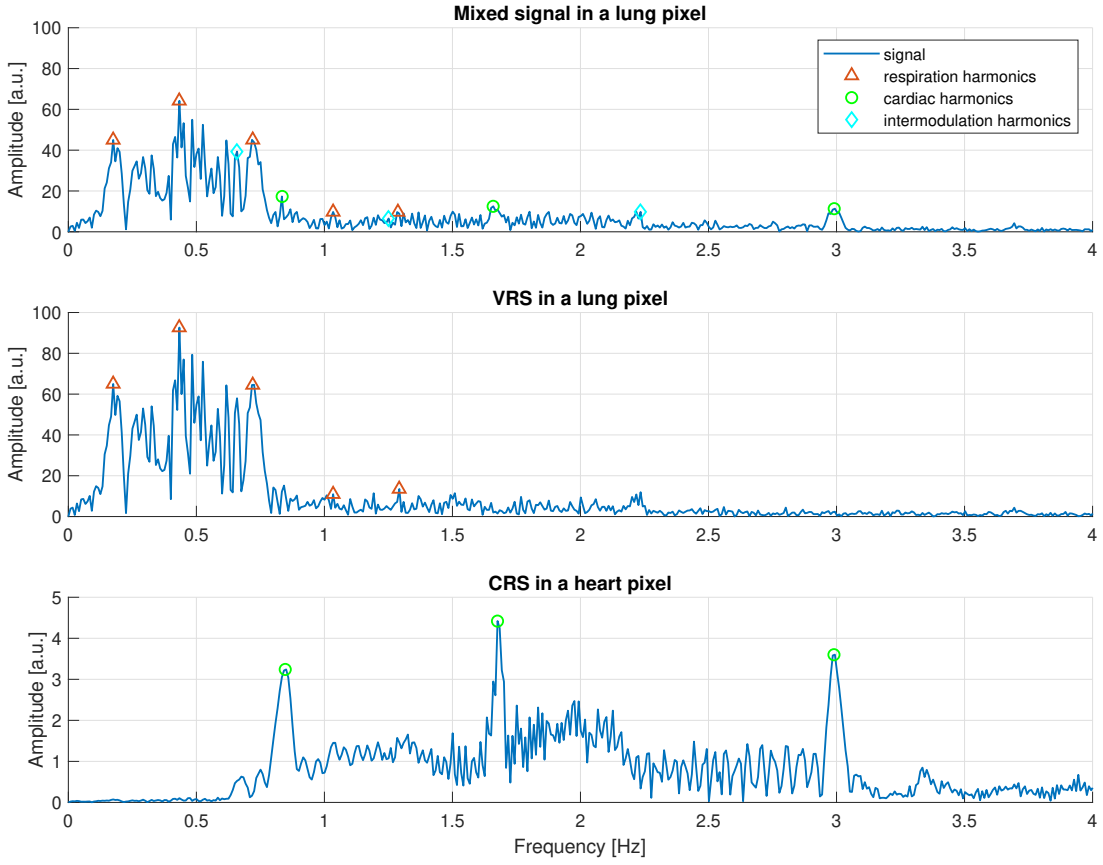

Figure 3.9: First 20 seconds of the synthesized EIT signals in the frequency domain

It is to be pointed out that the first cardiac and intermodulation harmonics almost overlap with the third ventilation harmonic, and the second intermodulation harmonic almost overlaps with the fifth ventilation harmonic. This also happens sometimes in real EIT signals measured in patients.

Eventually, the synthesized validation signals are considered realistic enough to be used for the validation and comparison of the implemented multi-pitch and source separation algorithms presented in the following chapter.

3.4 Performance assessment metrics

Standard estimation accuracy metrics, namely the RMSE and bias, are used to measure the accuracy of all the implemented algorithms. To better assess the overall algorithms' performance, time domain, and, in the case of the multi-pitch estimation algorithms, Bland-Altman plots are analyzed. Moreover, the time needed to process one input signal sample is measured.

Eventually, the RMSE, bias, and LoA are combined into the so-called multi-pitch estimation quality index (MEQI) for parameter optimization of the grid search and CLIE algorithms. To adapt this approach for source separation, source separation quality index (SSQI) is developed by combining the RMSE, bias, and Pearson correlation coefficient.

3.4.1 RMSE and bias

For the accuracy assessment of the implemented multi-pitch estimation algorithms, RMSE is defined as

$$\mathrm{RMSE}_i = \sqrt{\frac{1}{N} \cdot \sum_{n=1}^{N} (\hat{\mathbf{f}}_{0,i}[n] - \mathbf{f}_{0,i}[n])^2}, \tag{3.22}$$

where $i = \{RR, HR\}$ denotes the estimated frequency, N is the number of estimates, $\mathbf{f}_{0,i}$ is the vector of true frequencies, and $\hat{\mathbf{f}}_{0,i}$ is the vector of the estimated frequencies.

Bias (offset, mean error) is then given as

$$\mathrm{bias}_i = \frac{1}{N} \cdot \sum_{n=1}^{N} (\hat{\mathbf{f}}_{0,i}[n] - \mathbf{f}_{0,i}[n]). \tag{3.23}$$

It is to be noted that the RMSE and bias are defined analogously for the accuracy assessment of the implemented source separation algorithms since instead of the RR and HR, the normalized impedance changes ΔZ_{norm} are estimated.

3.4.2 Bland–Altman plot

Being well-known in analytical chemistry or biomedicine, the so-called Bland–Altman plot or, in other words, difference plot, is a valuable tool for analyzing the estimation accuracy, aside from RMSE and bias. In our case, the vertical axis of a Bland-Altman plot shows the estimation errors defined as

$$E_i = \hat{\mathbf{f}}_{0,i}[n] - \mathbf{f}_{0,i}[n], \tag{3.24}$$

where $n \in [1, ..., N]$ while the horizontal axis is defined by the average frequency values

$$\overline{\mathbf{f}}_{0,i} = \frac{1}{2}(\hat{\mathbf{f}}_{0,i} + \mathbf{f}_{0,i}). \tag{3.25}$$

Moreover, in a Bland-Altman plot, two horizontal lines at $bias_i \pm LoA_i$ are displayed. LoA are defined as

$$\mathrm{LoA}_i = 1.96 \cdot \sigma_{E_i}, \tag{3.26}$$

where σ_{E_i} is the standard deviation of the estimation error. Therefore, a Bland-Altman plot provides a complex overview of the estimation errors. Any trends or outliers can be immediately seen in relation to the average frequencies, and different biases and LoA can be easily compared.

3.4.3 Computation time

When considering a potential real-time application, the complete algorithm's computation time needed for one input signal sample must be lower than the EIT sampling period $T_s = \frac{1}{f_s} = \frac{1}{50\ \mathrm{Hz}} = 20$ ms.

Therefore, the computation time is measured using MATLAB stopwatch functions *tic* and *toc*. However, since they cannot reliably measure multiple subsequent time intervals shorter than 100 ms, the total computation time T_C is measured and divided by the number of estimations N to find the average time needed to obtain one estimate of RR and HR

$$\overline{T}_{est} = \frac{T_C}{N}. \tag{3.27}$$

The measurement is performed in Matlab R2021b installed on a Dell Inspiron 15 5505 laptop equipped with AMD Ryzen 7 4700U 2.00 GHz processor with integrated Radeon graphics and 16 GB of RAM. The operating system is 64-bit Windows 11 Pro 22H2.

3.4.4 MEQI

For parameter optimization of the multi-pitch estimation algorithms, the MEQI is developed to provide one simple-to-understand measure of estimation accuracy. To obtain the MEQI, the RMSE, bias, and LoA values obtained with different parameter settings are first normalized in the range from zero to one. Next, the average of all the values is found. Finally, for better interpretability, the MEQI is subtracted from 1

$$\mathrm{MEQI} = 1 - \frac{1}{M}\sum_{i=1}^{2}(\mathrm{RMSE}_i + \mathrm{bias}_i + \mathrm{LoA}_i), \tag{3.28}$$

where $M = 6$ is the total number of the summed values and $i = \{1, 2\} \mathrel{\hat{=}} \{RR, HR\}$ denotes the type of estimated frequency. This way, the MEQI values are also defined in the range [0,1], which is very convenient and simple to understand.

3.4.5 SSQI

The RMSE, bias, and Pearson correlation coefficient are combined to measure the accuracy of the source separation algorithms. Pearson correlation coefficient ρ is calculated using MATLAB in-built function *corrcoef* which, according to the documentation [62], defines the coefficient as

$$\rho(A, B) = \frac{1}{N-1}\sum_{i=1}^{N}\left(\frac{A_i - \mu_A}{\sigma_A}\right)\left(\frac{B_i - \mu_B}{\sigma_B}\right) = \frac{cov(A, B)}{\sigma_A \sigma_B}, \tag{3.29}$$

where μ_A, μ_B are the means and σ_A, σ_B are the standard deviations of A and B, respectively. In our case, A and B are set as $\hat{\mathbf{y}}$ and $\mathbf{y}$.

The SSQI is given as

$$\mathrm{SSQI} = \left(\frac{\mathrm{RMSE}_{VRS} + \mathrm{RMSE}_{CRS}}{2}\right) \cdot \left(\frac{|\mathrm{bias}_{VRS}| + |\mathrm{bias}_{CRS}|}{2}\right) \cdot \left(\frac{2}{\rho_{VRS} + \rho_{CRS}}\right). \tag{3.30}$$

Since the RMSE, bias, and Pearson correlation coefficient can have significantly different values and the SSQI values are not in the range from zero to one, this is not as convenient measure as MEQI. Moreover, unlike the MEQI, lower SSQI is better. However, the SSQI provides one simple-to-calculate value for each version of the complete source separation algorithm, thus making a direct comparison easier.

4 Results and discussion

This chapter provides the results of the validation and comparison of the implemented algorithms. First, the multi-pitch estimation algorithms are validated, and their versions are compared. Next, the best-performing versions of the grid search and CLIE algorithms are subjected to parameter optimization. In the end, the optimized grid search and CLIE algorithms are combined with the comb filtering algorithm, and the complete algorithmic ensemble is used for source separation in the synthesized validation EIT signal.

4.1 Multi-pitch estimation algorithms

The implemented versions of the grid search and CLIE algorithms are validated and compared in the following sections using the synthesized validation signals, already described in section 3.3.3. Four implemented versions of the grid search algorithm and two versions of the CLIE algorithm, described in sections 3.2.2 and 3.2.3, are validated and compared based on the multi-pitch estimation metrics presented in the previous section.

4.1.1 Grid search algorithm

For grid search validation, a balanced EIT signal with the component representation ratio $R = 1$ in the pixel with coordinates $(x, y) = (53{,}25)$, found with the pixel detection algorithm (see 3.2.1), is used. Figure 4.1 shows its first 60 seconds in the time domain.

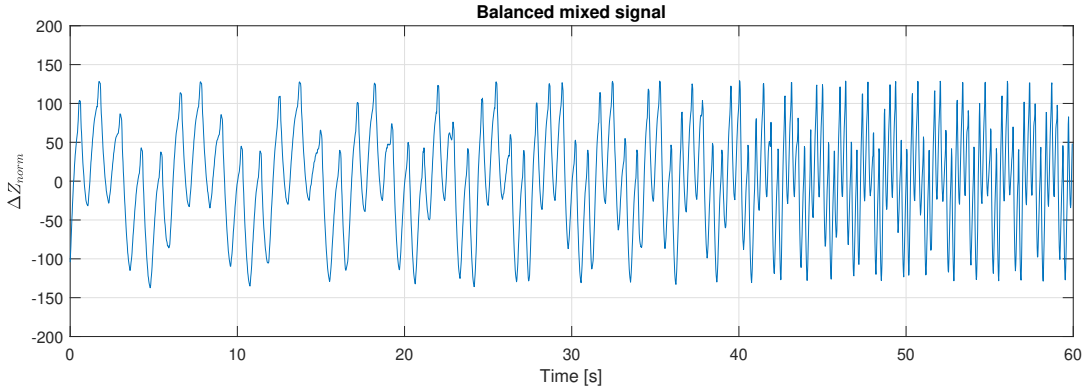

Figure 4.1: First 60 seconds of a balanced EIT signal used for grid search validation.

For clarity, time plots and Bland-Altman plots obtained with each implemented algorithm version are first shown. Consequently, a comparison table with all performance metrics is provided, and the best-performing algorithm version is selected.

Original implementation

No serious modifications are present in the original implementation of the grid search algorithm. Only slight improvements of the parameter values presented in [32] are found empirically, e.g., the processing window length $W = 180$ samples (3,6 s) and the Laplacian prior scale parameters $b_{RR} = 0.5$, $b_{HR} = 3.5$. The number of previous estimations used for Laplace prior calculation $n = 10$ was already presented in [36] and [32]. The following figure shows the respective time-domain and Bland-Altman plots.

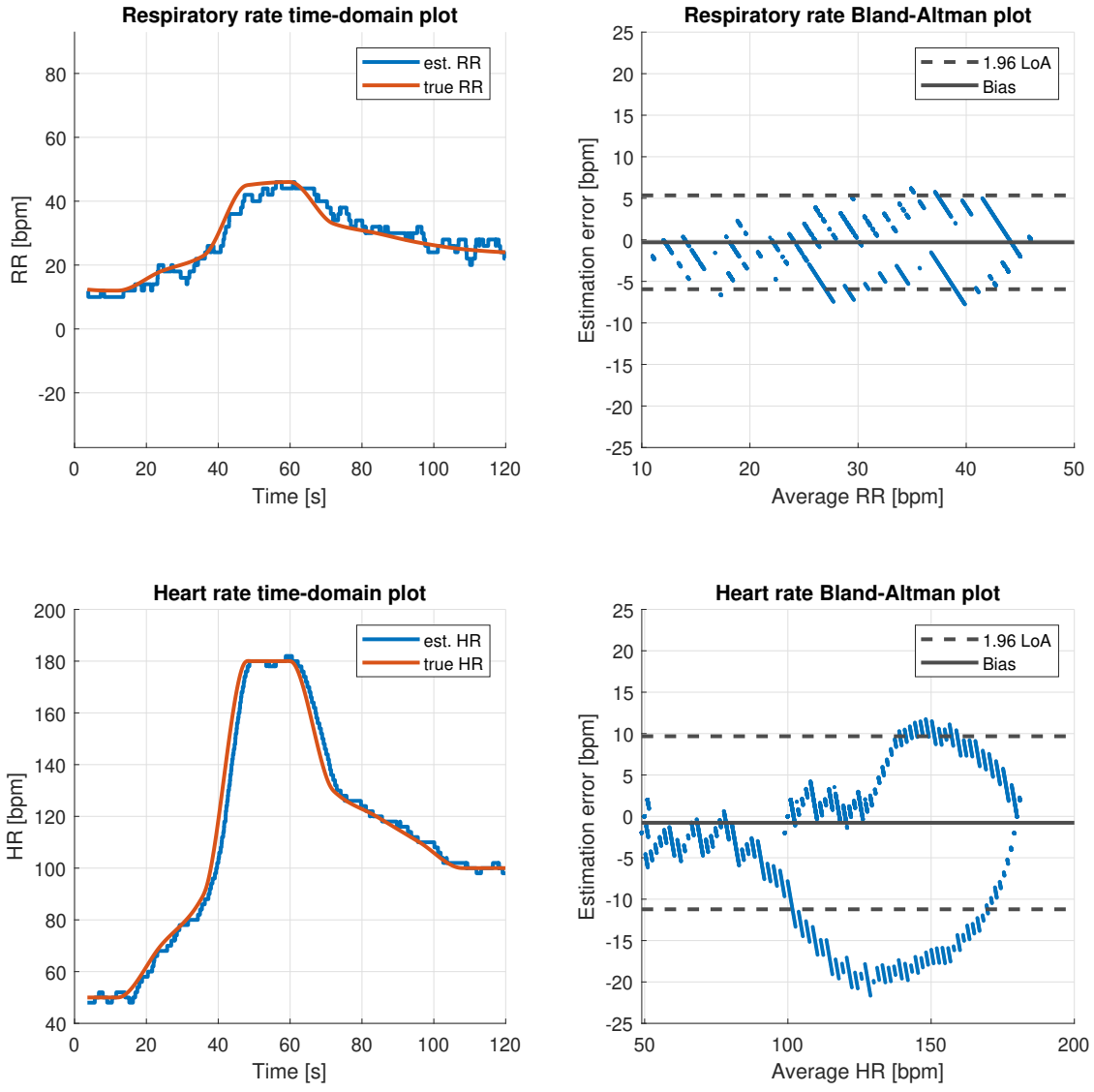

Figure 4.2: Grid search version 1 - time-domain and Bland-Altman plots.

Laplace prior thresholding

The second version of the grid search algorithm includes the Laplace prior thresholding described in section 3.2.2. The parameter p defined by equation 3.5 is initially set as 0.75. No other parameters of the algorithm are changed. Thus, the respective time-domain and Bland-Altman plots, shown in the following figure, are the same as those shown in Figure 4.2.

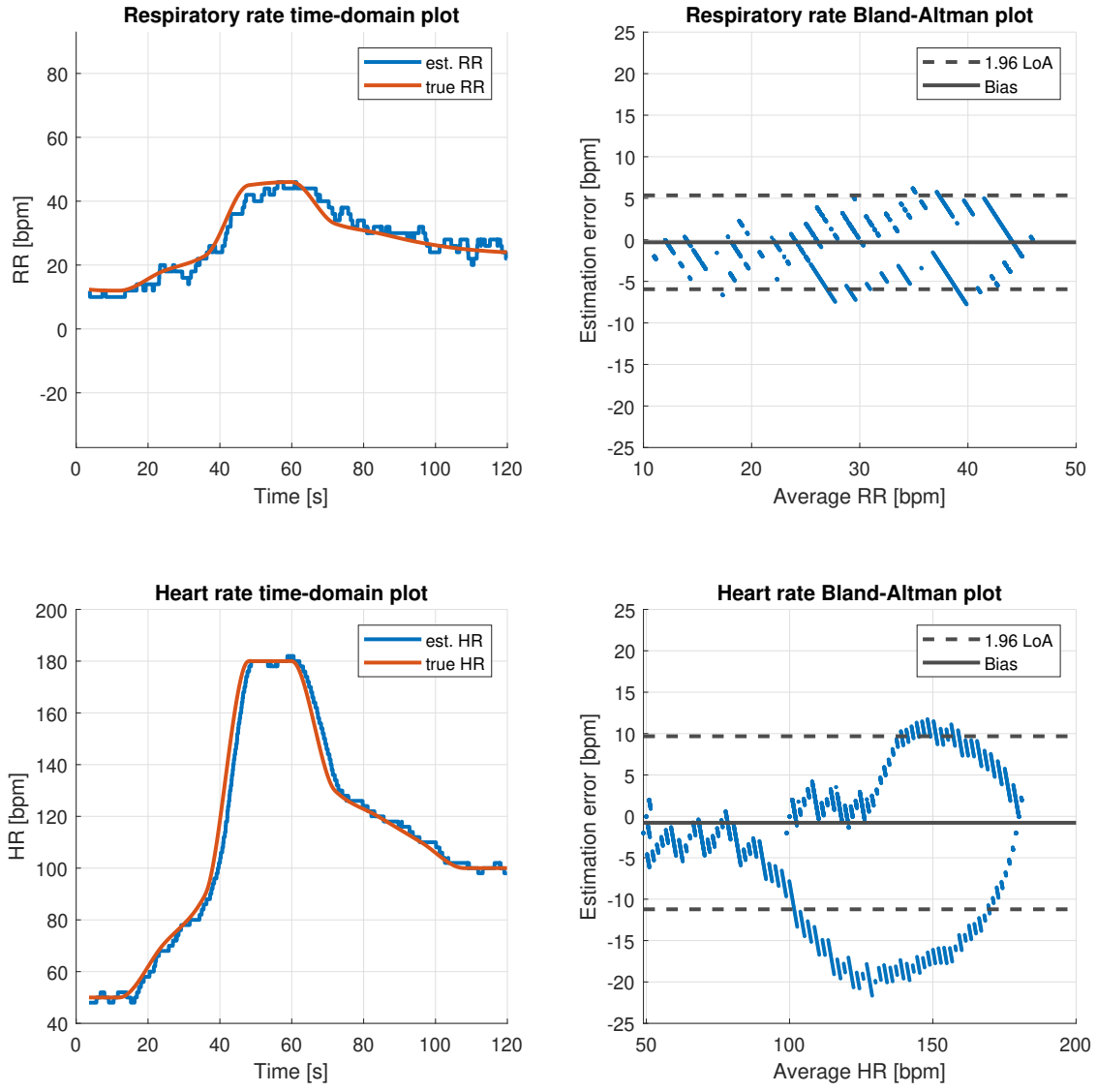

Figure 4.3: Grid search version 2 - time-domain and Bland-Altman plots.

Adaptive parameters

Adaptive parameters are implemented in the third version of the grid search algorithm, allowing it to follow fast RR and HR changes better. As explained in 3.2.2, the $W = 750$ samples is set to always include at least two respiration cycles while the cropping window of the adaptive size is introduced. Moreover, the adaptive n is introduced according to equation 3.8 with the initial value of r set initially as 0.15. The following figure shows the respective time-domain and Bland-Altman plots.

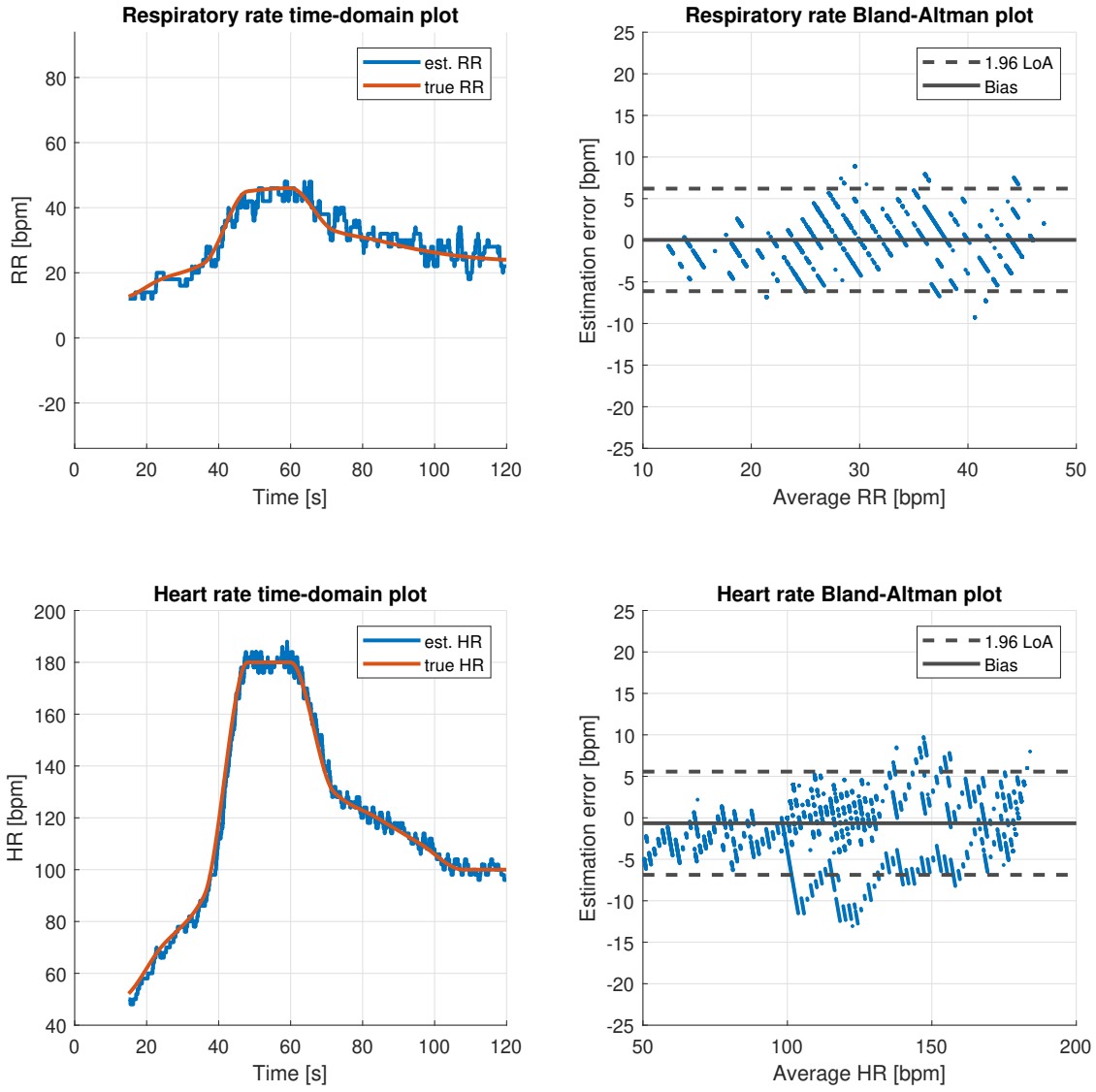

Figure 4.4: Grid search version 3 - time-domain and Bland-Altman plots.

Super-resolution

In the fourth implemented version, the super-resolution, described in section 3.2.2, is introduced. The following figure shows the respective time-domain and Bland-Altman plots.

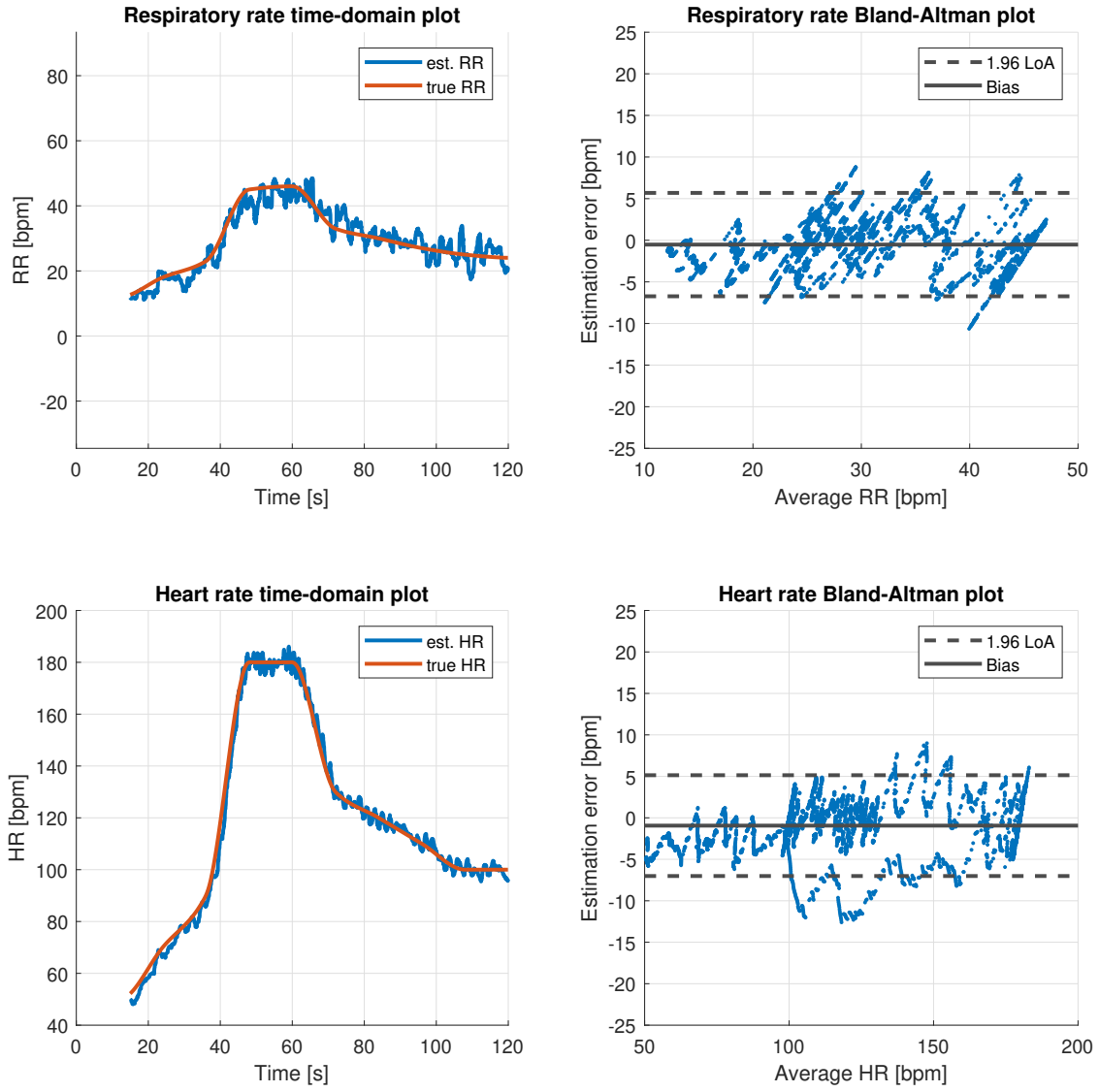

Figure 4.5: Grid search version 4 - time-domain and Bland-Altman plots.

Best-performing version selection

The following table with all the obtained values of the performance metrics is provided to explain the selection of the best-performing version of the grid search algorithm. All the obtained values of the performance metrics and the measured computation times are compared. Moreover, the time-domain and Bland-Altman plots are analyzed.

Version	1	2	3	4
RMSE_{RR} [bpm]	**2.90**	**2.90**	3.14	3.21
RMSE_{HR} [bpm]	5.39	5.39	**3.24**	**3.24**
bias_{RR} [bpm]	-0.30	-0.30	**0.04**	-0.52
bias_{HR} [bpm]	-0.77	-0.77	**-0.65**	-0.94
LoA_{RR} [bpm]	**5.65**	**5.65**	6.16	6.21
LoA_{HR} [bpm]	10.45	10.45	6.22	**6.08**
TC [s]	177.86	38.92	**37.49**	39.89
$\overline{T}_{est}$ [ms]	30.58	**6.69**	7.15	7.60

Table 4.1: Performance metrics obtained with each version of the grid search algorithm.

When analyzing Table 4.1 and Figures 4.2, 4.4, and 4.5, it can be seen that the accuracy and robustness of the HR estimation is improved when the adaptive parameters are introduced in version 3. Although the accuracy in RR estimation is slightly lower than with the original implementation, the difference is negligible.

For a potential real-time application, it is essential that the average time needed to obtain one estimation $\overline{T}_{est}$ is significantly lowered when the Laplace prior thresholding is introduced in version 2. Another improvement is achieved when the adaptive parameters are first implemented in version 3 and, consequently, in version 4.

The super-resolution, implemented in version 4, does not seem to provide any improvements neither on the accuracy nor robustness of the estimation. Therefore, version 3 of the grid search algorithm, which includes the Laplace prior thresholding and adaptive parameters, is selected for the parameter optimization described in section 4.2.1.

4.1.2 Iterative CLIE algorithm

For the validation of the implemented CLIE algorithms, different EIT signals are used. Similarly to the grid search algorithm validation, respective time plots and Bland-Altman plots obtained using each implemented algorithm version are first shown. Next, a comparison table with all performance metrics is provided, and the best-performing algorithm version is selected.

LP and HP filtering

As explained in section 3.2.3, the first version of the iterative CLIE algorithm, based on the LP and HP filtering, is designed to work with two different input signals, ventilation-dominated and cardiac-dominated. Therefore, the mixed signals from typical lung and heart pixels, already shown in Figures 3.7 and 3.8, are used. The following figure shows the respective time-domain and Bland-Altman plots.

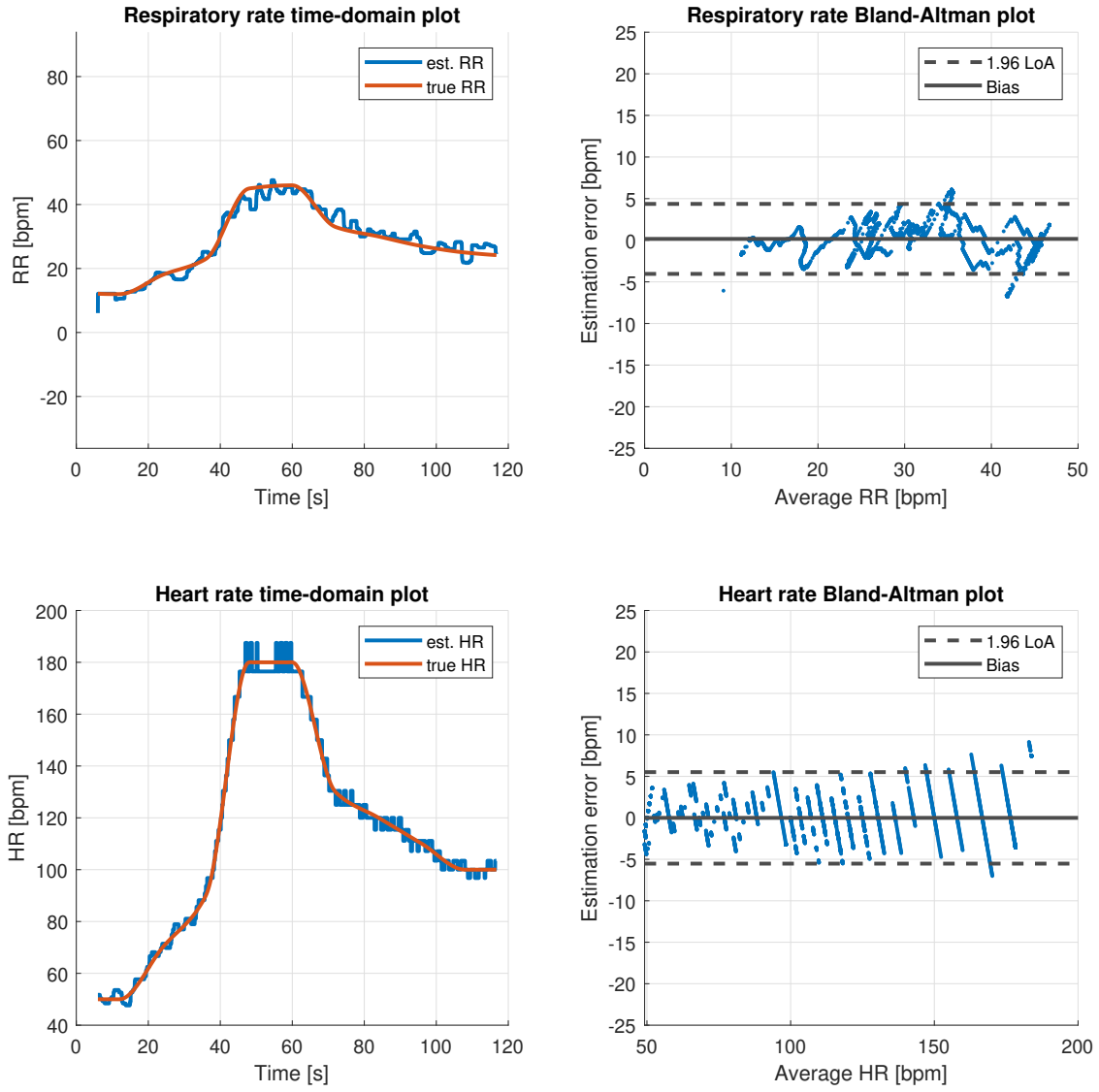

Figure 4.6: CLIE version 1 - time-domain and Bland-Altman plots.

LP and comb filtering

Based on the LP and comb filtering, the second implemented version of the iterative CLIE algorithm needs only one input signal (see 3.2.3). Therefore, the same balanced signal as for the grid search algorithm validation, shown in Figure 4.1, is utilized.

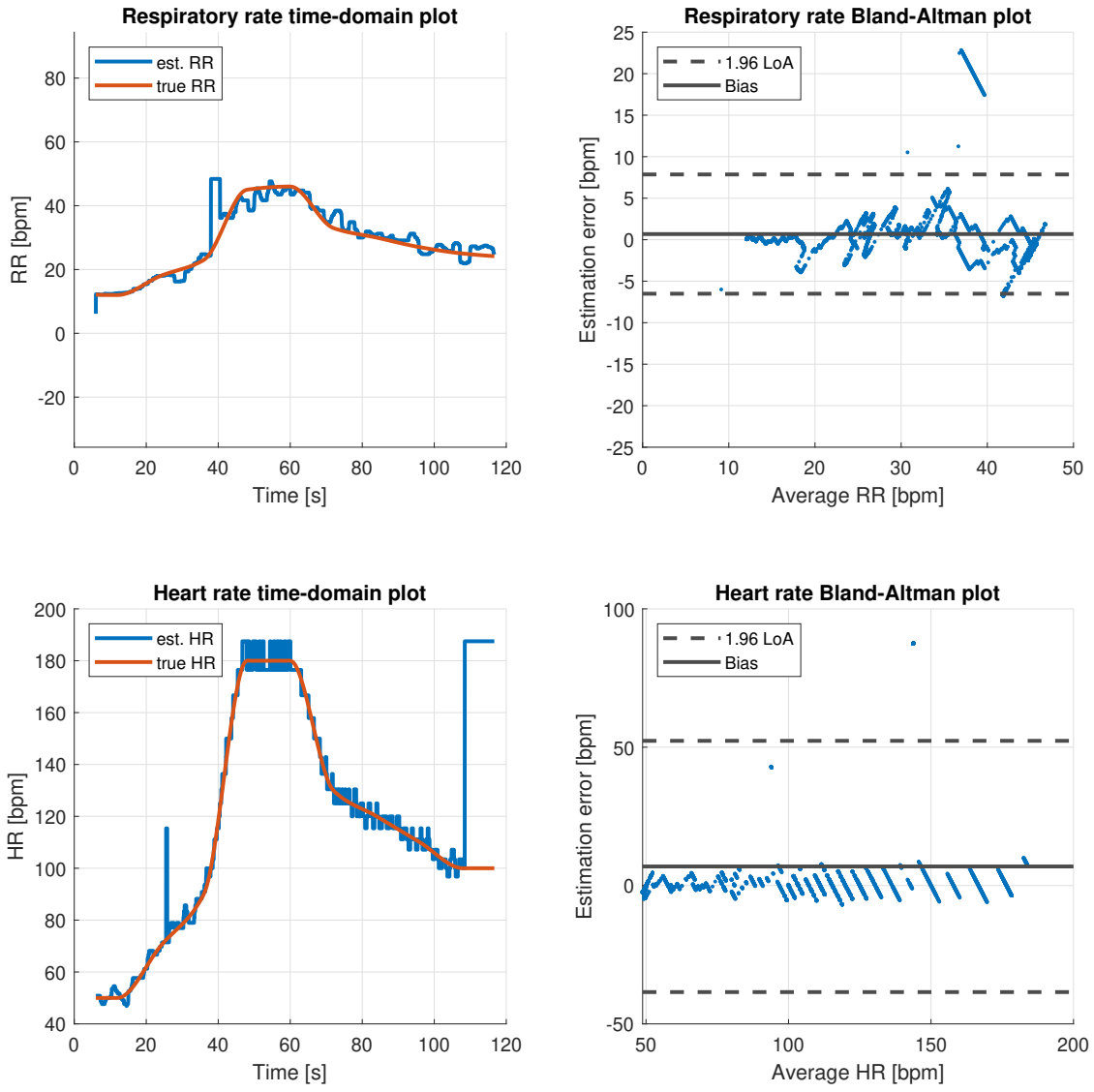

Figure 4.7: CLIE version 2 - time-domain and Bland-Altman plots.

Best-performing version selection

Version	1	2
RMSE_{RR} [bpm]	**2.15**	3.73
RMSE_{HR} [bpm]	**2.81**	24.17
bias_{RR} [bpm]	**0.16**	0.68
bias_{HR} [bpm]	**-0.01**	6.89
LoA_{RR} [bpm]	**4.20**	7.19
LoA_{HR} [bpm]	**5.52**	45.41
TC [ms]	**530.56**	560.77
$\overline{T}_{est}$ [ms]	**0.10**	**0.10**

Table 4.2: Performance metrics values obtained with each CLIE algorithm version.

When analyzing Table 4.2 and Figures 4.6 and 4.7, it can be seen that the robustness of the RR and HR estimation is much better with the first CLIE algorithm version.

On the one hand, the comb filter implemented in version 2 produces some outliers and generally makes the iterative CLIE implementation more complex. On the other hand, it demonstrates that only one signal can be used when performing multi-pitch estimation using the modified CLIE algorithm. With additional parameter optimization, the outliers could be removed to make the estimation almost as with the first version.

However, the simpler and more effective version 1, providing a more robust estimation, is selected for parameter optimization, described in section 4.2.2.

4.2 Parameter optimization

The accuracy of the open-loop source separation algorithms highly depends on the accuracy of the multi-pitch estimation algorithms. Therefore, the best-performing versions of the grid search (version 3) and CLIE (version 1) algorithms are subjected to parameter optimization to improve their performance further. For this purpose, the same input signals as for the validation of each algorithm's versions are used.

Similarly to the validation of the algorithms' versions, the parameter optimization of the grid search algorithm is described first, followed by the parameter optimization of the iterative CLIE. Since all the parameters are described in detail in chapter 3, only a simple list with references follows.

parameter	reference	algorithm type
r	equation 3.8	grid search
b	equation 3.2	grid search
p	equation 3.5	grid search
s	paragraph containing equation 3.13	CLIE
M	second paragraph below equation 3.13	CLIE

Table 4.3: List of optimized parameters of the multi-pitch estimation algorithms.

During the optimization, the RR and HR estimation is performed repeatedly with each algorithm using a pre-defined set of parameter values. These sets are swept over using a for-loop (grid search-inspired optimization). The optimum value is then found by maximizing the MEQI described in section 3.4.4.

Moreover, the respective $\overline{T}_{est}$ values are compared to confirm that the selected parameter does not significantly increase the algorithm's computation time. To keep this section concise, all the obtained MEQI and computation time figures are shown in appendices A.1 and A.2.

Finally, when the optimal parameter value is found, the respective time-domain and Bland-Altman plots are analyzed to confirm the selection. The verified parameter value is then set permanently so the remaining parameters are optimized using the current best-available algorithm setting.

4.2.1 Grid search algorithm

First, the r parameter of the grid search algorithm is optimized with the set of values $\{0.05, 0.10, ..., 1.00\}$. To optimize the **b** parameter, a 2-column matrix of all the possible combinations of b_{RR} and b_{HR} is defined. The optimization is performed multiple times to find the optimal range with a coarse set of values and then to search this range with a much finer set to find the optimal values as accurately as possible. Finally, the highest value of p resulting in no loss in the algorithm's performance is identified in the set of values $\{0.40, 0.45, ..., 1.00\}$.

Figure 4.8 shows the time-domain and Bland-Altman plots obtained with the optimized grid search algorithm.

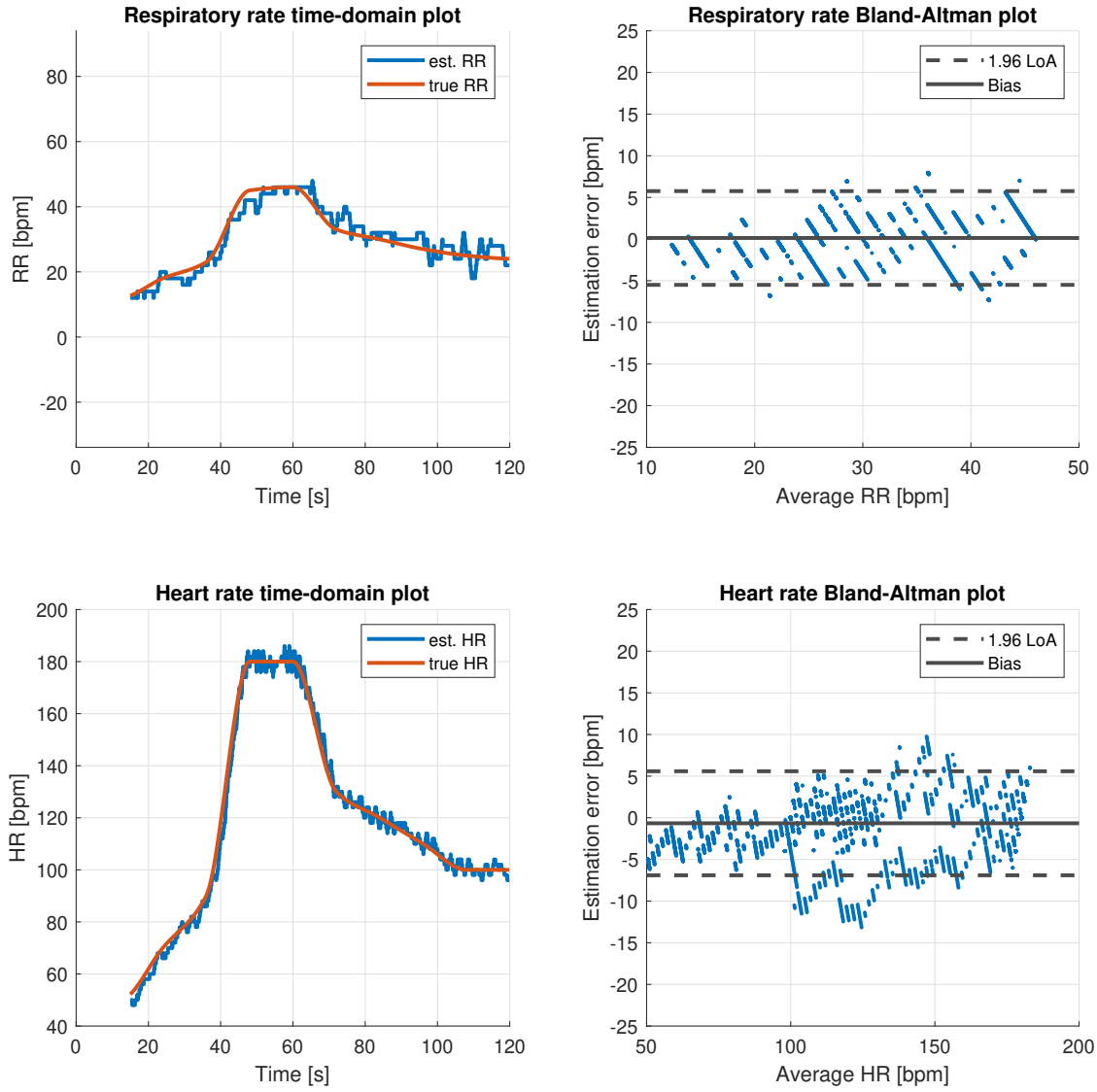

Figure 4.8: Optimized grid search algorithm - time-domain and Bland-Altman plots.

Table 4.4 shows the parameter values before and after the optimization.

parameter	original values	optimized values
r	0.15	0.20
$\mathbf{b} = [b_{RR}, b_{HR}]$	[0.5, 3.5]	[0.27, 2.22]
p	0.75	0.85

Table 4.4: Original and optimized values of the grid search algorithm parameters.

Table 4.5 shows the values of the performance metrics obtained before and after the optimization to prove that the optimized parameter values improve the algorithm's performance.

	before	after
RMSE_{RR} [bpm]	3.14	**2.87**
RMSE_{HR} [bpm]	**3.24**	3.25
bias_{RR} [bpm]	**0.04**	0.13
bias_{HR} [bpm]	**-0.65**	-0.66
LoA_{RR} [bpm]	6.16	**5.63**
LoA_{HR} [bpm]	**6.22**	6.25
TC [s]	37.49	**5.65**
$\overline{T}_{est}$ [ms]	7.15	**1.08**

Table 4.5: Performance metrics obtained before and after the optimization.

With the optimal values of the r and $\mathbf{b}$ parameters, the grid search algorithm performs slightly better in accuracy and robustness. The values of the accuracy metrics shown in Table 4.5 prove that the estimation is quite accurate considering the ranges of RR and HR values are more than ten times higher (12 to 46 bpm for RR, 50 to 180 bpm for HR).

However, the most noticeable improvement is achieved with parameter p set as 0.85 since the average computation time of one estimation $\overline{T}_{est}$ reaches close to 1 ms. This finally makes the grid search algorithm competitive compared to the iterative CLIE.

4.2.2 Iterative CLIE algorithm

Similarly to the $\mathbf{b}$ parameter in the grid search algorithm, $\mathbf{s}$ and $\mathbf{M}$ are composed of two parameters (one for RR and one for HR estimation). However, the RR and HR estimations of the iterative CLIE algorithm version 1 are entirely independent. Therefore, the optimization is performed as there would be four stand-alone parameters.

Figure 4.9 shows the time-domain and Bland-Altman plots obtained with the optimized CLIE algorithm.

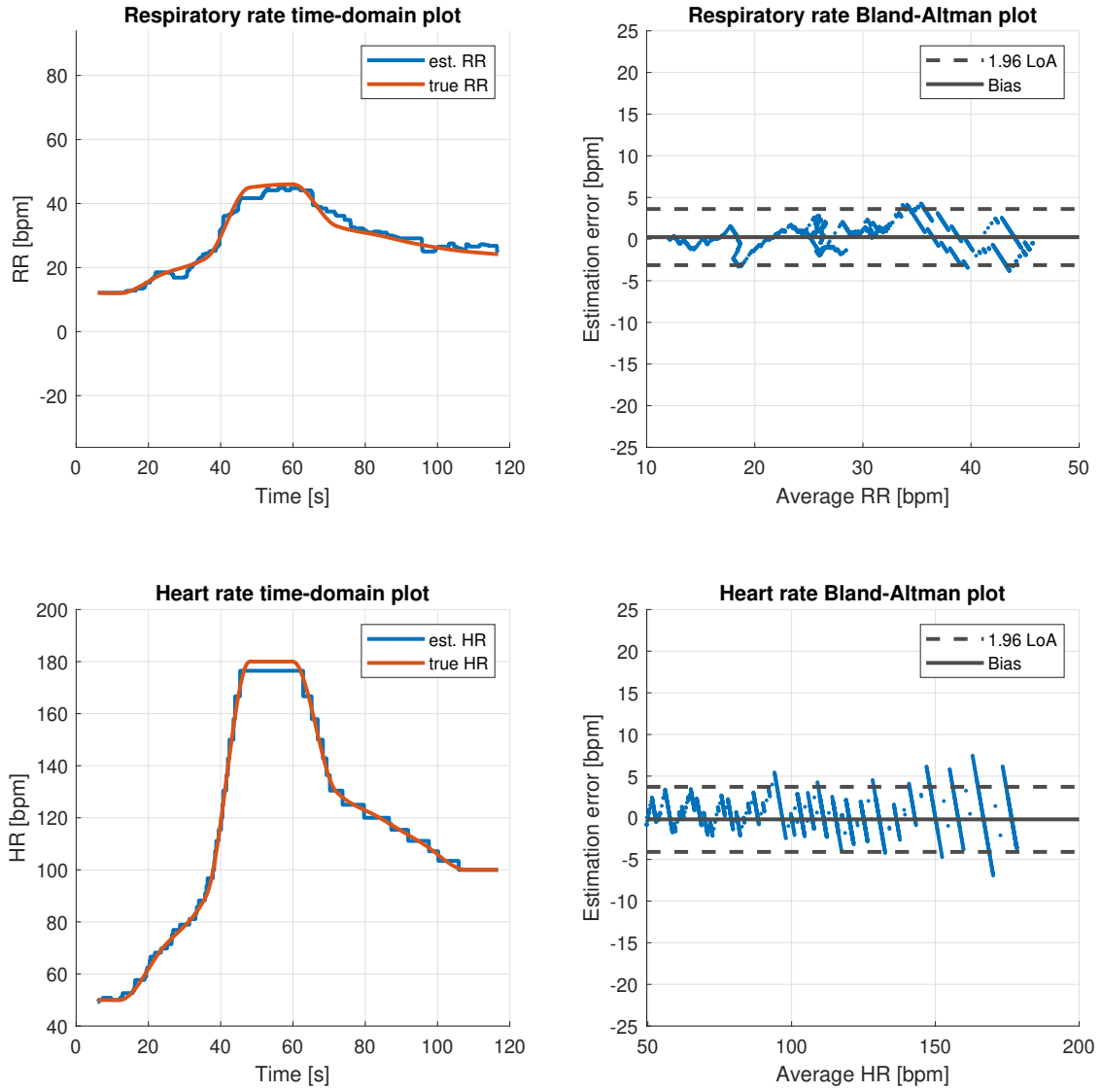

Figure 4.9: Optimized iterative CLIE algorithm - time-domain and Bland-Altman plots.

Table 4.6 shows the parameter values before and after the optimization.

parameter	original values	optimized values
$\mathbf{s} = [s_{RR}, s_{HR}]$	[50, 25]	[92, 25]
$\mathbf{M} = [M_{RR}, M_{HR}]$	[50, 25]	[281, 310]

Table 4.6: Original and optimized values of the CLIE algorithm parameters.

Table 4.7 shows the performance metrics values obtained before and after the optimization

to prove that the optimized parameter values improve the algorithm's performance.

	before	after
RMSE_{RR} [bpm]	2.15	**1.74**
RMSE_{HR} [bpm]	2.81	**2.00**
bias_{RR} [bpm]	**0.16**	0.24
bias_{HR} [bpm]	**-0.01**	-0.19
LoA_{RR} [bpm]	4.20	**3.37**
LoA_{HR} [bpm]	5.52	**3.19**
TC [ms]	**530.56**	541.74
$\overline{T}_{est}$ [ms]	**0.10**	**0.10**

Table 4.7: Performance metrics obtained before and after the optimization.

With the optimal values of the **s** and **M** parameters, the accuracy and robustness of the iterative CLIE algorithm are noticeably improved compared to the original parameter values.

When comparing Table 4.7 with Table 4.5, it seems that the CLIE algorithm performs slightly better than the grid search algorithm. However, it is to be noted that the grid search algorithm, unlike the CLIE, does not use any post-processing. Since the grid search-estimated RR and HR fluctuate even around the steady high plateau in the true RR and HR, some additional moving average window could be applied to smoothen the estimation.

Although the parameter optimization does not lower the $\overline{T}_{est} = 0.1$ ms, the iterative CLIE algorithm is still approximately ten times faster than the optimized grid search algorithm.

4.3 Source separation algorithms

Eventually, the best-performing optimized versions of the multi-pitch estimation algorithms are combined with the comb filtering algorithm, as explained in section 3.2.4. Furthermore, the true RR and HR values are used to determine whether the accuracy of the multi-pitch estimation algorithms limits the accuracy of the comb filtering algorithm.

Validation of the three complete algorithmic ensembles is performed using the synthesized validation signals described in detail in section 3.3.3, namely the signals in a typical lung pixel (see 3.7).

Figures 4.10, 4.11, and 4.12 show the results of the source separation performed using

the comb filtering algorithm combined with the grid search and CLIE algorithms and the true RR and HR values used for the validation signal synthesis. The complete algorithmic ensemble versions are numbered from one to three, respectively.

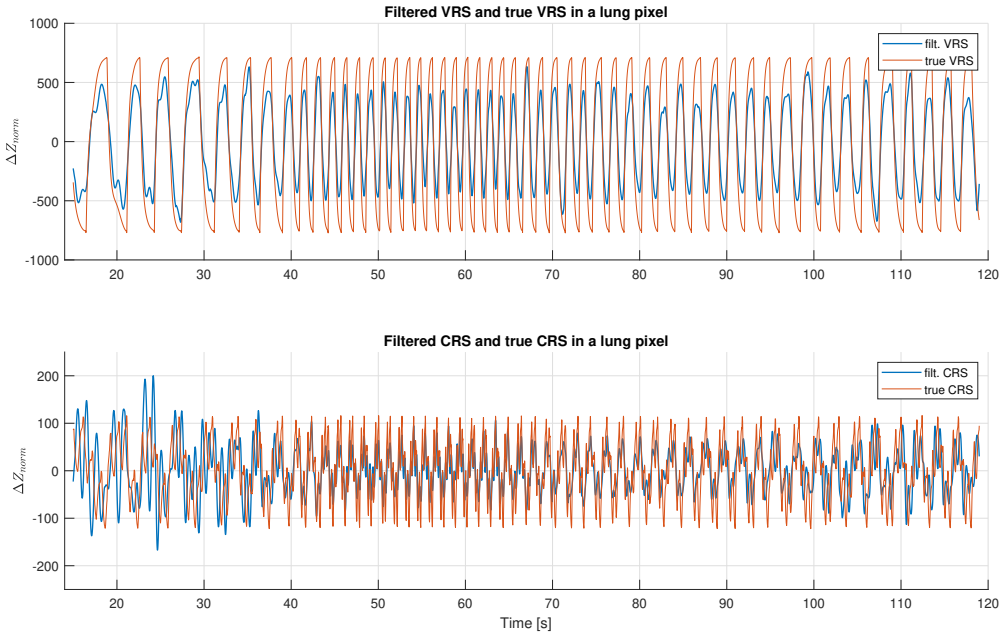

Figure 4.10: Source separation using comb filtering combined with the grid search algorithm.

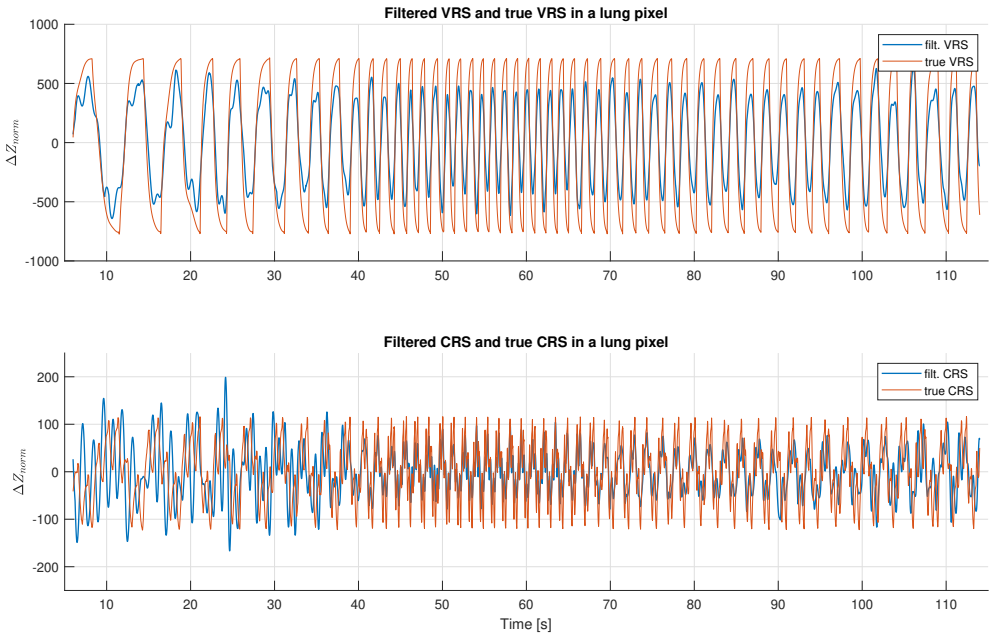

Figure 4.11: Source separation using comb filtering combined with the CLIE algorithm.

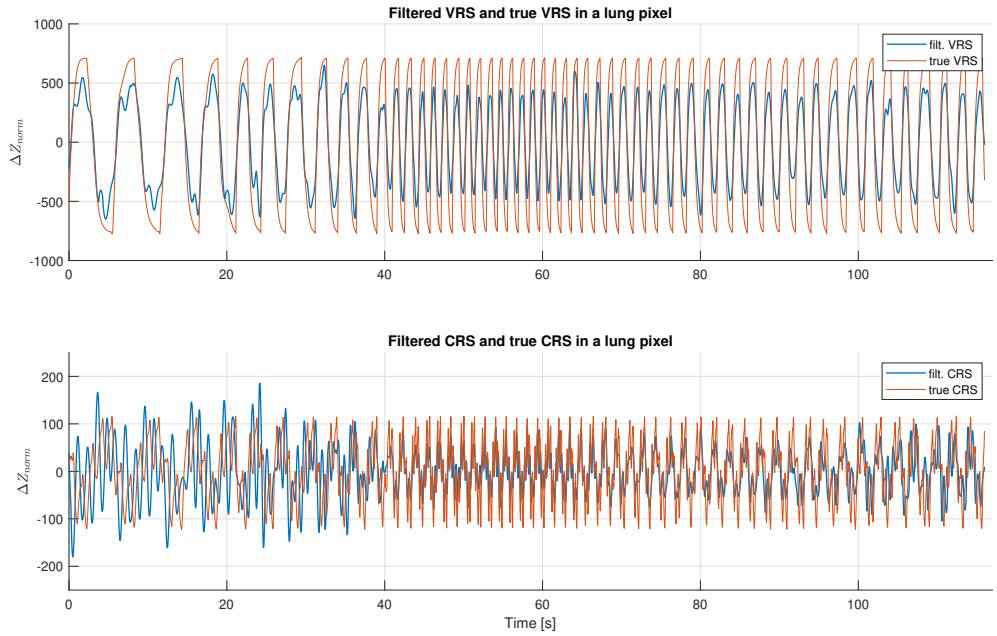

Figure 4.12: Source separation using comb filtering and the true RR and HR values.

Table 4.8 shows the values of performance metrics relevant to the source separation algorithm. These are RMSE, bias, Pearson correlation coefficient ρ, SSQI (see 3.4.5), T_C, and $\overline{T}_{est}$. The versions of the complete algorithmic ensemble for source separation are numbered in the same order as the above time-domain plots are presented.

Version	1	2	3
RMSE_{VRS} [a.u.]	256.53	**248.79**	249.38
RMSE_{CRS} [a.u.]	**57.67**	63.22	65.86
bias_{VRS} [a.u.]	**-1.35**	-1.87	-2.37
bias_{CRS} [a.u.]	**0.83**	-0.92	-1.06
ρ_{VRS} [a.u.]	**0.97**	**0.97**	**0.97**
ρ_{CRS} [a.u.]	**0.48**	0.39	0.35
SSQI [a.u.]	**235.81**	320.15	410.52
TC [s]	6.00	0.57	**0.13**
$\overline{T}_{est}$ [ms]	1.15	0.11	**0.02**

Table 4.8: Performance metrics obtained with each source separation algorithm version.

In the end, the first two implemented source separation algorithm versions show that the proposed approach might be applicable in real time. The average computation times of one estimation $\overline{T}_{est}$ are low enough, and the separated signals' waveforms show correct frequency and phase relations. Although the amplitudes of the filtered signals compared

to the true signals are smaller, especially those of the VRS, this could be addressed with further comb filter optimization or signal amplification for compensation.

When the true RR and HR are used, the accuracy is not significantly improved. Although the slightly worse performance metrics, shown in table 4.8 under version 3, happen mainly due to longer signals, it is important that they are not noticeably better. Consequently, this proves that the accuracy of the multi-pitch estimation algorithms is good enough not to limit the implemented comb filtering algorithm's accuracy significantly.

As shown in Table 4.8, version 1 of the complete algorithm performs slightly better. However, version 2 is almost ten times faster. The computation time is still a big concern since the EIT image usually has 64x64 = 4096 pixels. That means 4096 samples of EIT signals would have to be separated in less than 20 ms to provide a complete source separation of the EIT video with a frame rate of 50 fps.

It is to be noted that the grid search is currently implemented in MATLAB only. Therefore, converting the critical implementation parts into C would significantly decrease the computation time. However, even with the CLIE algorithm, the time needed to separate 4096 samples would be $0.02 \cdot 4096 = 81.92$ ms. Thus, lowering the computation time is still a critical target for a potential real-time application.

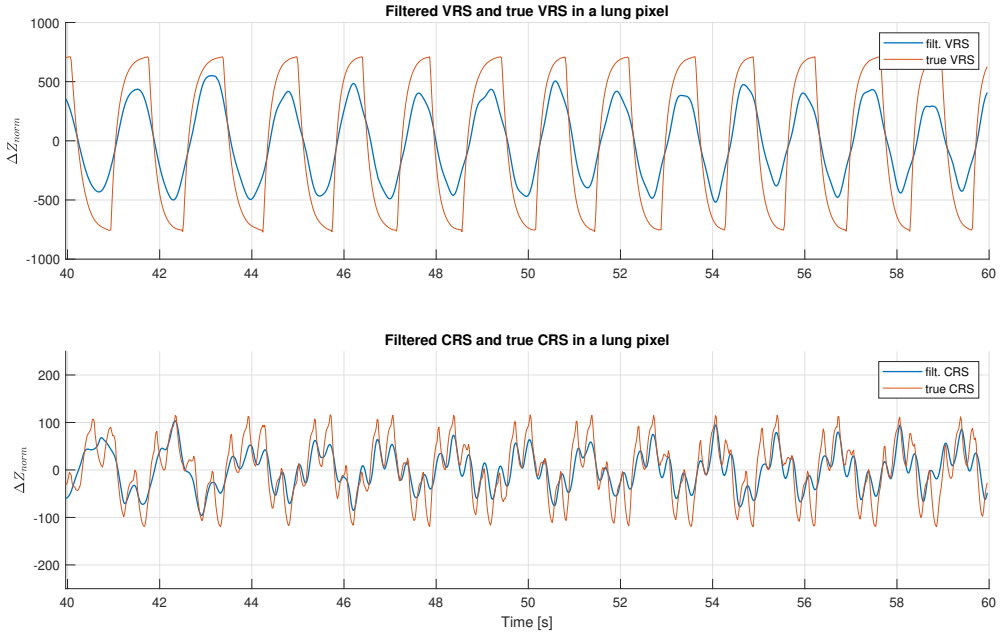

Figure 4.13: Detail of the source separation results shown in Figure 4.11.

As shown in Figure 4.13 and Table 4.9, the separation is more accurate when the true RR and HR are higher. This is probably due to the fixed size of the comb filter processing window. As mentioned in section 3.2.4, in a potential real-time implementation, the adaptive

window size would be forced by the multi-pitch estimation algorithm, making the comb filtering more dynamic and improving its robustness.

RMSE_{VRS} [a.u.]	286.09
RMSE_{CRS} [a.u.]	35.96
bias_{VRS} [a.u.]	2.50
bias_{CRS} [a.u.]	-0.57
ρ_{VRS} [a.u.]	0.96
ρ_{CRS} [a.u.]	0.83
SSQI [a.u.]	275.46

Table 4.9: Performance metrics obtained with the signals shown in Figure 4.13.

5 Conclusion

This work investigates and compares different dynamic source separation approaches to find the most suitable one for real-time source separation in EIT. First, after analyzing various possibilities, two selected multi-pitch estimation algorithms are implemented, one based on the grid search approach and the other on interval length estimation. These algorithms are combined with a simple comb filtering algorithm to serve as a proof-of-concept.

To validate and compare all the implemented algorithm combinations, different performance assessment metrics are introduced, and a validation signal is generated using an existing EIT signal synthesizer. This novel approach can provide a different point of view on the source separation algorithms since traditional validation using real EIT signals measured in patients cannot provide the ground truth for the EIT signal's components. Moreover, using the ground truth signals, the parameters of the multi-pitch estimation algorithms are optimized to improve the algorithms' performance further.

Eventually, the optimized multi-pitch estimation algorithms can provide fast and accurate frequency estimation from EIT signals (RMSE from 1.74 to 3.25 bpm and bias from -0.66 to 0.24 bpm) even for a challenging input EIT signal generated with RR between 12 and 46 bpm and HR between 50 and 180 bpm.

Consequently, the complete source separation algorithms prove that the proposed approach is applicable for separating the two main EIT signal components. The separated signals show correct frequency and phase relations, and the computation times are low enough to cope with the EIT video frame rate of 50 fps.

However, the presented results are obtained only with a synthesized signal in one lung pixel. When a proper real-time implementation at the bedside is considered, additional modifications of the implemented algorithms must be made to improve accuracy and robustness and further reduce computation time.

Nevertheless, despite these limitations, the presented algorithms represent satisfying proofs of the general concept. The main focus of future research should be implementing algorithms based on harmonic regression, as this is another highly promising method, and using real EIT signals measured in patients for comparison and validation.

Bibliography

[1] R. P. Henderson and J. G. Webster, "An impedance camera for spatially specific measurements of the thorax," *IEEE Transactions on Biomedical Engineering*, vol. BME-25, no. 3, pp. 250–254, 1978.

[2] S. Leonhardt and B. Lachmann, "Electrical impedance tomography: the holy grail of ventilation and perfusion monitoring?," *Intensive Care Med*, vol. 38(12), pp. 1917–1929, December 2012.

[3] A. Adler, (ed.) and D. Holder, (ed.), "Electrical impedance tomography: Methods, history and applications (2nd ed.)," *CRC Press*, 2021.

[4] J. M. Deibele, H. Luepschen, and L. S., "Dynamic separation of pulmonary and cardiac changes in electrical impedance tomography," *Physiological Measurement*, vol. 29, p. S1, June 2008.

[5] X. Sun, O. Jakob, J. Malmivuo, and S. Leonhardt, "Separation of cardiac- and ventilation-related signals within electrical impedance tomography data based on multi-dimensional ensemble empirical mode decomposition," *IFAC-PapersOnLine*, vol. 50, no. 1, pp. 4436–4441, 2017. 20th IFAC World Congress.

[6] A. Battistel, R. Chen, N. Hallemans, R. Pintelon, L. J., and K. Möller, "Harmonic analysis for the separation of perfusion and respiration in electrical impedance tomography," *IFAC-PapersOnLine*, vol. 54, no. 15, pp. 281–286, 2021. 11th IFAC Symposium on Biological and Medical Systems BMS 2021.

[7] I. Frerichs, M. B. P. Amato, A. H. v. Kaam, D. G. Tingay, Z. Zhao, B. Grychtol, M. Bodenstein, H. Gagnon, S. H. Böhm, E. Teschner, O. Stenqvist, T. Mauri, V. Torsani, L. Camporota, A. Schibler, G. K. Wolf, D. Gommers, S. Leonhardt, A. Adler, and TREND study group, "Chest electrical impedance tomography examination, data analysis, terminology, clinical use and recommendations: consensus statement of the translational eit development study group," *Thorax*, vol. 72, no. 1, pp. 83–93, 2017.

[8] E. Teschner, M. Imhoff, and S. Leonhardt, *Electrical Impedance Tomography: The realisation of regional ventilation Monitoring (2nd edition)*. Dräger Medical GmbH, January 2015.

[9] C. Putensen, B. Hentze, S. Muenster, and T. Muders, "Electrical impedance tomography for cardio-pulmonary monitoring," *Journal of Clinical Medicine*, vol. 8, no. 8, 2019.

[10] B. Nett, "Filtered backprojection (fbp) illustrated guide

for radiologic technologists." `https://howradiologyworks.com/filtered-backprojection-fbp-illustrated-guide-for-radiologic-technologists/`. online in How Radiology Works; accessed: 26. 08. 2023.

[11] D. C. Barber, "Quantification in impedance imaging," *Clinical Physics and Physiological Measurement*, vol. 11, pp. 45–46, January 1990.

[12] G. Hahn, I. Sipinkova, F. Baisch, and H. G., "Changes in the thoracic impedance distribution under different ventilatory conditions," *Physiological Measurement*, vol. 16, pp. A161–173, August 1995.

[13] A. Adler, J. H. Arnold, R. Bayford, A. Borsic, B. Brown, P. Dixon, T. J. C. Faes, I. Frerichs, H. Gagnon, Y. Gärber, B. Grychtol, G. Hahn, W. R. B. Lionheart, A. Malik, R. P. Patterson, J. Stocks, A. Tizzard, N. Weiler, and G. K. Wolf, "Greit: a unified approach to 2d linear eit reconstruction of lung images," *Physiological Measurement*, vol. 30, p. S35, June 2009.

[14] E. Stein, A. Chen, R. and; Battistel, and K. Möller, "Separating respiration and perfusion in eit: Harmonic analysis on 2d-thorax simulation," *Current Directions in Biomedical Engineering*, vol. 8, no. 2, pp. 785–788, 2022.

[15] C. Grant, T. Pham, J. Hough, T. Riedel, C. Stocker, and A. Schibler, "Measurement of ventilation and cardiac related impedance changes with electrical impedance tomography," *Critical care (London, England)*, vol. 15, p. R37, January 2011.

[16] A. Fagerberg, O. Stenqvist, and A. Aneman, "Monitoring pulmonary perfusion by electrical impedance tomography: an evaluation in a pig model," *Acta Anaesthesiologica Scandinavica*, vol. 53, no. 2, pp. 152–158, 2009.

[17] A. Fagerberg, O. Stenqvist, and A. Aneman, "Electrical impedance tomography applied to assess matching of pulmonary ventilation and perfusion in a porcine experimental model," *Critical Care*, vol. 13, no. R34, 2009.

[18] I. Frerichs, J. Hinz, P. Herrmann, G. Weisser, G. Hahn, M. Quintel, and G. Hellige, "Regional lung perfusion as determined by electrical impedance tomography in comparison with electron beam ct imaging," *IEEE Transactions on Medical Imaging*, vol. 21, no. 6, pp. 646–652, 2002.

[19] N. E. Huang, (ed.) and N. O. Attoh-Okine, (ed.), "The hilbert-huang transform in engineering (1st edition)," *CRC Press*, 2005.

[20] P. C. Young, D. J. Pedregal, and W. Tych, "Dynamic harmonic regression," *Journal of Forecasting*, vol. 18, no. 6, pp. 369–394, 1999.

[21] Q. Zhang, Q. Xie, M. Wang, and G. Wang, "Motion artifact removal for ppg signals

based on accurate fundamental frequency estimation and notch filtering," in *2018 40th Annual International Conference of the IEEE Engineering in Medicine and Biology Society (EMBC)*, pp. 2965–2968, 2018.

[22] C. Park, H. Shin, and B. Lee, "Blockwise ppg enhancement based on time-variant zero-phase harmonic notch filtering," *Sensors*, vol. 17, p. 860, April 2017.

[23] C. Park and B. Lee, "Real-time estimation of respiratory rate from a photoplethysmogram using an adaptive lattice notch filter," *Biomedical engineering online*, vol. 13, p. 170, December 2014.

[24] S.-C. Pei and C.-C. Tseng, "Elimination of ac interference in electrocardiogram using iir notch filter with transient suppression," *IEEE Transactions on Biomedical Engineering*, vol. 42, no. 11, pp. 1128–1132, 1995.

[25] Y. Wu, R. M. Rangayyan, Y. Zhou, and S.-C. Ng, "Filtering electrocardiographic signals using an unbiased and normalized adaptive noise reduction system," *Medical Engineering & Physics*, vol. 31, no. 1, pp. 17–26, 2009.

[26] D. Dobrev, T. Dobreva, and N. Mudrov, "Simple high-q comb filter for mains interference suppression," in *ELECTRONICS' 2008*, September 2008.

[27] L. Tan and J. Jiang, "Novel adaptive iir filter for frequency estimation and tracking [dsp tips&tricks]," *IEEE Signal Processing Magazine*, vol. 26, no. 6, pp. 186–189, 2009.

[28] C.-C. Tseng and P. S.-C., "Stable iir notch filter design with optimal pole placement," *IEEE Transactions on Signal Processing*, vol. 49, no. 11, pp. 2673–2681, 2001.

[29] M. Christensen and A. Jakobsson, "Multi-pitch estimation," *Synthesis Lectures on Speech and Audio Processing*, vol. 5, March 2009.

[30] C. Weiß and G. Peeters, "Learning multi-pitch estimation from weakly aligned score-audio pairs using a multi-label ctc loss," in *2021 IEEE Workshop on Applications of Signal Processing to Audio and Acoustics (WASPAA)*, pp. 121–125, 2021.

[31] X. Li, Y. Yan, J. Soraghan, Z. Wang, and J. Ren, "A music cognition–guided framework for multi-pitch estimation," *Cognitive Computation*, vol. 15, pp. 23–35, 2023.

[32] D. F. Silva and S. Leonhardt, "A real-time dual heart and respiratory rate estimator for electrical impedance tomography," *2023 IEEE 36th International Symposium on Computer-Based Medical Systems (CBMS)*, pp. 426–430, 2023.

[33] S. Maisch, S. H. Bohm, J. Solà, M. S. Goepfert, J. C. Kubitz, H. P. Richter, J. Ridder, A. E. Goetz, and D. A. Reuter, "Measurement of heart-lung interactions by electrical

impedance tomography," *Critical Care Medicine*, vol. 39, pp. 2173–2176, September 2011.

[34] C. H. Antink, S. Leonhardt, and M. Walter, "A synthesizer framework for multimodal cardiorespiratory signals," *Biomedical Physics & Engineering Express*, vol. 3, p. 035028, June 2017.

[35] C. Brüser, S. Winter, and S. Leonhardt, "Robust inter-beat interval estimation in cardiac vibration signals," *Physiological Measurement*, vol. 34, p. 123, January 2013.

[36] C. H. Antink, S. Leonhardt, and M. Walter, "Local interval estimation improves accuracy and robustness of heart rate variability derivation from photoplethysmography," in *2018 40th Annual International Conference of the IEEE Engineering in Medicine and Biology Society (EMBC)*, pp. 3558–3561, 2018.

[37] G. Y. Jang, Y. J. Jeong, T. Zhang, T. I. Oh, R.-E. Ko, C. R. Chung, G. Y. Suh, and E. J. Woo, "Noninvasive, simultaneous, and continuous measurements of stroke volume and tidal volume using eit: feasibility study of animal experiments," *Scientific reports*, vol. 10, July 2020.

[38] M. Proença, "Non-invasive hemodynamic monitoring by electrical impedance tomography," *Lausanne, EPFL*, 2017.

[39] M. Koledintseva, R. DuBroff, and R. Schwartz, "A maxwell garnett model for dielectric mixtures containing conducting particles at optical frequencies," *Progress in Electromagnetics Research-pier - PROG ELECTROMAGN RES*, vol. 63, pp. 223–242, January 2006.

[40] D. F. Silva and S. Leonhardt, "Fast 4d fem model for eit source separation benchmarking," in *Current Directions in Biomedical Engineering*, 2023.

[41] G. B. Kaplan, O. Içoglu, A. B. Yoldemir, and M. Sezgin, "Real-time object detection using dynamic principal component analysis," in *Proceedings of the XIII Internarional Conference on Ground Penetrating Radar*, pp. 1–6, 2010.

[42] Z. Bankó, L. Dobos, and J. Abonyi, "Dynamic principal component analysis in multivariate time-series segmentation," *Conservation, Information, Evolution*, vol. 1, pp. 11–24, January 2011.

[43] E. G. Tarpara and V. H. Patankar, "Real time implementation of empirical mode decomposition algorithm for ultrasonic nondestructive testing applications," *Review of Scientific Instruments*, vol. 89, p. 125118, December 2018.

[44] A. Santillán-Guzmán, M. Fischer, U. Heute, and G. Schmidt, "Real-time empirical

mode decomposition for eeg signal enhancement," in *21st European Signal Processing Conference (EUSIPCO 2013)*, pp. 1–5, 2013.

[45] P. Trnka and M. Hofreiter, "The empirical mode decomposition in real-time," in *Proceedings of the 18th International Conference on Process Control*, January 2011.

[46] R. Lan, L. Sun, Z. Liu, H. Lu, C. Pang, and X. Luo, "Madnet: A fast and lightweight network for single-image super resolution," *IEEE Transactions on Cybernetics*, vol. 51, no. 3, pp. 1443–1453, 2021.

[47] Y. Romano, J. Isidoro, and P. Milanfar, "Raisr: Rapid and accurate image super resolution," *IEEE Transactions on Computational Imaging*, vol. 3, no. 1, pp. 110–125, 2017.

[48] The University of Queensland, Australia, "Taylor series in two dimensions." `https://teaching.smp.uq.edu.au/scims/Num_analysis/Taylor.html`, 2017. online in Science and Mathematics Simulations (SciMS) - Numerical Analysis; accessed: 26. 08. 2023.

[49] MathWorks (1994-2023 The MathWorks, Inc.), "Documentation for the function iirnotch." `https://www.mathworks.com/help/dsp/ref/iirnotch.html`. online; accessed: 24. 08. 2023.

[50] MathWorks (1994-2023 The MathWorks, Inc.), "Documentation for the function filtfilt." `https://www.mathworks.com/help/signal/ref/filtfilt.html`. online; accessed: 24. 08. 2023.

[51] K. R. Visser, "Electric properties of flowing blood and impedance cardiography," *Annals of Biomedical Engineering*, vol. 17, no. 5, p. 463–473, 1989.

[52] W. Huang, R. T. Yen, M. McLaurine, and G. Bledsoe, "Morphometry of the human pulmonary vasculature," *Journal of Applied Physiology*, vol. 81, no. 5, pp. 2123–2133, 1996.

[53] R. Avram, G. H. Tison, K. Aschbacher, P. Kuhar, E. Vittinghoff, M. Butzner, R. Runge, N. Wu, M. J. Pletcher, G. M. Marcus, and J. Olgin, "Real-world heart rate norms in the health eheart study," *npj Digital Medicine*, vol. 2, June 2019.

[54] A. Nicolò, C. Massaroni, E. Schena, and M. Sacchetti, "The importance of respiratory rate monitoring: From healthcare to sport and exercise," *Sensors*, vol. 20, no. 21, 2020.

[55] K. Nakajima, T. Tamurat, and H. Miike, "Monitoring of heart and respiratory rates by photoplethysmography using a digital filtering technique," *Medical Engineering & Physics*, vol. 18, pp. 365–372, July 1996.

[56] F. Scholkmann and U. Wolf, "The pulse-respiration quotient: A powerful but untapped parameter for modern studies about human physiology and pathophysiology," *Frontiers in Physiology*, vol. 10, 2019.

[57] Garmin (1996-2023 Garmin Ltd. or its subsidiaries), "Critical relationship between respiratory rate, heart rate and cadence?." `https://www.garmin.com/en-PH/blog/critical-relationship-between-respiratory-rate-heart-rate-and-cadence/`, August 2020. online; accessed: 25. 08. 2023.

[58] S. Fleming, M. Thompson, R. Stevens, C. Heneghan, A. Plüddemann, I. Maconochie, L. Tarassenko, and D. Mant, "Normal ranges of heart rate and respiratory rate in children from birth to 18 years: a systematic review of observational studies," *The Lancet*, vol. 377, p. 1011–1018, March 2011.

[59] Medical News Today (2023 Healthline Media UK Ltd, Brighton, UK), "What to know about newborn respiratory rates." `https://www.medicalnewstoday.com/articles/327164`. online; accessed: 25. 08. 2023.

[60] E. Corregera, G. Muriasb, E. Chaconc, A. Estrugac, B. Salesd, J. Lopez-Aguilarc, J. Montanyae, U. Lucangelof, O. Garcia-Esquirole, A. Villagrac, J. Villard, R. M. Kacmarekh, M. J. Burgueñoc, and L. Blanchc, "Interpretation of ventilator curves in patients with acute respiratory failure," *Medicina Intensiva*, vol. 36, pp. 294–306, May 2012.

[61] B. K. Walsh and C. D. Smallwood, "Electrical impedance tomography during mechanical ventilation," *Respiratory Care*, vol. 61, no. 10, pp. 1417–1424, 2016.

[62] MathWorks (1994-2023 The MathWorks, Inc.), "Documentation for the function corrcoef." `https://www.mathworks.com/help/matlab/ref/corrcoef.html`. online; accessed: 28. 08. 2023.

A Parameter optimization figures

A.1 Grid search algorithm

Figure A.1 shows all the values of MEQI and $\overline{T}_{est}$ obtained during r parameter optimization using the set of values $\{0.05, 0.10, ..., 1.00\}$. With the optimum $r^* = 0.20$, the grid search achieves MEQI of 0.84 and $\overline{T}_{est}$ of 18.14 ms. Although the lowest $\overline{T}_{est}$ value is achieved with $r = 0.15$, the relative difference in computation time of less than 0.4 % is not really important.

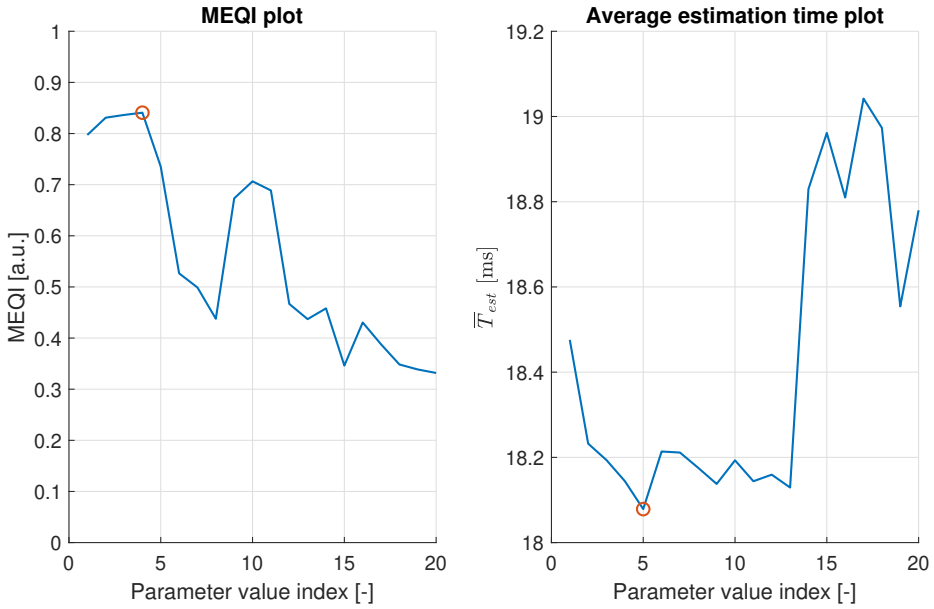

Figure A.1: MEQI (left) and $\overline{T}_{est}$ (right) - parameter r optimization.

Figure A.2 shows the values of MEQI and $\overline{T}_{est}$ obtained during **b** parameter optimization. A 2-column matrix of all the possible combinations is defined. The optimal values $b^*_{RR} = 0.27$ and $b^*_{HR} = 2.22$ achieve MEQI = 0.99 and $\overline{T}_{est} = 10.98$ ms. Similarly to the optimization of the r parameter, the minimum $\overline{T}_{est}$ is slightly lower for different values of **b** but the difference is negligible.

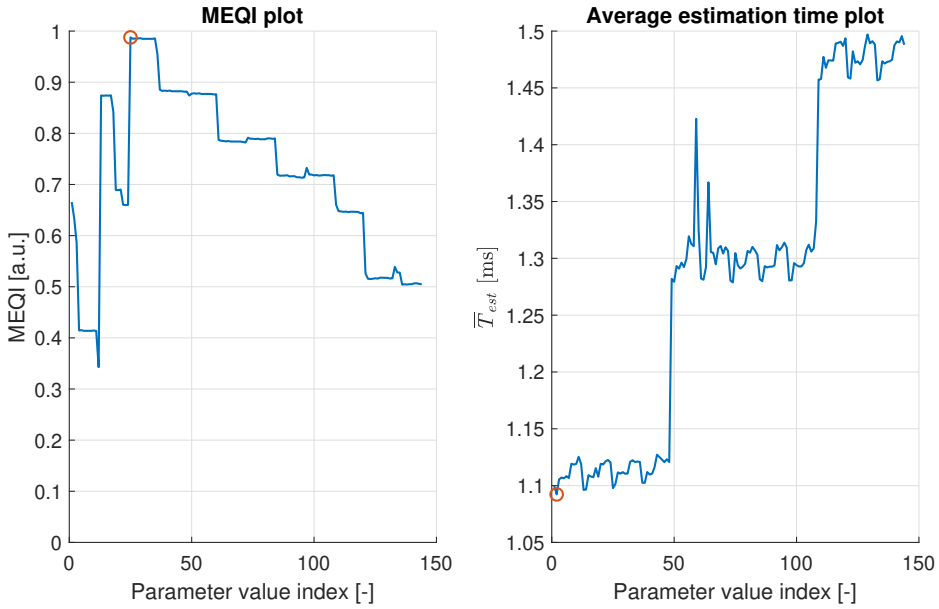

Figure A.2: MEQI (left) and $\overline{T}_{est}$ (right) - parameter **b** optimization.

Figure A.3 shows all the values of MEQI and $\overline{T}_{est}$ obtained during p parameter optimization using the set of values $\{0.40, 0.45, ..., 1.00\}$. The optimum $p^* = 0.85$ achieves MEQI of 1.00 and $\overline{T}_{est}$ of 0.98 ms. Since any higher value of p leads to a significant loss in the estimation accuracy, this the lowest achievable $\overline{T}_{est}$.

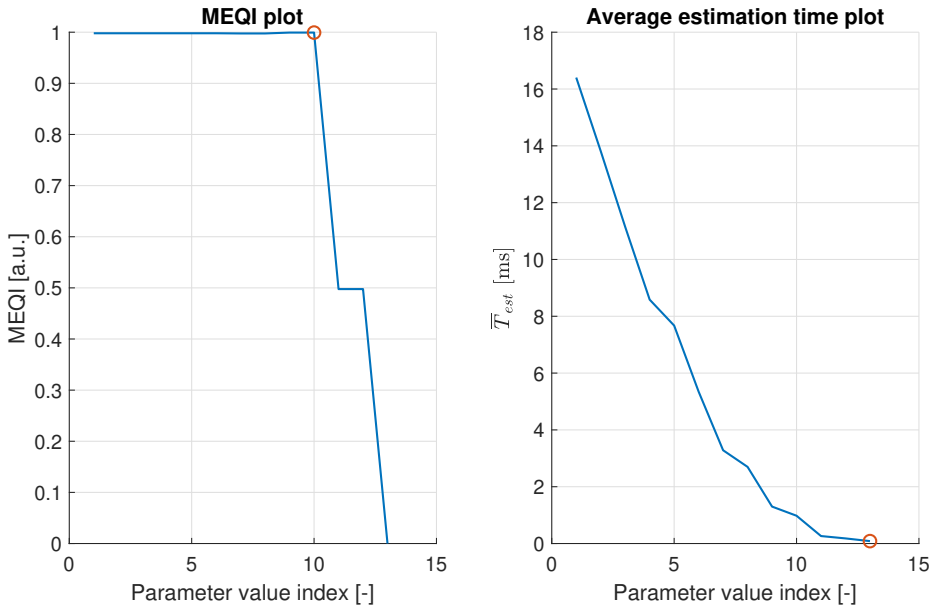

Figure A.3: MEQI (left) and $\overline{T}_{est}$ (right) - parameter p optimization.

A.2 Iterative CLIE algorithm

Figures A.4 and A.5 show all the values of MEQI and $\overline{T}_{est}$ obtained during **s** parameter optimization. With the optimal values $s^*_{RR} = 92$ and $s^*_{HR} = 25$, CLIE achieves MEQI of [0.83, 1.00] and $\overline{T}_{est}$ of [0.08, 0.05] ms.

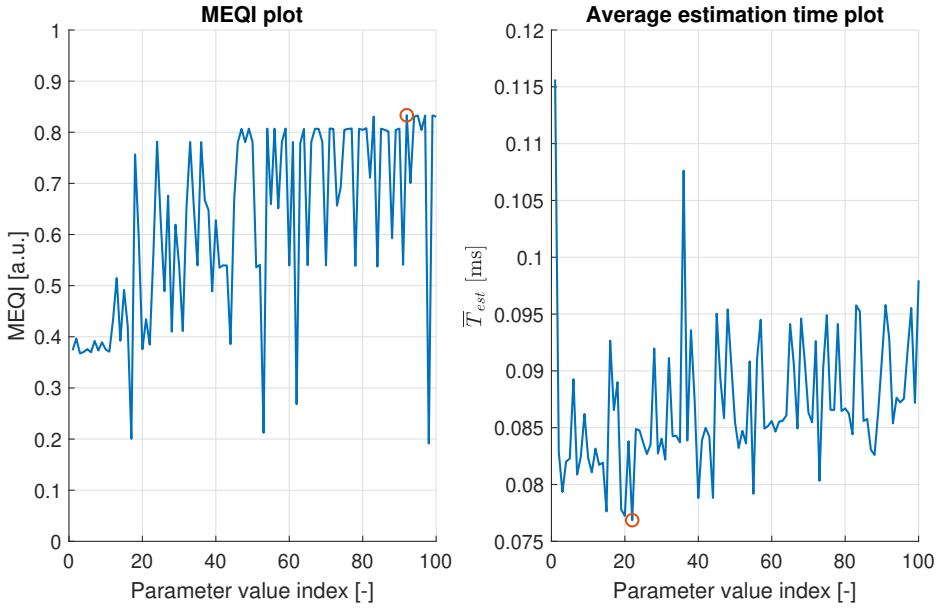

Figure A.4: MEQI (left) and $\overline{T}_{est}$ (right) - parameter s_{RR} optimization.

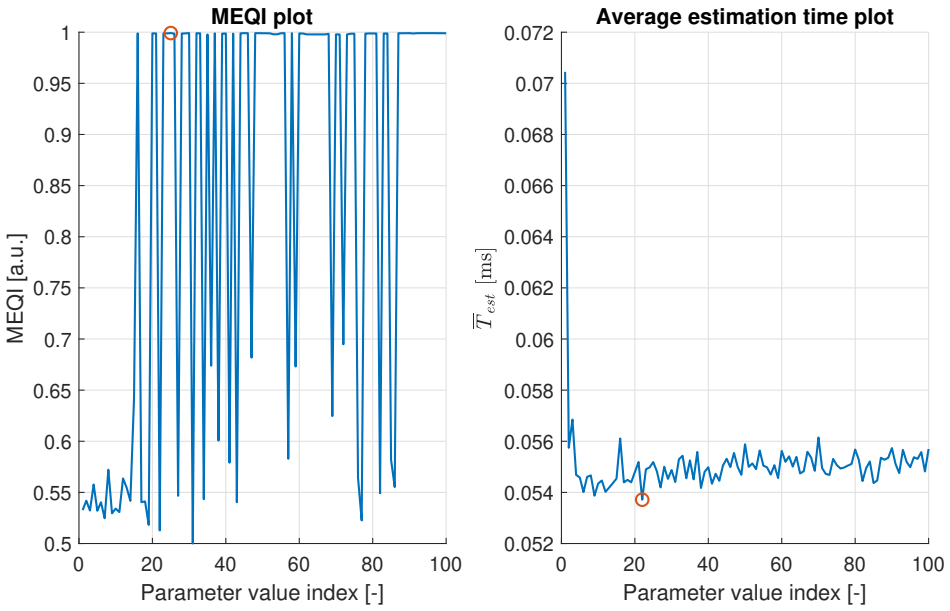

Figure A.5: MEQI (left) and $\overline{T}_{est}$ (right) - parameter s_{HR} optimization.

Figures A.6 and A.7 show all the values of MEQI and $\overline{T}_{est}$ obtained during **M** parameter optimization. With the optimal values $M^*_{RR} = 281$ samples and $M^*_{HR} = 310$ samples, MEQI of [0.93, 0.87] and $\overline{T}_{est}$ of [0.06, 0.06] ms are achieved.

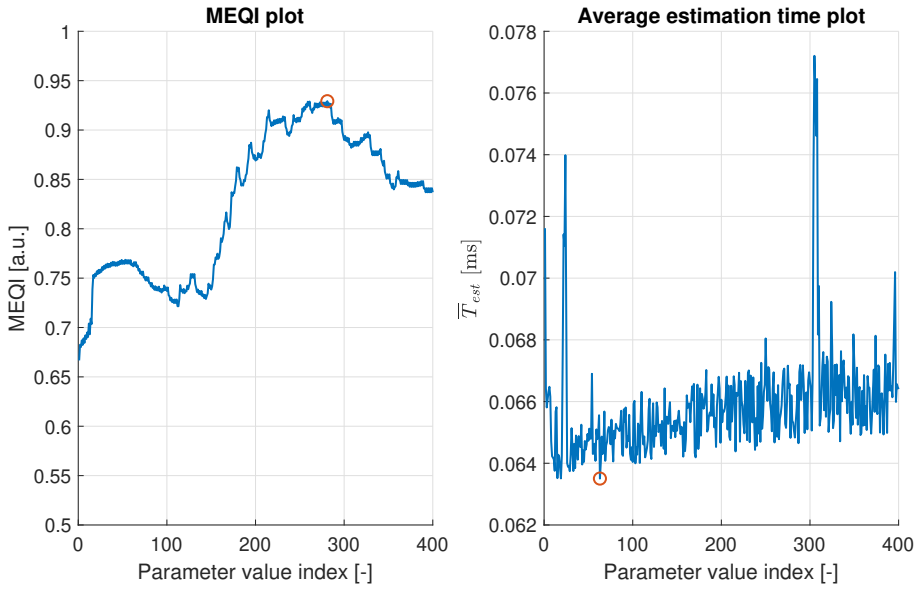

Figure A.6: MEQI (left) and $\overline{T}_{est}$ (right) - parameter M_{RR} optimization.

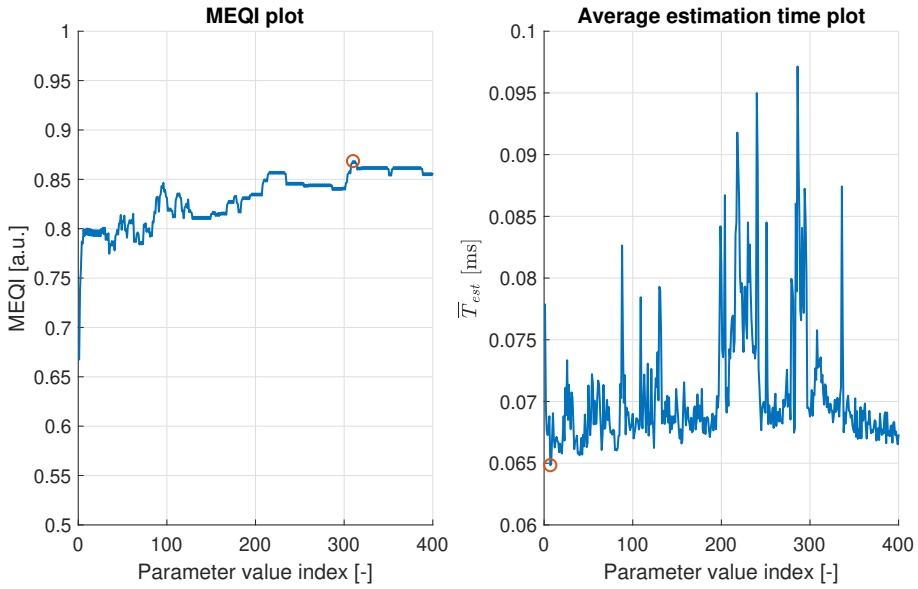

Figure A.7: MEQI (left) and $\overline{T}_{est}$ (right) - parameter M_{HR} optimization.